AU-BASED CORE-SHELL NANOPARTICLES FOR DIRECT FORMIC ACID FUEL CELLS

by

CHIAJEN HSU

Presented to the Faculty of the Graduate School of

The University of Texas at Arlington in Partial Fulfillment

of the Requirements

for the Degree of

DOCTOR OF PHILOSOPHY

THE UNIVERSITY OF TEXAS AT ARLINGTON

December 2013

Acknowledgements

First of all, I would deeply appreciate my mentor, Dr. Fuqiang Liu, for his advice, support, and inspiration in my research life. Under his guidance, I learned how to discover and discuss the beauty of science behind the surficial phenomena. I would appreciate Dr.Yaowu Hao's co-advising as well. Without his fully support of hollow gold nanoparticle knowledge and technique, this dissertation cannot be done.

Second, I would like to thank my committee member, Dr. Seong Jin Koh, Dr. "Max" Qinhong Hu, and Dr. Kyungsuk Yum for their suggestions to integrate the whole dissertation. I also want to thank my senior and friend, Dr. Chienwen Huang, for his suggestions and support not only in the experiment but also in my life. We really enjoyed a joyful research life in UTA. Besides, I would be so fortune to have many lab-mates, Md. N Siddique, Syed D Sajjad, Dong Liu, Amir H Salehi Gilani, Zi Wei, Yi Shen, Akanksha Pandey and Sonam Patel from Dr. Liu's lab, and also Chivarat Muangphat, Orathai Thumthan, Jiaqi Wu, Ruiqian Jiang, and Punnapob Punnakitikashem from Dr.Hao's lab. Third, I would also appreciate Dr. Jiechao Jiang and David Yan for their assist in Characterization Center for Materials and Biology in UTA.

Last but not least, I have to express my deepest gratitude to my grandmother, parents, and brothers in Taiwan for their great supports. Especially, I would like to thank Heyi to encourage me to pass this long research journey.

November 15, 2013

Abstract

AU-BASED CORE-SHELL NANOPARTICLES FOR DIRECT FORMIC ACID FUEL CELLS

Chiajen Hsu, PhD

The University of Texas at Arlington, 2013

Supervising Professor: Fuqiang Liu

Unique Au/Pd core-shell nanoparticles were synthesized via galvanic replacement of Cu by Pd on hollow Au nanoparticles. Au/PtCu core-shell nanoparticles were also synthesized using this method. These core-shell nanoparticles exhibited unique electrochemical properties - the Au/Pd nanoparticles demonstrated superior electrochemical activity for formic acid oxidation and the Au/PtCu nanoparticles improved the kinetics in oxygen reduction reaction, when compared to their corresponding pure metal particles. In this dissertation, we aim at investigating catalytic abilities of these core-shell nanoparticles and understanding electrochemical reactions in direct formic acid fuel cells.

Different Pd thicknesses on hollow Au nanoparticles in the core-shell configuration have been investigated. The hollow Au nanoparticles served as substrates. First, a sacrificial Cu layer was coated on the Au nanoparticles and then replaced by Pd in a $PdCl_2$ solution via a galvanic replacement reaction. The thickness of the Pd layer was determined by the Cu layer thickness which was tailored by the coating time. It has been found that the Au/Pd nanoparticles exhibited superior formic acid oxidation performance, lower CO-stripping peak potential, and long-term durability and stability

compared to commercial Pd black due to enhanced electronic coupling between Au core and Pd shell.

To optimize the cathodic reaction (so-called oxygen reduction reaction) in direct formic acid fuel cells, it is necessary to investigate the electro-catalytic abilities of cathodic materials. Herein, we adopted the Au/PtCu core-shell nanoparticles to study their performance and electro-catalytic mechanism in oxygen reduction reaction. The Au/PtCu core-shell nanoparticles were fabricated via galvanic replacement of Cu by Pt on hollow Au nanoparticles. The Pt thickness was also controlled by the Cu coating time. We found that up to 83 wt. % of Cu can be replaced in 5 mM K_2PtCl_4 solution, forming an alloyed PtCu phase which was confirmed by X-ray diffraction data. Results showed 2-2.5 times higher in area specific activity and mass specific activity of the Au/PtCu catalysts than the commercial Pt black and Pt/C in oxygen reduction reaction, measured by a rotating disk electrode system. The kinetic electrochemical studies showed a four-electron transfer process, suggesting an efficient pathway of O_2 directly reduced to H_2O. Besides, Au nanoparticles with a thinner PtCu shell (25 nm thickness) demonstrated a significant CO oxidation peak shift (by 0.13 V) and improved long-term durability probably due to the core-shell structure and the electronic coupling effect.

Further improvement in both activity and durability of the Au-based core-shell nanoparticles relies on the electronic coupling between core and shell which can be manipulated by tuning the Au core surface roughness. Two methods have been attempted: varying Au particle size by changing of the Au solution concentration and controlling surface roughness by adding a Na_2SO_3 solution. Smaller and more porous Au nanoparticles were formed when dilute Au solutions were used. The Au/Pd nanoparticles synthesized using a dilute Au concentration (7.775 g L^{-1}) showed the highest formic acid oxidation activity (0.93 mA cm^{-2} at 0.3 V). In addition, the roughness of the hollow Au

cores was also tailored by adding a Na_2SO_3 solution. It was found that the higher concentration of Na_2SO_3 was used, the rougher Au nanospheres became. However, the rough Au surface may reduce the electronic coupling with the Pd layer and decrease the catalytic abilities. The Au/Pd nanoparticles synthesized without the Na_2SO_3 solution yielded the smoothest Pd surface and demonstrated the highest formic acid oxidation activity (0.71 mA cm^{-2} at 0.3 V).

Raman spectroscopy was adopted to study formic oxidation mechanism on the Au/Pd core-shell nanoparticles thanks to the enhanced surface plasmon resonance from the hollow Au cores. By combining with electrochemical stripping analysis, the in situ Raman studies helped reveal the electrochemical intermediate species at differently applied potentials. In this study, CO stripping test in conjunction with the in situ Raman studies showed a lower oxidation potential (0.6 V vs. Ag/AgCl) of CO on the Au/Pd nanoparticles than the Pd black (> 0.6 V), suggesting a strong electronic coupling between Au and Pd in the core-shell nanoparticles which contributes to the enhanced electro-oxidation of formic acid.

To further explore the formic acid oxidation mechanism, oxidation of formate-based solutions were studied on the Au/Pd nanoparticles. Compared to the Pd black, the Au/Pd nanoparticles showed superior catalytic activities and stabilities especially when using concentrated formate solutions, indicating formate as the main electro-oxidation intermediate species in the reactions. Furthermore, oxidation of the formate-based solutions was numerically simulated. The results indicated a lower formate and hydroxyl coverage at the same applied potential for the Au/Pd nanoparticles than the Pd black, suggesting an efficient removal of these intermediates probably due to the strong electronic coupling within these nanoparticles.

Table of Contents

List of Illustrations

List of Tables

List of Acronyms

AAO	Anodic Aluminum Oxide
ASA	Area Specific Activity
AST	Accelerated Stress Test
BE	Binding Energy
CA	Chronoamperometry
CV	Cyclic Voltammogram
DFAFC	Direct Formic Acid Fuel Cell
DFT	Density Function Theory
DMAB	Dimethylamine Borane
DMFC	Direct Methanol Fuel Cell
FA	Formic Acid
FAO	Formic Acid Oxidation
FDTD	Finite Difference Time Domain
FE-SEM	Field Emission-Scanning Electron Microscopy
EDTA	Ethylenediamine Tetraacetic Acid
ECSA	Electrochemical Surface Area
HR-TEM	Higher Resolution-Transmission Electron microscopy
HAADS-TEM	High Angle Annular Dark Field-TEM
MEA	Membrane Electrode Assembly
MSA	Mass Specific Activity
NHE	Normal Hydrogen Electrode
ORR	Oxygen Reduction Reaction
PEMFC	Polymer Electrolyte Membrane Fuel Cell
RDE	Rotated Disc Electrode

SAED	Selected Area Electron Diffraction
SCE	Saturated Calomel Electrode
SERS	Surface Enhanced Raman Scattering
SF	Sodium Formate
SPR	Surface Plasmon Resonance
UPD	Underpotential Deposition
UV-Vis	Ultraviolet Visible Spectroscopy
XRD	X-Ray Diffraction
XPS	X-ray Photoelectron Spectroscopy

Chapter 1

Introduction

1.1 Alloyed Catalysts for DFAFCs

Direct formic acid fuel cells (DFAFCs) [1-11] appear as ideal portable power sources due to their unique features such as high open circuit voltage (1.45 V), allowable high concentration of fuel, and lowfuel crossover through membranes compared to direct methanol fuel cells. In a fuel cell system, the most important component in determining the overall efficiency is the catalyst which reacts with fuels (e. g., H_2, methanol, and formic acid...etc.) and oxygen, and hence generates current and potential. Such reactions between solid catalysts and fuel/oxygen are so-called heterogeneous reactions, which involve adsorption, surface diffusion, reaction, and desorption [9]. These reaction steps depend on both geometric and electronic characteristics of the catalysts. For example, pure Pd nanoparticles possess two most active planes, (111) and (100), where the most favorable geometric factors (e.g., Pd-Pd interatomic distance, coordination number, etc) exist. Besides, particle size as another geometric factor dominates both mass specific activity (MSA, in mA/g or A/kg) and area specific activity (ASA, in A/m^2) of the catalyst. With decreasing particle size, the MSA increases; however, the ASA drops as a results of increasing surface defects. In addition, the catalysts become less durable due to the Gibbs-Thomson effect. In summary, high activity and durability of pure metal particles as catalyst for electrochemical reactions cannot be simultaneously achieved.

Alloyed nanoparticles were proposed to improve catalytic property over the single-element materials. For example, alloyed nanoparticles [12-15] as the anodic catalysts on formic acid oxidation (FAO) reaction have been widely investigated. Pd-based [12-26] alloyed catalysts are reported to achieve superior FAO activity than pure Pd particles.The enhancement of catalytic activity is attributed to interactions between the

metallic components in the alloyed catalysts, including geometric [27-31] and electronic contributions [24, 32-37], which are commonly triggered by size, shape, morphology, interface and electronic structure. However, several issues remain unresolved for these alloyed materials:

- Independent control or synthesis of each element is difficult as the elements are miscible at atomic level in an alloy. The catalytic properties were normally controlled by composition of two materials, sintering temperature and time, and shape of the structure.
- It is hard to study the function of individual element of the catalysts.
- It is difficult to understand the interaction between the elements as their interface is hard to define.

1.2 Core-shell Nanoparticles for DFAFCs

To resolve the above dilemma, the core-shell structure provides a remedy. There are two types of the core-shell nanoparticles: one is crystalline core-shell nanoparticles and the other is polycrystalline hollow core-shell nanoparticles. There are three major advantages of the polycrystalline hollow core-shell nanoparticles, which are the focus of this study:

- Surface curvature: The nanocrystalline grain size is decoupled from the primary particle size.
- Freedom: The nanocrystalline area/shell, mass specific activity, and durability that can be controlled independently
- Low cost: Hollow core (e.g., Au) uses less material than solid core.

The polycrystalline hollow core-shell nanoparticles [38-40] as the facilely controllable structures could potentially promote both the geometric and electroniccontributions, and demonstrate high catalytic activity, stability and durability. In addition, the core-shell

structures can be easily tailored by controlling the composition, structure, or even particle size of the core and the shell, therefore acting as an ideal platform to explore the interaction between the core and shell. Also, the interaction between the core and shell strongly relies on interfacial stress, morphology and roughness of the core. It was reported that the compressive strain existed in shell results in the changes of the electronic structure and hence weakens the oxygenated chemisorption [41].

1.2.1 The Advantages of Au Core

According to lots of the benefits from the core-shell nanoparticles, we proposed that our Au based core-shell nanoparticles can achieve high activity and stability as well by controlled well on their geometric and electronic properties. The inner hollow Au core can reduce the amount of Au and provide large surface area. In addition, Au seems to be a potential candidate to stabilize the catalysts in fuel cell systems [42]. It was reported [43, 44] that the Au cluster can stabilize Pt during long-term cycles to diminish dissolution in the acidic environment.

Furthermore, the Au core may enhance Raman scattering due to its unique surface plasmon resonance (SPR), which is so-called surface enhanced Raman scattering (SERS). This cutting edge technique is used not only for bio-applications [45] but for electrochemical reaction observations [23, 46-50]. The SERS combined with electrochemical equipment is capable and sensitive to monitor molecules changes in situ. Recently, in situ SERS studies of CO electro-oxidation on crystalline core-shell Au/Pd nanoparticles have been demonstrated to observe change in molecule adsorption at different potentials [51-54]. According to previous reports, the hollow Au nanoparticles have demonstrated high and tunable SPR effect for bio-applications [55, 56]. In situ SERS studies on hollow Au/Pd core-shell nanoparticles during electrochemical reactions would shed lights on enhance mechanism of these core-shell nanoparticles.

1.2.2 The Au/Pd Core-shell Nanoparticles for FAO

Among many core-shell structures, the Au/Pd core-shell nanoparticles [12, 40, 57-60] exhibit superior electrochemical activity toward electrochemical reactions. With the superior Au as the core, the polycrystalline noble metallic shell (e.g., Pd and Pt) is tunable to improve the overall catalytic ability. Inner Au core can be easily synthesized by reduction of $HAuCl_4$ and the Pd shell may be formed by reducing H_2PdCl_2 using ascorbic acid [61] or sodium borohydride [13], or a galvanic replacement reaction of Cu [62]. Even though a variety of methods have been reported to prepare the Au/Pd crystalline core-shell nanoparticles with different size and shapes, the corresponding reference of polycrystalline hollow Au/Pd core-shell is rare. As the previous mention, the polycrystalline hollow core-shell nanoparticles demonstrated highly catalytic ability and durability. In this dissertation, the hollow Au/Pd core-shell nanoparticles were proposed and anticipated to exhibit superior catalytic properties on FAO as well.

The primary application of the Au/Pd core-shell nanoparticles is for FAO reaction; however, the detailed mechanism of FAO reaction is still in debate so far. To date, the reaction pathways of FAO were considered as dual-pathways [63]. One is dehydrogenation pathway through a direct conversion to CO_2 product and the other is dehydration pathway which generates CO as an intermediate that is adsorbed on the catalytic surface. For Pd and Pd-based materials, the pathway is generally expected as the dehydrogenation pathway. However, the detailed mechanism still needs to be understood for development of advanced catalysts for FAO in DFAFCs.

1.2.3 The Au/Pt Core-shell Nanoparticles for ORR

Au-based core-shell nanoparticles are also extensively developed for oxygen reduction reaction (ORR), especially using Pt as the catalytic material. The particle size of Pt catalysts [27] around 3.5 nm was reported to reach maximum mass activity and

specific activity for oxygen reduction reaction. Pt based catalysts (Pt-M, where M=V, Cr, Fe, Co, Ni, Cu) [64-69] have already demonstrated their superior activities toward ORR over pure Pt in polymer electrolyte membrane fuel cells (PEMFCs). In particular, among these efforts toward improvement of ORR ability, de-alloyed PtCu demonstrated the highest activity [70]. However, there is a concern about stability of these catalysts in acid since the dissolutionof Cu occursduring potential cyclic tests. The hollow Au/Pt core-shell nanoparticles were believed to be a promising candidate due to the advantages previously mentioned.In this study, the ORR activity and long-term durability of our hollow Au/Pt core-shell nanoparticles were discussed to verify the merit of our Au based core-shell nanoparticles.

In this dissertation, the Au/M (M=Pd and PtCu) core-shell nanoparticles synthesized via galvanic replacement of Cu by Pd or Pt on hollow Au nanoparticles were explored as electrochemical catalysts. Two kinds of catalysts have been developed and studied: 1) Au/Pd core-shell nanoparticles applied in FAO reaction, serving as both catalysts and SERS substrate for observing electrochemical reaction. 2) Au/PtCu core-shell nanoparticles as cathodic material were used in ORR.

The rest of this dissertation is organized as follows: Background information about the general synthesis methods will be introduced in Chapter 2. The detailed synthesis process and electrochemical properties of Au/M (M=Pd and PtCu) are described in Chapter 3 and Chapter 4, respectively. The impact of Au core to the structure and electrochemical properties are explored in Chapter 5. The mechanism of FAO on Au/Pd core-shell nanoparticles will be investigated in Chapter 6. Finally, conclusion is summarized in Chapter 7.

Chapter 2

Background Information

The development of proton exchange membrane fuel cell (PEMFC) cannot be widely spread and commercialized primarily due to costly Pt catalysts, combustible hydrogen as the fuel, and difficult storage and transportation of hydrogen. Alternatively, direct methanol fuel cells (DMFCs) employing methanol as fuel alleviate the drawback of hydrogen with the advantages of safe transportation and convenient usage; however, methanol is toxic and its high crossover rate through membrane jeopardizes both fuel efficiency and cell performance. Exploration of the next generation fuel cell system is a challenge to improve fuel cell efficiency and safety, as well as reduce cost.

2.1 Literature Review of DFAFCs

2.1.1 Introduction of DFAFCs

The first DFAFC was developed in 1996 by Weber et al. [71] using formic acid as the fuel. The research found that formic acid is an ideal alternative fuel source than methanol because of the following reasons[11]:

- Improved safety as fomic acid has been used as a food additive[2];
- Reduced fuel crossover through the membrane;
- High theoretical open circuit potential (~1.48 V) than methanol (~1.2 V);
- Alleviated catalyst poison due to reaction intermediates (i.e., CO);
- Allowable high concentration of fuel;

Since the membrane electrode assembly (MEA) applied in PEMFC adopted Pt based materials as the catalysts, Pt based materials were initially chosen as catalysts for DFAFCs as well. In 2002, Masel's group [3] was the pioneer to introduce direct formic acid fuel cells (DFAFCs) system. Their DFAFC can generate high current density up to 134 mA cm^{-2} and power density around 48.8 mW cm^{-2} by using high concentration formic

acid (12 M) with platinum black as the anodic catalyst. The FAO mechanisms were also investigated. The electrooxidation of formic acid on Pt-based catalysts are considered as dual pathways [72-74]: dehydrogenation and dehydration. For the dehydrogenation, formic acid was only oxidized to CO_2 without including CO intermediate [4]:

$$HCOOH + Pt^o \rightarrow Pt^o + CO_2 + 2H^+ + 2e^- \quad (2\text{-}1)$$

However, the dehydration pathway includes CO as the intermediate:

$$HCOOH + Pt^o \rightarrow Pt - CO + H_2O \rightarrow CO_2 + 2H^+ + 2e^- + Pt \quad (2\text{-}2)$$

From the reaction pathway, it was found that CO may impede the active sites on the Pt-based catalyst surface and hence reduce the efficiency of DFAFCs. Later, Masel group compared the FAO activity on Pt, Pt/Pd, and Pt/Ru catalysts and found that Pd enhanced the rate of the FAO via the direct reaction mechanism, i.e., the dehydrogenation pathway; however, Ru suppressed the direct pathway [4]. After that, the supported (i.e., on carbon) or unsupported Pd catalysts have attracted great interest due to the high activity than Pt based materials in DFAFCs. Pd catalyst (Pd black) was found to generate higher performance (271mW cm^{-2} at 30°C for 3M FA) [5]. Ha et al. reported that 20 wt.% Pd/C (145 mW cm^{-2}) showed a higher mass specific current (per gram) than the Pd black [7] due to smaller Pd particle size. To date, intense researches [1, 8-10] have focused on synthesizing of highly active Pd based catalysts to optimize the efficiency of DFAFCs system. However, stability of the Pd catalysts in formic acid is still not comparable to that of Pt catalysts due to the following reasons:

- Pd catalysts are easily corroded in formic acid solution [75]
- CO may be generated to poison Pd active sites during FAO

The developments of highly active and stable Pd catalysts are crucial for the DFAFCs application.

2.1.2 Catalysts of Au-Based Core-Shell Nanoparticles

The advantages of hollow Au based core-shell have been discussed in Chapter 1. In this section, the synthesis of Au nanoparticles and Au based core-shell nanoparticles will be introduced.

2.1.2.1 Synthesis of Au Nanoparticles

Nano-size Au particles have attracted lots of attentions due to their superior physical and chemical properties which are applied in many fields such as optical [76], catalysts [42], and biomedical materials [77]. There are notable synthesis methods [42-44, 76-83] to control size and structure of Au nanoparticles, as these geometric factors are considered to significantly affect their properties. In this part, we only discussed two structures - the spherical and hollow Au.

In 1857, Michael Faraday discovered colloidal Au via reduction of tetrachloroaurate ($AuCl_4^-$) by phosphorus in carbon disulfide (CS_2) [78]. The most popular method to prepare Au nanoparticles was later developed in 1951 using the so-called "Turkevitch method" [79] via the following reaction:

$$6AuCl_4^- + C_6H_8O_7 + 5H_2O \rightarrow 6CO_2 + 24Cl^- + 6Au^0 + 18H^+ \quad (2\text{-}3)$$

where citrate serves as not only a reduced agent but a stable agent to the Au nanoparticles, and the average particle size is around 20 nm. After that, the Brust-Schiffrin method [80] was developed in 1994 as a breakthrough to facilely synthesize dispersed and size-controllable Au nanoparticle with thermal and air stable properties. In liquid-liquid phase, the thiol ligands acted as a strong binder between Au and S, tetraoctylammonium bromide as the phase-transfer reagent allowed $AuCl_4^-$ to transfer into toluene, and $NaBH_4$ within dodecanethiol acted as a reducing agent:

$$AuCl_{(aq)}^- + N(C_8H_{17})_4^+(C_6H_5Me) \rightarrow N(C_8H_{17})_4^+ AuCl_4^-(C_6H_5Me) \quad (2\text{-}4)$$

$$mAuCl_4^-(C_6H_5Me) + nC_{12}H_{25}SH(C_6H_5Me) + 3me^- \rightarrow 4mCl_{(aq)}^- + [Au_m(C_{12}H_{25}SH)_n](C_6H_5Me) \quad (2\text{-}5)$$

Another seeded growth method to fabricate uniform spherical Au nanoparticle in a large range was using ascorbic acid as the reductant and sodium citrate as the stabilizer. Figure 2-1 showed the synthesized Au nanoparticles with different particle size [83].

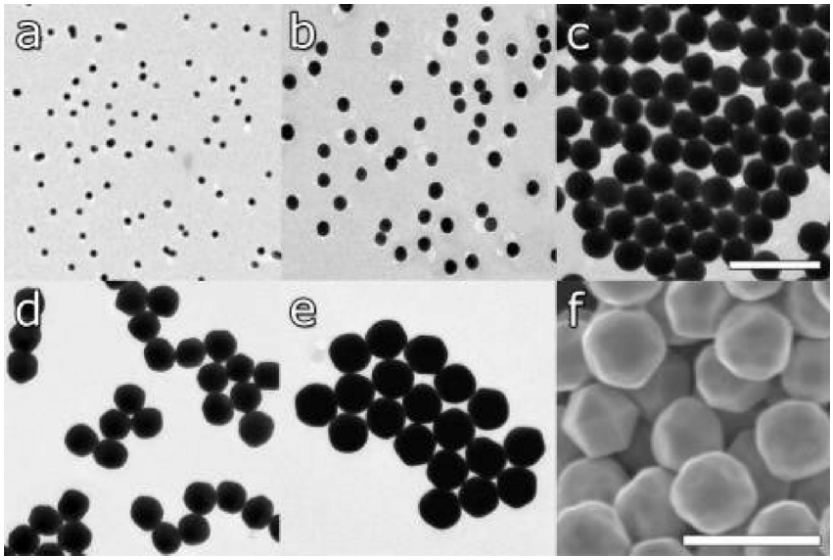

Figure 2-1 TEM images of Au nanoparticles (a) 15 ± 2 nm, (b) 31 ± 3 nm, (c) 69 ± 3nm, (d) 121 ±10 nm, (e) 151 ± 8 nm, and (f) 294 ± 17 nm. Scale bar from a-c: 200 nm; d-f: 500 nm [83].

For hollow Au nanoparticles, in 2006, Zhang et al. reported controllable hollow Au nanoparticles (Figure 2-2) [84] by sacrificial galvanic replacement of Co nanoparticles.

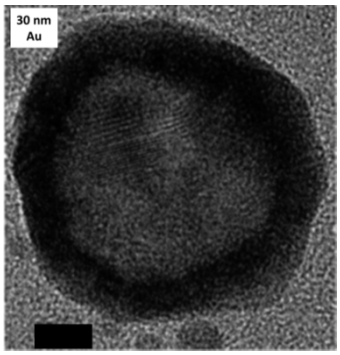

Figure 2-2 TEM image of single hollow Au nanoparticle and the scale bar is 5 nm [84].

Au nanoparticles of different sizes demonstrate unique optical properties due to their surface plasmon resonance (SPR) shown in Figure 2-3. Control of particle size and layer thickness using different parameters such as concentration of cobalt chloride, sodium borohydride, sodium citrate, reductant, and capping agent has been shown to significantly alter the light absorption spectra.

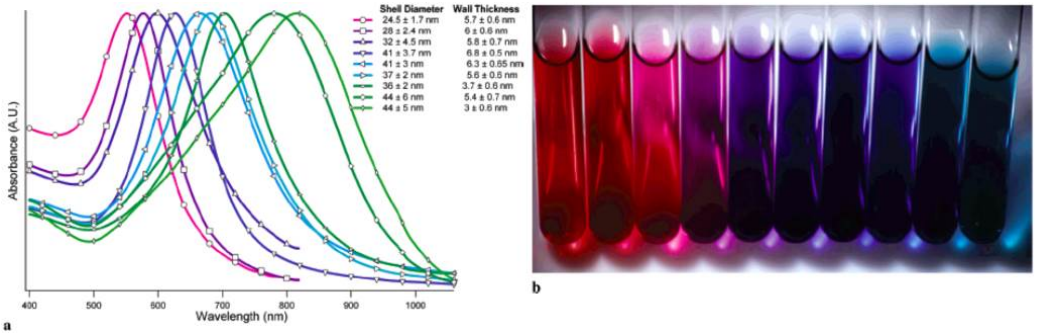

Figure 2-3 (a) UV-Vis spectra of hollow gold nanoparticles with different size, and (b) The color range varies with different Au size [84].

In 2009, a facile synthesis method for hollow Au nanoparticles was developed by Hao's group [85] using evolved hydrogen nanobubbles inside an alumina membrane via electrodeposition method [86] shown in Figure 2-4. The channel diameter of the alumina membrane is about 300 nm and the size of each branch varies from 20 nm to 200 nm.

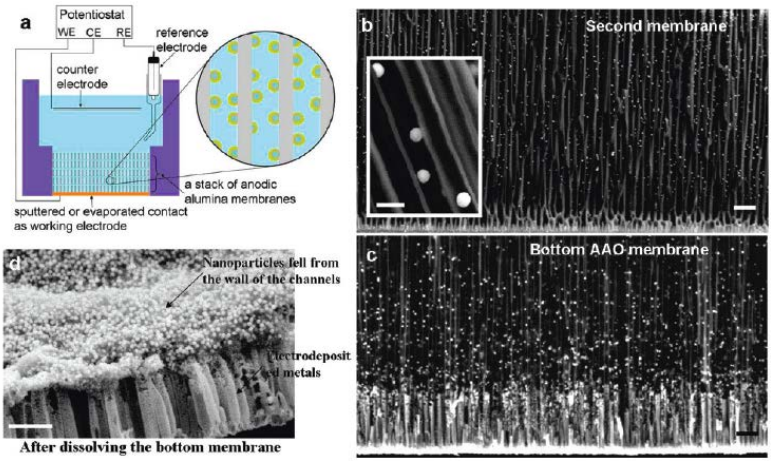

Figure 2-4 (a) Scheme of three electrode system, (b,c) SEM images of bottom and second membrane of AAO after electrodeposition showing Au nanoparticles formed on the channel, and (d) Particles on the top of electrodeposition metal with bottom coated with Cu layer around 400 nm. The scale bar is 1 μm and 200 nm for inset in (b), respectively [86].

In brief, the hollow Au nanoparticles were reduced from the surface of saturated hydrogen nanobubbles. The discharge of the gold sulfite complex follows the steps:

$$Na_3Au(SO_3)_2 \rightarrow 3Na^+ + Au(SO_3)_2^{3-} \quad (2\text{-}6)$$

$$Au(SO_3)_2^{3-} \rightarrow Au^+ + 2SO_3^{2-} \quad (2\text{-}7)$$

The Au^+ ion underwent the disproportionation reaction due to the low stability of gold sulfite at the pH value smaller than 8:

$$3Au^{1+} \rightarrow Au^{3+} + 2Au \quad (2\text{-}8)$$

Au^0 and Au^{3+} ions existed in the solution become turbid as a result of colloidal precipitation and finally decomposed. The stability can be improved by adding stabilizing additives due to the spontaneous decomposition. The hollow Au nanoparticles with applied potentials from -0.7 V to -0.85 V (vs. Ag/AgCl) were shown in Figure 2-5. Since

the hollow structure is composed of a poly-crystalline shell and gases can diffuse easily, they have potentials applied in sensors, drug deliveries, and catalysts [55, 56, 87].

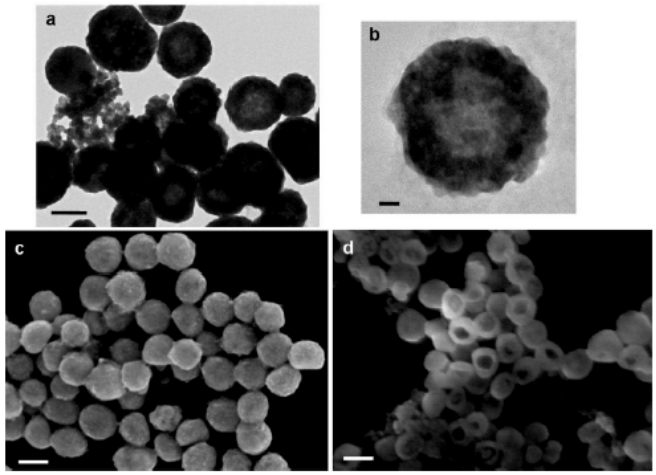

Figure 2-5 (a,b) TEM images of hollow Au nanoparticles, and (c,d) SEM images of hollow Au nanoparticles before and after ion-milling. The scale bar for (a,c,d) is 100 nm and 10 nm for (b) [86].

2.1.2.2 Au/Pt Core-Shell Nanoparticles

The conventional method to synthesize Au/Pt core-shell nanoparticles is to fabricate an inner Au core first and then covered by a Pt shell [88-91]. For example, Wang et al. [92] produced two kinds of Au/Pt core-shell structures - dendritic and spherical nanoparticles by first synthesizing 4 nm Au cores from $HAuCl_4$ reduced by $NaBH_4$ and then followed boiling in ascorbic acid and H_2PtCl_6. By controlling molar ratio of Au and Pt, the component and size of Au/Pt nanoparticles can be adjusted as shown in Figure 2-6.

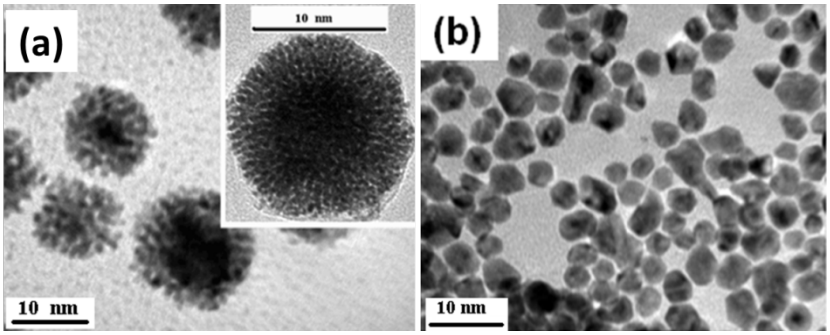

Figure 2-6 TEM images of (a) dendritic (b) conventional Au/Pt at molar ratios 1:3 [92].

In addition, another synthesis method similar to the one previously mentioned is a one-pot approach which depends on different metallic reduction potential. For example, Au/Pt nanocolloids [93] shown in Figure 2-7 were fabricated in a mixed solution of H_2PtCl_6, $HAuCl_4$, Pluronic F127, and ascorbic acid with various ratios by sonication. The applied sonication can decrease the particle size and make a uniform size distribution. The growth mechanism of Au/Pt nanocolloids depends on their different reduction potentials as follows:

$$AuCl_4^- + 3e^- \rightarrow Au + 4Cl^- \qquad +1.00 \text{ eV vs. SHE} \quad (2\text{-}9)$$

$$\left[PtCl_6\right]^{2-} + 2e^- \rightarrow \left[PtCl_4\right]^{2-} + 2Cl^- \qquad +0.68 \text{ eV vs. SHE} \quad (2\text{-}10)$$

$$\left[PtCl_4\right]^{2-} + 2e^- \rightarrow Pt^{2-} + 4Cl^- \qquad +0.76 \text{ eV vs. SHE} \quad (2\text{-}11)$$

where SHE stands for standard hydrogen electrode. During the reduction, Au ions become the Au core in a short time and later covered by the Pt dendritic nanowires as Figure 2-7 shows.

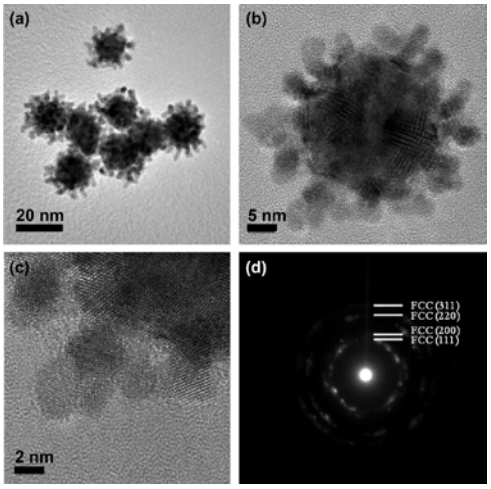

Figure 2-7 Au/Pt nanocolloids (a) low-magnification (b) high-magnification (c) HR-TEM of Pt shell (d) Selected-area electron diffraction (SAED) patterns from Pt shell [93].

Other common synthesis methods involve creating a Cu layer on the outside of Au cores and then being replaced by Pd via galvanic replacement due to their different reduction potential. For example, Yancey et al. [94] synthesized Pt dendrimer-encapsulated nanoparticles on glassy carbon electrode which involves underpotential deposition (UPD) of Cu on the Au cores and replacement of Cu by Pt as shown in Figure 2-8. This method provided a facile and controllable ways to tune the size and thickness of the nanoparticles.

Figure 2-8 Scheme of UPD/galvanic exchange approach for Au/Pt dendrimer-encapsulated nanoparticles [94].

Besides, the Ag layer was chosen to be a sacrifice layer [95]. Xie's group [96] first coated Ag on Au surface and then Ag was replaced by Pt in a H_2PtCl_6 solution to fabricate unique Au/Pt core-shell nanoparticles shown in Figure 2-9.

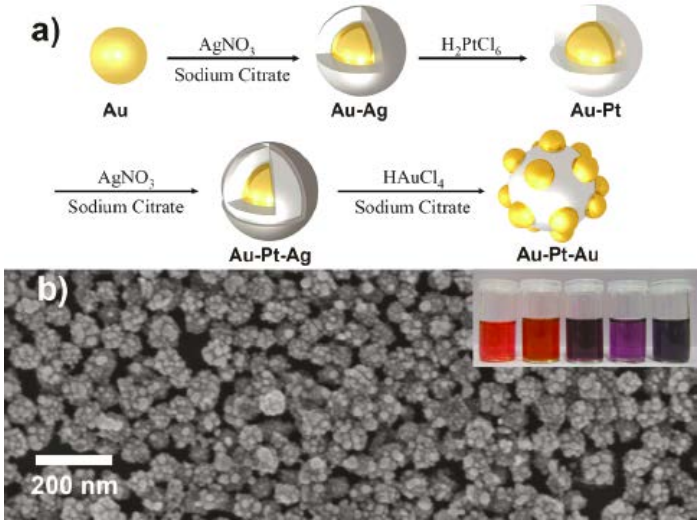

Figure 2-9 (a) scheme of synthesis process (b) SEM image of Au/Pt/Au core shell nanoraspberries [96].

2.1.2.3 Au/Pd Core-Shell Nanoparticles

The synthesis methods for Au/Pd core-shell nanoparticle are similar to those for Au/Pt nanoparticles, but are rarely reported. There are several unique methods reported using gold as the nucleation centers. First, gold seeds were created from $HAuCl_4$ using sodium citrate and mixed with H_2PdCl_4 at 4°C in an ice bath. Then, ascorbic acid was slowly added in the solution with stirring to reduce Pd and later the color became black brown shown in Figure 2-10 [61]. Size of the gold seeds was controlled by solution concentration. The lower the Au concentration, the larger Au size will be. The dispersion of Pd layer can be controlled by H_2PdCl_4 concentration and reaction temperature [51].

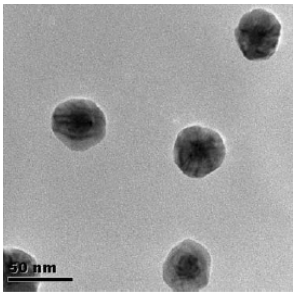

Figure 2-10 TEM image of Au/Pd core-shell nanoparticles by Hu et al.[51].

One-pot synthesis of Au/Pd nanooctahedra was presented by Lee's group in equal ratio of $HAuCl_4$ and K_2PdCl_4 with cetyltrimethylammonium as a reductant and stabilizer. The solution was heated up to 90°C to control the shape and size of the particles. Due to their different reduction potentials of Au (Au^{3+}($AuCl_4^-$/Au, +1.002V vs. SHE) and Pd^{2+} ($PdCl_4^{2-}$/Pd, +0.591V), Au will be reduced earlier than Pd when the applied potential is increased. In Figure 2-11, the SEM (a) and TEM (b) images showed clear octahedral shapes and Figure 2-11c indicated the nanocrystalline structure of the Pd. High-angle annular dark field scanning TEM (HAADFSTEM) in Figure 2-11d pointed out the distribution of Pd and Au which is confirmed by its mapping images in Figure 2-11e [97].

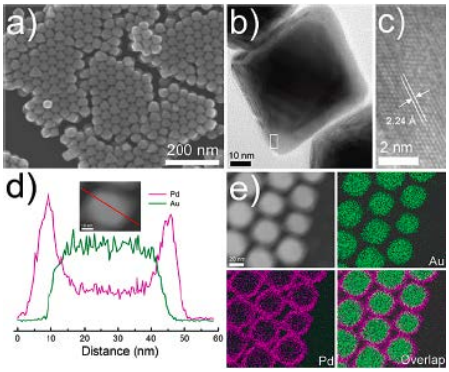

Figure 2-11 (a) SEM (b) TEM (c) HR-TEM of Pd shell (d) HAADFSTEM (e) mapping images from HAADFSTEM of Au/Pd nanooctahedra [97].

For core-shell structures, the shape of the outside layer can be tuned by the inner core. Yang et al. [98] used octahedral gold nanocrystals as the seed to induce the growth of Pd shell. In brief, by controlling the amount of Au nanocrystals (reduced from $HAuCl_4$ using cetyltrimethylammonium chloride in ice-cold $NaBH_4$ solution) and then mixed with CTAB, H_2PdCl_4, and ascorbic acid. The different shape of Au-Pd nanocrystals can be easily achieved as shown in Figure 2-12. Comparing with the previous synthesis method for Au/Pd core-shell nanoparticles, hydrothermal method does not use any reducing agent. Kuai et al. [13] successfully fabricated Au/Pd core-shell nanoparticles by this method, in which $HAuCl_4$, H_2PdCl_4, PVP, and $NH_3 \bullet H_2O$ were mixed and heated up to 180 °C for 12 hours without adding any surfactant. In this method, the thickness, dispersion and shape of the Pd layers were difficult to control.

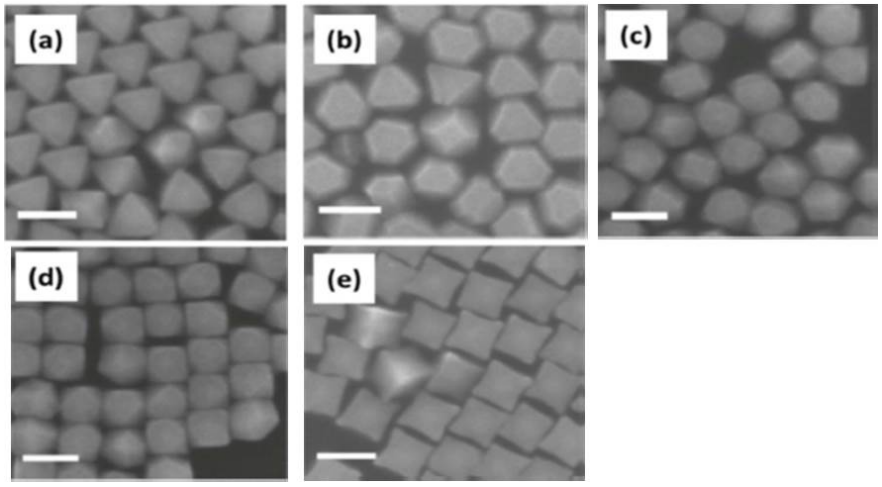

Figure 2-12 SEM images of Au/Pd core-shell nanocrystals (a) octahedral (b) truncated octahedral (c) cuboctahedral (d) truncated cubic and (e) concave cubic shapes. The scale bar is 100 nm [98].

2.1.3 Applications of Au Based Core-Shell Nanoparticles

2.1.3.1 FAO on Au/Pd Core-Shell Nanoparticles

A typical cyclic voltammogram of FAO on Pt in Figure 2-13 demonstrated five waves which were identified and assigned by Okamoto et al.[99, 100]. Three peaks were identified in the positive scan: peak I at ~0.6 V, peak II at ~0.85 V, and peak III at ~1.45 V. In the negative scan, two peaks were found: peak IV at ~0.71 V and peak V at ~0.47 V. These peaks can be attributed the following reactions:

Peak I appeared due to the direct pathway of FAO:

$$HCOOH + * \rightarrow HCOO^{*} + H + e^{-} \quad (2\text{-}12)$$

$$HCOO^{*} \rightarrow CO_2 + H^{+} + e^{-} + * \quad (2\text{-}13)$$

$$H_2O + CO^{*} + * \rightarrow H_2O^{*} - CO^{*} \quad (2\text{-}14)$$

The asterisk stands for an adsorption site. The overall reaction of peak I is suppressed by the formation of CO.

$$HCOOH + * \rightarrow CO^{*} + H_2O \quad (2\text{-}15)$$

Peak II indicated the oxidation of the adsorbed CO (indirect path):

$$H_2O^{*} - CO^{*} \rightarrow CO_2 + 2H^{+} + 2e^{-} + 2* \quad (2\text{-}16)$$

It also can be expressed as:

$$CO^{*} + H_2O^{*} \rightarrow CO_2 + 2H^{+} + 2e^{-} + 2* \quad (2\text{-}17)$$

The oxidation of H_2O with surface oxide and hydroxide formation occurs simultaneously:

$$H_2O + * \rightarrow OH^{*} + H^{+} + e^{-} \quad (2\text{-}18)$$

$$H_2O + * \rightarrow O^{*} + 2H^{+} + 2e^{-} \quad (2\text{-}19)$$

Peak III may be due to Eq. 2-12, Eq. 2-13, and Eq.2-19 on the oxidized surface:

$$OH^{*} \rightarrow O^{*} + H^{+} + e^{-} \quad (2\text{-}20)$$

Peak IV is due to direct pathway of FAO on clean and reactive surface.

Peak V appears due to a combination of surface rearrangement, decreasing FAO rate and increase of the heterogeneous non-faradaic reaction of Eq. 2-15

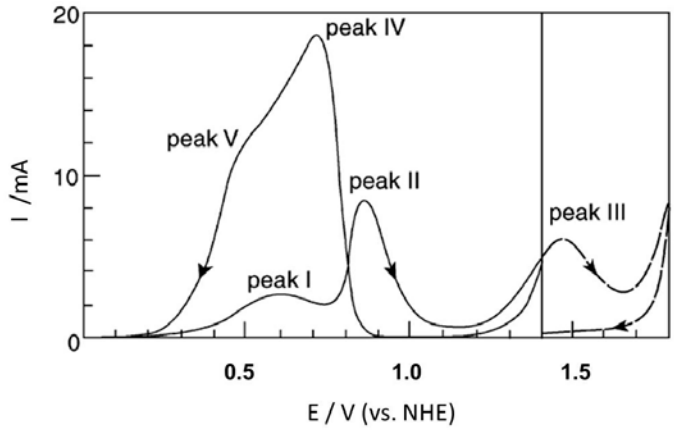

Figure 2-13 The oxidation of formic acid of Pt in 0.1 M H_2SO_4 and 0.5 M HCOOH mixed solution with 100 mV/s scan rate [99].

Au/Pd core-shell nanoparticles have attracted great attention due to their unique geometric and electronic effect by tuning thickness, roughness and size of the inner Au core and the outer Pd shell, because Au is considered as a promoter to the electrocatalytic oxidation [101]. However, reports on AuPd as FAO catalyst are rare [38-40]. Zhou et al. [38] reported higher mass-activity of Au@Pd/C (average size:7.0 nm) than Pd/C (average size: 3.8 nm) in 3 M FA+0.1 M $HClO_4$ solution. At 0.3 V (vs. Ag/AgCl), the current density of Au@Pd/C nanoparticles was 0.78 A mg^{-1} and Pd/C was 0.57 A mg^{-1}. Besides, the peak currents of the Au@Pd/C and Pd/C nanoparticles were 1.06 and 0.58 A mg^{-1}, respectively. Hong et al. [40] synthesized highly active Au/Pd core-shell nanocrystals (Au:Pd=4:1) and showed that Pd surface area specific activity of the Au/Pd nanocrystals was 9.8 mA cm^{-2} which is more than doubled that of the Pd

nanocrystals (4.1 mA cm^{-2}). In addition, the mass activity of the Au/Pd nanocrystals and Pd nanocrystals were 0.35 A $mg^{-1}_{(Au+Pd)}$ and 0.24 A mg^{-1}_{Pd}, respectively, which implied that adding Au promotes the catalytic abilities.

2.1.3.2 Simulation of FAO

A mathematical model for the anode of fuel cells provides a further understanding of electrooxidation of fuels on the catalysts and hence predicts the possible reactions in the system. The studies on direct methanol fuel cells system [102, 103] based on Pt-based materials successfully predicted the electrooxidation of the methanol in different conditions (e.g. concentration, cross-over...etc) by converting the possible chemical reactions into the simulated equations. In these chemical reactions, the adsorbed CO and OH were considered as the intermediates that contributed to the majority of current in the system. The voltammetric current of CO oxidation on Pt(111) simulated by Orts et al. [104] predicted the relationships between the CO coverage and current intensity. In brief, the CO adsorbed on a honeycomb lattice of Pt(111) was easily oxidized at a lower coverage (1/3); however, a higher CO coverage impeded the oxidation reactions.

For FAO on Pt-based material, Mukouyama et al. [105] reported formate-involved pathway resulting in formate directly oxidized to CO_2. Furthermore, the impact of formate on FAO in Pt(111)/H_2O system was carried out by Wang et al.[106]. They adopted density functional theory (DFT) to probe the reaction between the solid/liquid interface by considering adsorption energy and solvation energy. Figures 2-14 (a-h) show the simulated structure of HCOOH on the Pt(111) surface in combination with the calculated adsorption energy. There are several important results from the DFT modeling: (1) HCOOH adsorbed on the Pt(111)/H_2O with O-down configuration and directly degraded to CO_2 when Pt surface is clean; (2) The CH-down configuration of HCOOH is stable at

the interface in the presence of formate with large energetics (-0.2 eV); (3) HCOOH directly degrades while the Pt surface is pre-adsorbed with formate; and (4) From Figure 2-14(i), CH-down configuration with lower barrier (0.45 eV) is prone to break CH-bond easily and OH-bond of the HCOOH can promote the CO_2 formation.

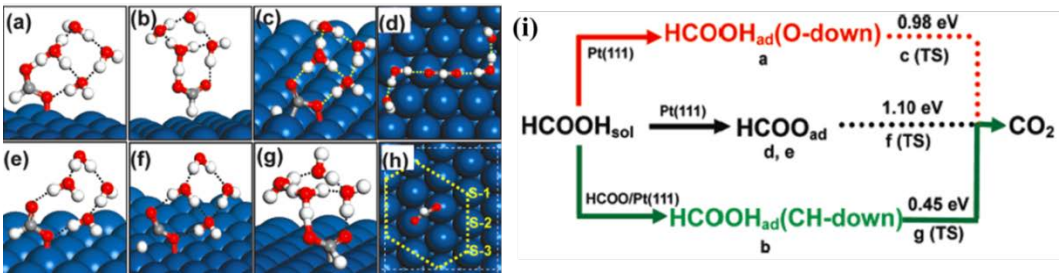

Figure 2-14 DFT structures for adsorbed states (red: O; white: H; grey: C) (a) HCOOH-$(H_2O)_4$ of O-down configuration, (b) HCOOH-$(H_2O)_4$ of CH-down configuration, (c) transition state (TS) for the C-H splitting of HCOOH-$(H_2O)_4$ in the O-down configuration, (d) HCOOH-$(H_2O)_4$ of bidentate configuration, (e) HCOOH-$(H_2O)_4$ in the monodentate configuration (f) TS for the C-H splitting of HCOOH-$(H_2O)_4$, (g) TS for the C-H splitting of HCOOH-$(H_2O)_4$ in the CH-down configuration, (h) neighboring sites of formate on Pt (111), and (i) three pathways of FAO [106].

Gao et al. [107] confirmed the same finding that the formate serves as the reactive intermediates in FAO and water promotes the C-H dissociation by decreasing the O-H barrier of HCOOH. Although formate is considered as one of the reactive intermediate, bridge-bond formate cannot be the main pathway for the majority of current density as indicated by Xu et al. [108]. The possible mechanism can be expressed as follow:

$$HCOOH + Pt \xrightarrow{k1} Pt - COOH_{ad} + H^+ + e \xrightarrow{k2} CO_2 + 2H^+ + 2e \qquad (2\text{-}21)$$

$$j_{ox} \approx j_{direct} \propto k_1 C_{HCOOH}(1 - 2\theta_{formate}) \qquad (2\text{-}22)$$

where $-COOH_{ad}$ is the reactive intermediate after breaking C-H bond of HCOOH on Pt. The Eq.2-22 represents the Bulter-Volmer kinetics which are derived from the experiment and simulation results considering formic acid adsorption as the direct pathway. Lovic et al.[100, 109] reported a kinetic study of FAO on Pt/C catalysts. In his work, the rate determining step followed Eq. 2-23 and Eq. 2-24 under the Temkin conditions. Eq. 2-23 can be expressed as:

$$\exp\left(\frac{r\theta_{HCOOH}}{RT}\right) = K_0 C_{HCOOH} \tag{2-23}$$

where the Θ_{HCOOH} is the coverage of HCOOH (~ 0.5), C_{HCOOH} is the formic acid concentration, k_0 is the equilibrium constant of adsorption and r is the Frumkin interaction parameter (~20-60 kJ mol^{-1}). If the surface coverage was considered $HCOOH_{ads}$ and CO_{ads}, the current density can be written:

$$i = Fk_a(1-\theta_{CO})\theta_{HCOOH}\exp\left(\frac{\alpha_a FE}{RT}\right) \tag{2-24}$$

where k_a is the anodic heterogeneous rate constant for Eq. 2-23, α_a is the anodic transfer coefficient. Besides, k_a is a function of Θ_{HCOOH} according to Frumkin's model by considering Gibbs free energy of the adsorption and the free energy of activation. It can be expressed as:

$$k_a = k_{a,0}\exp\left(\frac{\alpha_a r\theta_{HCOOH}}{RT}\right) \tag{2-25}$$

when $r\Theta_{HCOOH} >> 0$, the activation energy of the anodic direction was reduced and the surface oxidation of $HCOOH_{ad}$ is improved; on the other hand, if $r < 0$, the attraction to the adsorbed molecules increases decreasing the surface reaction. Combination of Eq. 2-24 and Eq. 2-25 yields:

$$i = Fk_{a,0}(1-\theta_{CO})\theta_{HCOOH}\exp\left(\frac{\alpha_a r\theta_{HCOOH}}{RT}\right)\exp\left(\frac{\alpha_a FE}{RT}\right) \quad (2\text{-}26)$$

Eq. 2-26 was partially substituted by Eq. 2-23, i.e.,:

$$i = k(1-\theta_{CO})\theta_{HCOOH}C_{HCOOH}^{\alpha_a}\exp\left(\frac{\alpha_a FE}{RT}\right) \quad (2\text{-}27)$$

The equation shows the current density of FAO relies on concentration of formic acid, and the surface coverage of HCOOH and CO.

Unfortunately, the FAO simulation on Pd-based material is rarely discussed to date and the development of Pd-based FAO simulation is necessary for further understanding and improving the DFAFCs system.

2.1.3.3 ORR and Au/Pt Core-Shell Nanoparticles

In proton exchange membrane fuel cells, ORR is the cathodic reaction. The kinetics of ORR is slow and it determines the overall cell efficiency. In order to increase the cell efficiency, a cathode catalyst for ORR is necessary. Pt and Pt-based materials are the best candidates [110-117] to date. Pd and Pd-based catalysts are rarely reported [118-122] due to their slightly lower oxygen reduction activity than Pt [123]. The method to evaluate ORR catalysts is using rotating disk electrode (RDE) and so-called Koutecky-Levich equation [124, 125]. The detail calculation will be shown in chapter 4.

Pt and Pt-based material have been widely studied as the cathode catalysts for ORR. The possible reactions shown in Figure 2-15 involve multi-electron process and different reaction intermediates [124], i.e.,

$$O_2 + 4H^+ + 4e^- \rightarrow H_2O \quad (2\text{-}28)$$

$$O_2 + 2H^+ + 2e^- \rightarrow H_2O_2 \quad (2\text{-}29)$$

$$H_2O_2 + 2H^+ + 2e^- \rightarrow 2H_2O \quad (2\text{-}30)$$

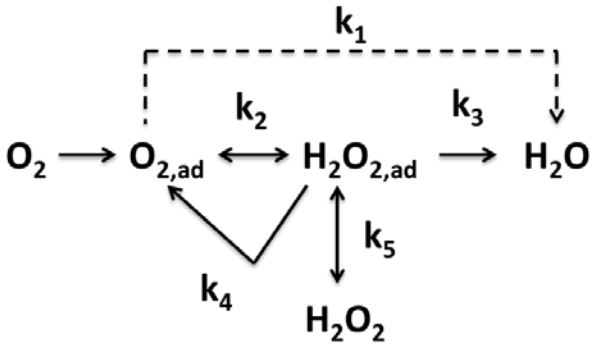

Figure 2-15 The ORR mechanism on Pt catalyst [124].

where O_2 can be directly reduced to H_2O through a four-electron pathway with a rate constant of k_1, or become adsorbed H_2O_{2ad} via a 2 electron pathway at k_2 rate constant. The H_2O_{2ad} can be reduced to H_2O at a rate constant of k_3, or decomposed to O_2 ad on the electrode surface at a rate constant of k_4, or desorbed to H_2O_2 in the solution at a rate constant of k_5.

In particular, Norskov et al. [123] reported two possible reaction mechanisms of ORR on Pt catalysts. Both of the equations depend on the potential.

(1) Dissociative mechanism (low current density range):

$$\frac{1}{2}O_2 + * \rightarrow O^* \tag{2-31}$$

$$O^* + H^+ + e \rightarrow OH^* \tag{2-32}$$

$$OH^* + H^+ + e \rightarrow H_2O + * \tag{2-33}$$

where * denotes a Pt surface site. O_2 breaks the O-O bond and acquires two electrons to form water.

(2) Associative mechanism (high current density range):

$$O_2 + * \rightarrow O_2^* \tag{2-34}$$

$$O_2^* + H^+ + e \rightarrow HO_2^* \quad (2\text{-}35)$$

$$HO_2^* + H^+ + e \rightarrow H_2O + O^* \quad (2\text{-}36)$$

$$O^* + H^+ + e \rightarrow OH^* \quad (2\text{-}37)$$

$$OH^* + H^+ + e \rightarrow H_2O + e \quad (2\text{-}38)$$

This mechanism doesn't involve H_2O_2. O_2 adsorption doesn't break the O-O bonding and acquires four electrons to form water.

The core-shell structures of Au/Pt nanoparticles have attacked lots of attention due to their tunable ORR activities [126-129]. By increase of Pt layer thickness, the Au/Pt nanoparticles ORR activity can be optimized with a four-electron reduction and direct H_2O formation. The enhanced ORR activity for Au/Pt core-shell nanoparticles could attribute to an electrostatic interaction between core and shell, providing stabilization to the Pt shell. In addition, the electro-donating effect could happen due to difference of electronegativities between Au (2.28) and Pt (2.54) [129]. Zhai et al. [126] reported that the Au/Pt nanoparticles (controllable Pt layer by underpotential deposition) exhibited the 4 electron reduction path with 5 Pt layers and the Tafel slope was -119 mV/dec.

Wang et al. [130] built a model to describe the ORR kinetic currents by assuming that the intrinsic exchange current and Tafel slope are independent of anion adsorption. Also, they considered the site blocking and electronic effects of OH adsorption from the $HClO_4$ solution in the model. The kinetic current, j_k , can be calculated from the following equation:

$$\frac{1}{j} = \frac{1}{j_k} + \frac{1}{j_l} \quad (2\text{-}39)$$

where j_l is the diffusion-limited current, and j is the measured current density. So, the kinetic current can be expressed as:

$$j_k = -j_0\left[\exp(2.303\eta/b) - \exp(-2.303\eta/b\frac{1-\beta}{\beta})\right] \quad (2\text{-}40)$$

where β is the transfer coefficient for the cathodic reaction, b is the Tafel slope, and overpotential η=E-E^0.

For the geometric site-blocking effect, the term of $(1-\gamma\theta)^m$ were added into Eq. 2-40; on the other hand, $-\varepsilon\theta$ was treated for electronic effect. Therefore, the kinetic current can be written as:

$$j_k(E) = -j_0^*(1-\gamma_{OH}\theta_{OH}(E))^m \exp(2.303(E - E^0 - \varepsilon_{OH}\theta_{OH}(E)/b^*)) \quad (2\text{-}41)$$

where γ, ε, and m are the site-blocking, energy coefficients and number of Pt sites in the rate determining step, and j_0^* and b^* are the intrinsic exchange current and Tafel slope, respectively. The combined fitting and experimental result showed that the Tafel slope deviates from its intrinsic value in $HClO_4$ solution.

2.1.3.4 SERS of Au Based Core-Shell Nanoparticles

The sensitive SERS as an in situ diagnostic tool was developed in mid-1970 which was applied in many areas such as biology, chemistry, and electrochemistry. After 1996, the enhancement of weak Raman scattering of transition metal (e.g., Pt, Pd, Fe, Ni...) can be achieved by 10 to 1000 times by incorporating Au or Ag. In order to investigate the Au-based metallic catalytic abilities on FAO in this study, we borrowed CO as a effective probe to evaluate CO electro-oxidation via surface enhanced Raman scattering technique. CO may be a poisoning intermediate during the FAO reaction.

Using the state of art SERS method, we can further understand the influence of structural and electronic changes on electrochemical oxidation of CO.

For Au/Pt Nanoparticles:

After mid-1970, SERS has been employed to study nanostructure of nanomaterials [96, 131-134], especially the core-shell structure. It has been reported that strong surface plasmon resonance (SPR) of the Au-core can enhance the Raman signal of the outer Pt layer. The intensity of Raman scattering based on Placzek's polarizability theory can be expressed as follows[53]:

$$I_{mn} = \frac{4352.3}{c^4} I_0 (v_0 - v_{mn})^4 \sum_{\rho\sigma} \left| (\alpha_{\rho\sigma} mn) \right|^2 NA\Omega Q T_0 T_m \qquad (2\text{-}42)$$

where N is the density per cm^2 of adsorbed molecules, I_0 is the laser power, A is laser beam illuminated area (cm^2), Ω is the solid angle of the collection optics, Q is the detector efficiency, Tm is throughput of the dispersion system, and T_0 is the transmittance of the collection optics. In addition, the SPR intensity relates to the electromagnetic field. For example, Figure 2-16 shows the decay of the field with increasing distance away from the Au-core, suggesting a thinner Pt layer is necessary for the stronger SRES intensity [53, 135].

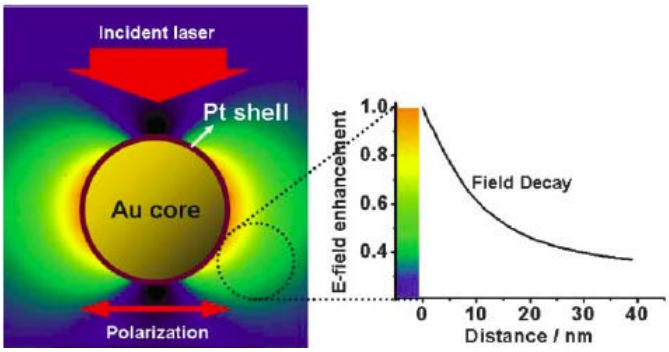

Figure 2-16 Electromagnetic field distribution of Au/Pt core-shell nanoparticles [53].

Also, the SERS intensity depends on the structure as shown in Figure 2-17, which emphasizes the superiority of the Au/Pt core-shell nanoparticles. Zhang et al. [136] reported in situ SERS of CO electro-oxidation in the range of 1850-2350 cm^{-1} from -0.3 V to 0.4 V (vs. saturated calomel electrode, SCE).The C-O stretching frequency started at -0.3 V (2050 cm^{-1}), red-shifted to 2067 cm^{-1} at 0.3 V, and disappeared at 0.4 V as shown in Figure 2-18. The non-smooth curves may due to the roughness of particle surface.

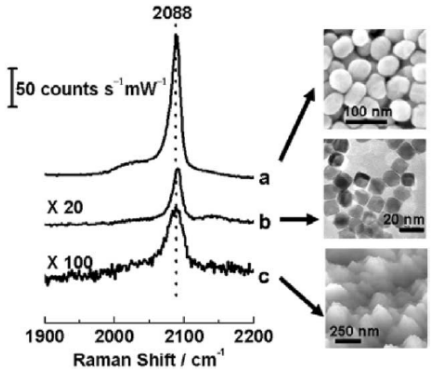

Figure 2-17 SERS of adsorbed CO on (a) Au/Pt core-shell nanoparticles, (b) nanocubic Pt, and (c) roughened Pt electrode [53].

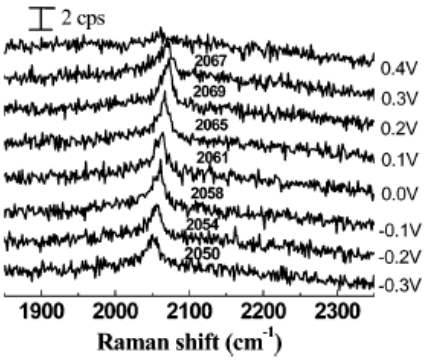

Figure 2-18 In situ SERS of Au/Pt on glassy carbon electrode in 0.1 M $HClO_4$ (after 30 min CO adsorption). Excitation: 632.8 nm. Acquisition time: 100 second [136].

For Au/Pd Nanoparticles:

SERS of Pd boosted by metals such as Au has been reported in many studies [23, 47-49, 137]. The Raman enhancement factor depends on surface roughness, concentration of the molecules (e.g., R6G [47], pyridine...etc.), Raman intensity at certain frequency (e.g., v_1 mode...etc.) [51]. The SERS of CO adsorbed Au/Pd core-shell nanoparticles in Figure 2-19 showed three bands of bridge-bonded CO (1951 cm^{-1}), linearly-bonded CO (2062 cm^{-1}), and Pd-C vibration of the bridge-bonded CO, respectively [46, 50, 52]. All of these peaks starting from -0.4 V (vs. SCE) disappeared above the 0.55 V, suggesting the complete removal of CO from Pd surface. The setup of SERS measurement was normally conducted under the excitation line of 632.8 nm from a He-Ne laser. The Raman signals were collected at a long working length (8 mm) objective with 50x magnification (some group used 20X~100X) while the laser was directed to the sample surface.

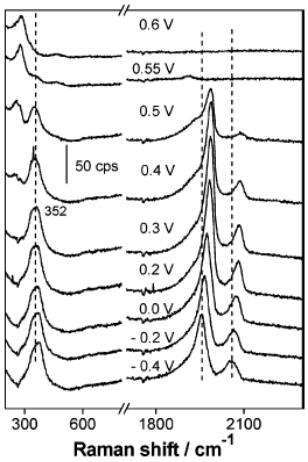

Figure 2-19 In situ SERS of CO adsorbed on Au (12 nm) / Pd (0.25 nm) core-shell nanoparticles from -0.4 V to 0.6 V (vs. SCE) [52].

The efficient enhancement of the SERS via tunable structures of core and shell has been also investigated [52-54]. For Au/Pd core-shell nanoparticles, increase of Au-core size [52] and decrease of Pd-shell thickness [53] both can efficiently improve the

SERS intensity as shown in Figure 2-20. The result showed that the bridge bonded CO shifted to higher wavenumber with the increased Pd thickness which may hinder SPR of the Au core; on the other hand, the intensity of the bridge bonded CO increased with the increased size of the Au cores because of the enhanced SPR effect. Therefore, the larger Au particle size may enhance the SPR effect to efficiently probe possible changes during the reaction. For the reported results, the SPR enhancement was observed from Au nanospheres up to 90 nm in diameter; there is no report currently on hollow Au/Pd core-shell nanoparticles.

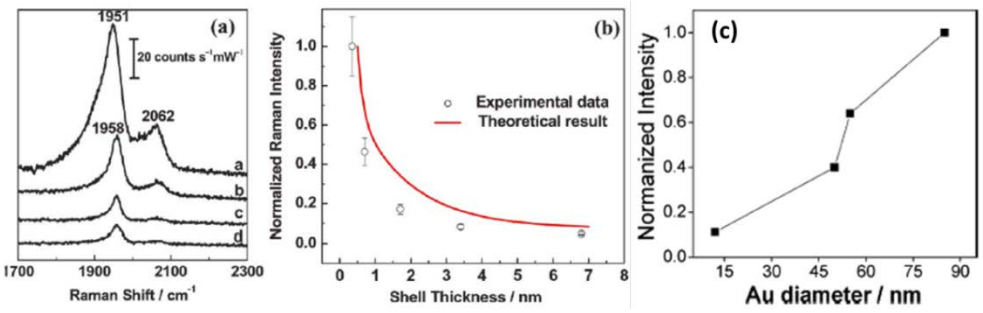

Figure 2-20 (a) SERS of CO adsorbed on 55 nm Au/Pd with different thickness a: 0.7 nm, b: 1.4 nm, c: 2.8 nm, and d: 6.8 nm; (b) Intensity of CO adsorbed on different Pd thickness, and theoretical result from FDTD calculation [53]; and (c) Intensity of bridge-bonded CO adsorbed of different Au-core size [52].

2.2 Enhancement Factor in Electrochemical Activity

Although the Pd catalysts demonstrate high electrocatalytic activity in FAO reaction, there are concerns about their electrocatalytic activity and stability in the acid environment. Therefore, it is necessary to further understand the electrocatalytic properties and reaction mechanism of the Pd catalyst to resolve these problems

2.2.1 Factors Affecting the Electrocatalytic Activity and Stability

It was reported that Pd catalysts with ~ 3 nm demonstrate a high activity due to the large electrochemical surface area; however, the area specific activity and stability were compromised. In order to boost the catalytic activity and stability, bimetallic Pd based materials were developed to increase their catalytic properties such as PdV, PdAu, PdMo, PdW, PdCr, PdNb, and PdTa [11].

2.2.2 Catalytic Properties

The bimetallic catalysts in either alloy or core-shell structures demonstrate superior activities than their metallic component. The enhancement of the catalytic ability could be attributed to two fundamental effects: electronic, and geometric effect [138].

2.2.2.1 Geometric Effect

Most of the studies focus on surface structure of metal nanoparticles at different sizes. Mayrhofer et al. [138] studied the particle size effect on formation of OH adlayer, CO oxidation, and ORR. In brief, the predominantly adsorbed hydrogen on Pt catalysts (Pt-H_{upd}) interactions are weaker at smaller particle sizes; however, smaller particle size will enhance the adsorption of OH ions. The adsorbed OH is a promoter to CO oxidation as follow:

$$CO + OH^- \rightarrow CO_2 + 2e^- + H^+ \quad (2\text{-}43)$$

The more OH generates from smaller particle size in ORR, the oxophilicity increases resulting in decreased specific activity since OH effectively blocks the active sites for reaction of oxygen dissociation. The same phenomenon was demonstrated by Antolini's group [139] by controlling Co content in the Pt-Co/C catalysts. Their result suggests that the increased Co content in the catalysts would decrease the Pt-Pt bond distance, therefore, the ORR activity will drop due to lower the amount of adsorbed OH.

Wilson et al. [30] reported that the geometric effect happens with particle larger than 1.5 nm while electronic effect occurs with the size less than 1.5 nm of Pd nanoparticles toward hydrogenation of allyl alcohols. Baldauf et al. [1] reported that the FAO activity of Pd overlayers depends on their thickness and crystallographic orientation. They compared Pd(111), (100), and (110) overlayers of various thickness on Au(hkl) and Pt(hkl) in FAO. Pd(100) showed the highest FAO activity, and the Pd film on Pt(hkl) with 2~3 layers exhibited higher activity than that on Au(hkl).

Geometric effect involves arrangement of surface atoms with surface strain (compression or expansion) [28, 29]; this phenomenon is distinct within few atomic layer [41]. AuPd alloy (Pd less than 1 monolayer) shows 4% lattice strain [140]. The surface strain had been already confirmed as an important factor to affect the d-band structure (d-band center) which will strongly alter the adsorbate state due to the environment changes [28]. On the other hand, the catalytic properties of the core-shell structures can be easily engineered. Strasser et al. [41] reported the strain controls the ORR activity using the dealloyed AuPt core-shell nanoparticles (Pt shell/ Pt-Cu core) shown in Figure 2-21. In his study, the strain can be expressed as:

$$s(Pt) = \frac{a_{shell} - a_{Pt}}{a_{Pt}} \times 100 \qquad (2\text{-}43)$$

where a_{Pt} is the bulk Pt lattice parameter, and a_{shell} is determined by anomalous X-ray diffraction. The results showed the compression from the Pt-enriched surface modified the d-band structure to decrease the absorbed energy of reaction intermediates; thus the catalytic activity will be increased.

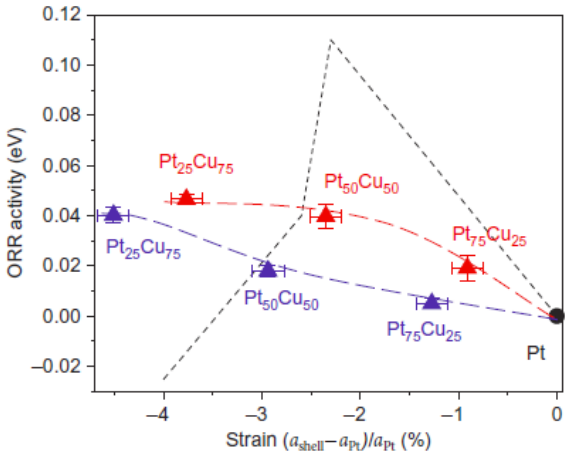

Figure 2-21 The relationship of experimental (red: 800 °C; blue: 950°C) and simulation (dot line) with ORR activity and lattice strain [41].

2.2.2.2 Electronic Effect

Electronic effect (also called ligand effect) is caused by the electronic charge transfer between the two dissimilar metal atoms [35, 41]. Pt-based alloys with Ni, Co, and Fe exhibit better activity than pure Pt because of the modified electronic structure. From the calculated binding energy from density functional theory (DFT), a kinetic model was developed in Figure 2-22 to show that the ORR rate at certain potential (i.e., 0.9V) as a function of a parameter characterizing the catalytic surface-the oxygen chemisorption energy (ΔE_O). The volcano-shaped depends on the rate of the ΔE_O. That means if the oxygen binding is too strong (left of the figure), the rate determining step will be removal of the adsorbed O and OH; otherwise, the weak oxygen binding energy will impede the oxygen dissociation [34]. In the figure, the activity (A) can be expressed as:

$$A = k_B T \ln(r) \tag{2-44}$$

where r is the rate per surface atom per second at 0.9 V (shown in "●"), and k_B is the Boltzmann constant. For the experimental results marked as red dot was given as:

$$A = k_B T \ln(\frac{i}{i_{Pt}}) + A_{Pt} \quad (2\text{-}45)$$

where (i/i_{Pt}) is the Pt current density, and A_{Pt} is the theoretical value for the activity of Pt.

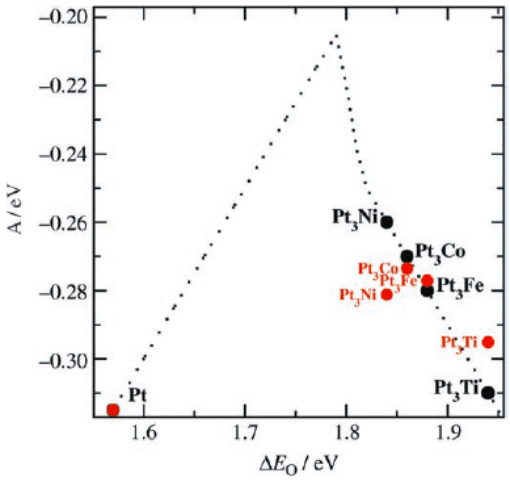

Figure 2-22 DFT model of the activity versus the adsorption energy of oxygen for Pt_3M alloys [34].

The d-band center was measured by using the synchrotron-based high resolution photoemission spectroscopy. A shift of the d-band center at 0.9 V shown in Figure 2-23 indicates that simulated (DFT calculated) d-band center as a function of the oxygen binding energy agrees with the experimental results. The results indicated the catalysts that bind oxygen too strong, the rate will be limited by the removal of the surface oxide, on the other hand, the bind oxygen too weak, the rate will be restricted by the transfer of the electrons and protons to adsorbed O_2.

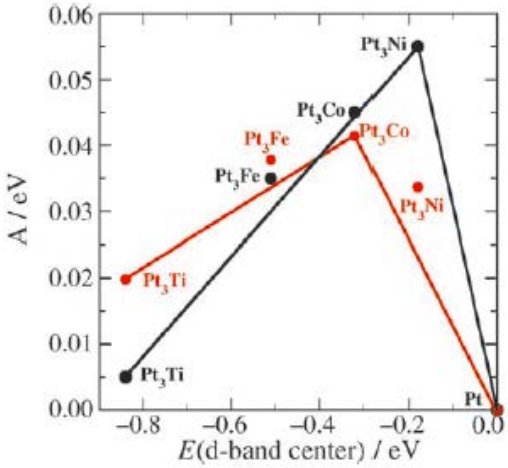

Figure 2-23 The d-band center (relative to Pt) versus the activity.(red: simulation; black: experiment) [34].

For Pt monolayer supported on Au(111), Rh(111), Pd(111), Ru(0001), and Ir(111) surface, the Pt/Pd(111) demonstrates the highest ORR activity than pure Pt reported by Zhang and his co-workers [141]. Their work showed a fine-tuning the electrocatalytic activity of transition metals. From Figure 2-24, the volcano-type curve depicts that the Au(111) with highest the weighted center of the d-band (ε_d) has strong oxygen binding; however, it will impede the O or OH hydrogenation kinetics. Pt/Au (111) may encounter hindered oxygen or OH hydrogenation kinetics due to stronger binding of oxygen atoms and oxygen related species. That is why the activity lower than the pure Pt (111). The Pt/Ru (0001), Pt/Ir (111) and Pt/Rh (111) display less ORR activity due to difficulty to break the O-O bond and promoting the formation of H_2O_2, suggesting an optimal ORR activity is achieved with an optimum balance between O-O bond breaking and O-H bond generating activity [141]. In the figure, the calculated oxygen binding energy (BE_o) is a function of the d-band center ($\varepsilon_d - \varepsilon_F$) of individual Pt monolayer.

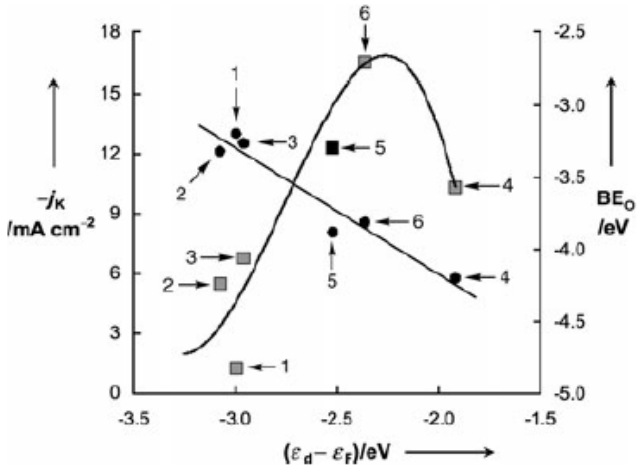

Figure 2-24 Kinetic currents at 0.8 V for ORR (denoted as square) and BE_0 (filled circles) to the d-band center on monolayer Pt / M (M: 1. Ru(0001), 2. Ir(111), 3. Rh(111), 4. Au(111), 5. Pt(111) only, 6. Pd(111)) [141].

In summary, the related discussion merely focused on adding different second metal and changing the shape, size and component of the nanoparticles. There is lack of efficient and tunable structure (i.e. core-shell) to study the geometric and electronic effect for the FAO reaction. Also, there is still a debate on the FAO reaction pathway on Pd materials. In order to clarify the possible mechanisms that affect the electrocatalytic activity and stability of Pd catalysts, we attempt to employ Au-based core-shell structure as the promising platform according to the discussion in chapter 1.

2.2.3 Hypothesis of the Proposed Research

The research taken in this work will help to answer the following questions:

- How do the hollow Au cores influence the stability and durability of the Au-Pd core-shell nanoparticles?

- SERS will be an effective tool to probe surface structure, electronic coupling between Au and Pd, as well reaction intermediates during reactions. How do Raman spectra change upon altering structures or operating conditions (such as voltage)?
- How do Au particle size and surface roughness affect the catalytic activity and stability in FAO reaction?
- Are the electronic coupling and geometric factors acting coherently or independently? Which is dominating? Can they be quantified?
- How the surface coverages of reaction intermediate evolve as the applied potential changes? Can structures of the core-shell nanoparticles change the coverages?

The contribution of this study will help understand the FAO mechanism on Au/Pd core-shell nanoparticle and develop strategies to improve the catalytic ability and stability. The experimental synthesis and study of various hollow Au core-shell nanoparticles in combination with numerical modeling of FAO is to predict the possible reaction pathways and shed lights on enhancement factors in electrochemical activity and durability.

Chapter 3

Synthesis of Au/Pd Core-Shell Nanoparticles for Formic Acid Oxidation

3.1 Introduction

Pd and Pd-based catalysts have been well studied for their superior electrochemical activity on formic acid oxidation (FAO) because the reaction occurs primarily via a direct dehydrogenation pathway through a direct conversion to CO_2 product. However, Pd is unstable in an acid environment. The reported study [142] using XPS confirmed the existence of Pd species at higher valance states (Pd^{4+}) on catalyst surface, especially when the particle size is below ~3nm. This Pd oxidation and subsequent corrosion would therefore result in its deactivation in the DFAFCs environment.

Tailoring catalyst-support interaction has been recently attempted to enhance both electrochemical activity and stability of the Pd catalysts. The enhancement attributes from electronic structure modification of the catalysts by the support, where the d-band center of Pd shifts relative to the Fermi level [143]. However, in most studies the electronic coupling between Pd and the support is not fully assessed and its impact on long-term durability of the Pd-based catalysts has not been studied.

In this chapter, we first report a synthesis method of Au/Pd core-shell nanoparticles with tunable electronic interaction for enhanced activity and durability on FAO. Secondly, we studied the thickness of the Pd shell (coated on the hollow Au nanoparticles), which was varied as the determining factor to tailor the electronic coupling. We believe that the hollow Au core donates electrons to stabilize the Pd shell and thus enhances the electrocatalytic ability and long-term durability.

3.2 Synthesis of Hollow Au Nanoparticles

The synthesis of hollow Au nanoparticles was prepared by an electrodeposition method where Au ions were reduced in the mixed Au solutions at certain potential. The Au solution includes Au^{2+} (Technic Inc.) and Ni^{2+} solution with a ratio 4 to 1 at pH=6.2. From the previous studies [55, 56, 86, 87, 144], the gold nanoparticles were synthesized using the saturated hydrogen nanobubbles (hydrogen bubble nucleation). It is thus essential to explore the suitable applied potential and time for growing the hydrogen nanobubbles. We will briefly discuss the effect of the applied potential and deposited time for the Au nanoparticles.

3.2.1 Effect of Applied Potentials

Hydrogen evolution occurs at -0.55 V (vs. Ag/AgCl) or more negative potentials at pH=6.0. Figure 3-1 shows the hollow Au nanoparticles obtained at the applied potentials between -0.7 V and -0.8 V with uniformly dispersion; however, the wide size distribution of the Au nanoparticles occurred below -0.9 V. Figure 3-2 shows the hollow Au nanoparticles synthesized at -0.7 V for 800 seconds.

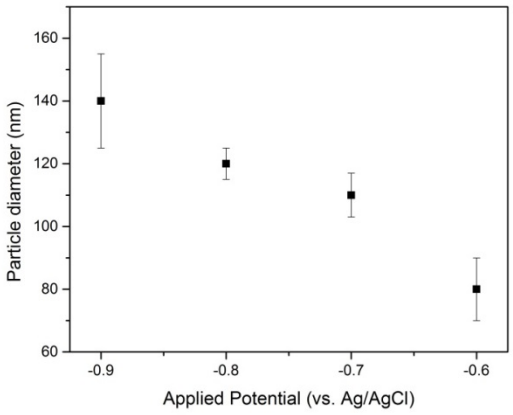

Figure 3-1 The relation of applied potential and the average Au nanoparticle size with error bar.

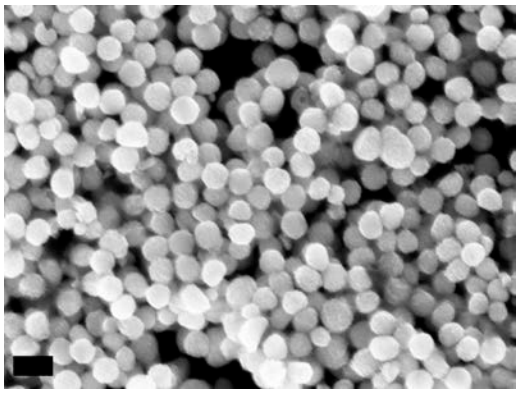

Figure 3-2 SEM image of hollow Au nanoparticles synthesized at -0.7 V (vs. Ag/AgCl) for 800 seconds. The scale bar is 200 nm.

3.2.2 Effect of Electro-deposition Time

Figure 3-3 shows that the size distribution of Au nanoparticles increases with the deposition time at a fixed potential of -0.7 V. It is found that the size of Au hollow spheres become less uniform when deposition time increases, indicating the uniformly-distributed and suitable of Au nanoparticles could be obtained within 800 seconds.

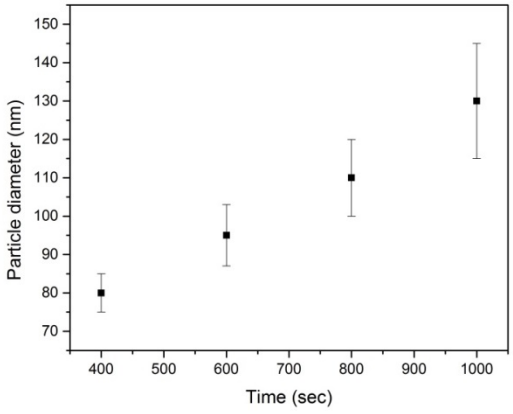

Figure 3-3 The relationship between deposition time and average Au nanoparticle size with error bars at the potential of- 0.7 V.

3.3 Synthesis of Au/Cu Core-Shell Nanoparticles via Electroless Plating

After synthesis of Au nanoparticles, Cu layer will be coated on their surface via an electroless plating method. The method was discovered in 1944 by A. Brenner and G.E. Riddell [145]. Copper, nickel, silver, gold, or palladium can be used on the surface of a variety of materials by means of a reducing chemical electrolyte (bath). Typically, for the electroless Cu plating, an electrolyte containing a metal source ion, reducing agent (formaldehyde), complexant (prevent Cu precipitation), buffer (adjust pH value), and stabilizer (preventing Cu decomposition from bath) is needed. Table 3-1 lists a reprehensive l composition of a Cu plating electrolyte.

Table 3-1 Components of Electroless Copper Plating Baths (Bindra et al. [146])

Reducing agent	Complexant	Stabilizer
Formaldehyde	Sodium potassium tartrate	Oxygen
Dimethylamine borane(DMAB)	Ethylenediamine tetraacetic acid (EDTA)	Thiourea
Sodium hypophosphite	Glycolic acid	2-mercaptobenzothiazole

The reaction of between Cu ions and formaldehyde can be explained by Wangner and Traud's theory [147] of mixed potentials as follows:

$$2H_2C(OH)_2 + 2OH^{-1} \rightarrow 2HCOOH + H_2 + 2H_2O + 2e^- \quad (3\text{-}1)$$

$$\left[CuL_6\right]^{(6n-2)-} \Leftrightarrow Cu^{2+} + 6L^{n-} \quad (3\text{-}2)$$

$$Cu^{2+} + 2e^- \rightarrow Cu^0 \quad (3\text{-}3)$$

where CuL_6 is the copper complex and n is the number of electrons. The total reaction rate according to Eq.(3-2) and Eq. (3-3) is formulated in the following form by Donahue et al.[148]:

$$r = 2.81\frac{[Cu^{2+}]^{0.43}[HCHO]^{0.16}}{[OH^{-}]^{0.70}[EDTA]^{0.04}}\exp.11.5\frac{T-313}{T} \quad (3\text{-}4)$$

The coefficient of formaldehyde and EDTA is low, so the rate depends majorly on concentration of Cu ion and hydroxyl group. We will discuss the effect of the OH^- value (pH value) to the Cu deposition rate in the following section. Figure 3-4 shows the result of electroless Cu plating reaction on different materials. In this simple demonstration, metallic materials appear as good conductive substrates to promote reaction (3-3) (electrons can move easily).

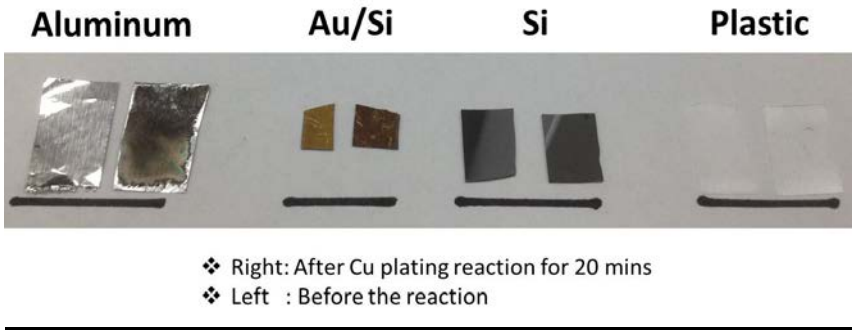

Figure 3-4 Test of Cu plating on different materials.

3.3.1 Effect of pH Value of Cu Electrolyte

In this study, we used the Cu electrolyte which consists of 0.4 M $CuSO_4$, 0.17 M EDTA disodium salt dehydrate, and formaldehyde at different pH value (adjusted by 1M NaOH) at room temperature. The Cu deposition rate was evaluated on a Au coated Si wafer and the results are shown in Table 3-2. The suitable ratio of mixed solutions of

$CuSO_4$, formaldehyde, and NaOH in this study was chosen as 1:1:1 as the baseline condition.

Table 3-2 Cu coating time with various pH values

$CuSO_4$ (ml)	Formaldehyde (ml)	1MNaOH(ml)	pH value	Reaction time on Au wafer (min)
1	1	1	10.42	5 min
1	1	0.9	10.31	5 min
1	1	0.8	10.30	5 min
1	1	0.7	10.06	5 min
1	1	0.6	9.45	5 min
1	1	0.5	9.40	15 min
1	1	0.4	9.32	15 min
1	1	0.3	9.25	15 min
1	1	0.2	9.20	15 min
1	1	0.1	9.13	30 min
1	1	0.09	8.98	40 min
1	1	0.08	8.79	40 min
1	1	0.07	8.58	40 min
1	1	0.06	8.49	60 min
1	1	0.05	< 8.49	More than 2 hours
1	1	0.04	< 8.49	More than 2 hours
1	1	0.03	< 8.49	More than 2 hours
1	1	0.02	< 8.49	More than 2 hours
1	1	0.01	< 8.49	More than 2 hours

3.4 Synthesis of Au/Pd Nanoparticles via Galvanic Replacement

A typical oxidation-reduction reaction (so-called galvanic replacement) will be used to coat different metals as according the following reaction:

$$A + BC \rightarrow AC + B \tag{3-5}$$

where metal A is more active than B. In this study, after coating the Cu layer for a certain time (designed thickness), subsequent replacement of the Cu layer by Pd occurred through a galvanic reaction in an aqueous solution containing 2.53 mM $PdCl_2$. Cu layer

will be replaced by Pd in the $PdCl_2$ solution for 30 minutes according to the following galvanic reaction:

$$Cu_{(s)} + Pd^{2+}_{(aq)} \rightarrow Pd_{(s)} + Cu^{2+}_{(aq)} \quad (3\text{-}6)$$

due to their different standard reduction potentials (Cu^{2+}/Cu : 0.342V; Pd^{2+}/Pd : 0.951V). Table 3-3 shows the standard reduction potentials of certain metals used in this study and Figure 3-5 shows the scheme of core-shell Au/Pd nanoparticle synthesis process.

Table 3-3 Standard Reduction Potential at 298.15K

Equation	E^0(V)
$Cu^{2+} + 2e^- \leftrightarrow Cu_{(s)}$	0.340
$PtCl_4^{2-} + 2e^- \leftrightarrow Pt_{(s)} + 4Cl^-$	0.758
$Pd^{2+} + 2e^- \leftrightarrow Pd_{(s)}$	0.915
$Au^{3+} + 3e^- \leftrightarrow Au$	1.52

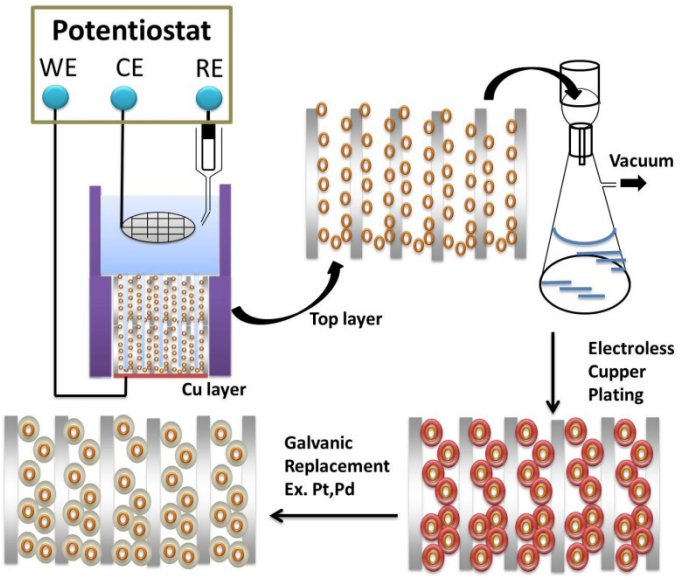

Figure 3-5 The scheme of Au/Pd nanoparticles synthesized process.

3.4.1 Effect of Thickness of Pd Layers

The thickness of the Pd shell depends on thickness of the Cu layer which was controlled by the plating time. Figure 3-6 shows the TEM images of Au/Pd nanoparticles synthesized using different Cu depositing time. These images clearly display the Au core and Pd shell formed by the contrast due to different atomic weights. Figure 3-6a demonstrates island-like Pd domains at the Au surface and the inset shows the Pd nanocrystallites with ca. 0.2356 nm lattice spacing. Figure 3-6(b–d) demonstrates that Cu coating time is an effective parameter to control the Pd shell thickness, and up to 30 nm in shell thickness and 3–6 nm nanocrystallite size can be observed from the TEM images. Figure 3-7 demonstrates the size distribution of Pd nanocrystalline with Cu plating time. Here, we noticed that the largest deviation of Pd thickness existed in the longest Cu coating time.

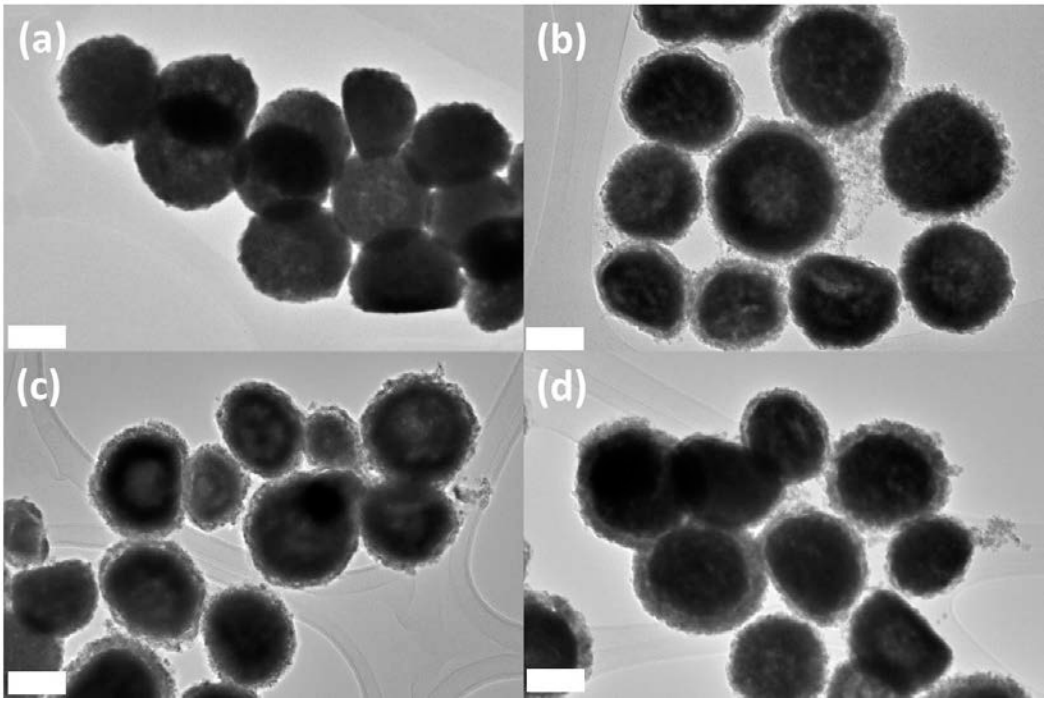

Figure 3-6 TEM images of Au/Pd nanoparticles with various Cu coating time (a) 10 min, (b) 20 min, (c) 30 min, and (d) 40 min. The scale bar is 100 nm.

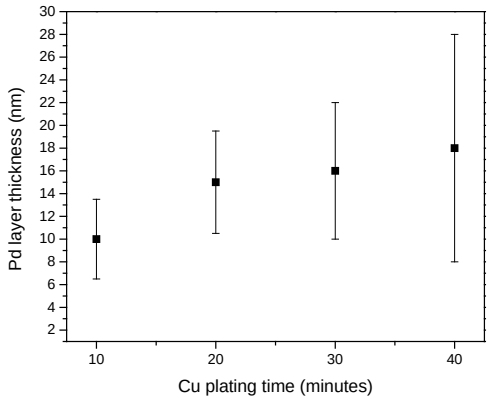

Figure 3-7 The relation of Pd layer thickness and Cu plating time.

3.5 Physical Characterization of Au/Pd Nanoparticles

The structural and electronic properties of the Au/Pd core-shell nanoparticles were examined by X-ray diffraction (XRD) and X-ray photoelectron spectroscopy (XPS), respectively.

3.5.1 XRD of Au/Pd Nanoparticles

In Figure 3-8 the Pd XRD reflection peaks at 40.1°, 46.5°, and 68° correspond to (111), (200) and (220) planes in the fcc structure. In addition, the strong Au reflection peaks at 38.2°, 64.89°, and 77.56° corresponding to (111), (200) and (220) planes suggest that the synthesized core–shell catalysts consist of distinct Au and Pd crystalline components, not alloy phase. There are no identifiable Cu or CuO peaks in the figure, indicating that the Cu layer is totally replaced by the Pd shell. On the other hand, the weak Pd signal, particularly in AuPd10 (Here AuPdX: X means the Cu coating time), is due to the highly dispersed Pd nanocrystalline embedded at the Au surface (Figure 3-6a); while the signal improves in other samples (Figure 3-6 (b–d)) when continuous Pd shells form with increasing Pd thickness.

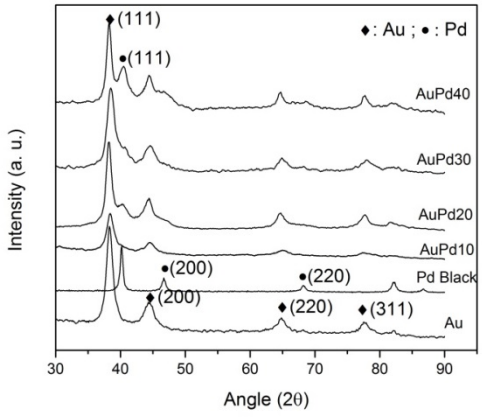

Figure 3-8 XRD pattern of Au/Pd nanoparticles, Pd black and Au samples.

3.5.2 XPS of Au/Pd Nanoparticles

The electronic coupling between the Au core and Pd shell in the Au/Pd catalysts was probed by XPS. Figure3-9a shows that the binding energy of Pd $3d_{5/2}$ in all the Au/Pd nanoparticles slightly shifts to lower energy compared to the Pd black (particle size ~8 nm, from Alfa Aesar). AuPd10 with ΔE=0.52 eV shows the largest binding energy shift while that of AuPd40 is negligible with only 0.08 eV. The shift of the binding energy implies surface electronic modification of the Pd shell resulting from the interaction with the Au core. Lower Pd $3d_{5/2}$ binding energy will result in higher activity of the Au/Pd catalysts than the Pd black, particularly with decreasing Cu coating time. This is because the chemisorption of formate as FAO intermediate on the Au/Pd catalysts is strongly dependent on Pd $3d_{5/2}$ binding energy, which is in agreement with the discussion in reference[149]. Also, the TEM image of Pd black was shown in Figure 3-9b.

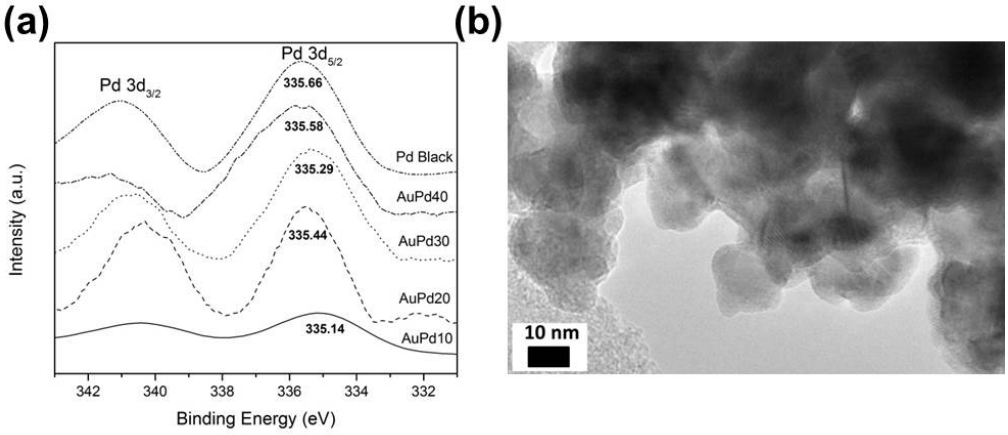

Figure 3-9 XPS spectra of Au/Pd nanoparticles and Pd black.

3.6 Electrochemical Properties of Au/Pd Nanoparticles

Electrochemical measurements were carried out using a Princeton Applied Research 2273 potentiostat in a three electrodes configuration and the rotation working

electrode (Pine Instrument Company) with glassy carbon (area: 0.19635 cm^2), Pt mesh as counter electrode, and the reference electrode via normal hydrogen electrode (NHE) at ambient temperature. Catalyst inks and rotating disk electrodes were prepared according to our previous work[150]. Typically, 15mg of catalysts was mixed with 12 ml DI water and 4.4 ml 5 wt.% Nafion(Ion Power Inc.). The CO-stripping measurement is first absorbed CO at 0.2 V for 900 seconds in CO-saturated 0.1 M $HClO_4$ and then tested CO-stripping cyclic voltammograms (CV) under the 0.1 M $HClO_4$ solution after Ar bubbling for an hour.

3.6.1 Cyclic Voltammetry (CV)

Electrochemical characteristics of these Au/Pd nanoparticles were evaluated by the cyclic voltammetry method. The cyclic voltammogram curves, obtained in 0.1 M $HClO_4$ solution from 0.075 V to 1.2 V (vs. NHE) at 10 mV s^{-1} scan rate, are shown in Figure 3-10aand the current density (J) has been normalized to the electrochemical surface area (ECSA). ECSA was calculated by integrating the hydrogen adsorption peak from CV curves according to equation 3-5 shown in Figure 3-10b.

$$ECSA = \frac{Q_H}{[Pd] \cdot Q_C} \tag{3-5}$$

where Q_H (mC cm^{-2}) is the charge under the hydrogen adsorption peak, [Pd] (g) is the Pd loading on the RDE, and Q_C stands for the adsorption of a monolayer of hydrogen on the Pd surface with a value of 0.21 mC cm^{-2}.The ECSA value is 1.383 cm^2g^{-1} (AuPd10), 1.735 cm^2g^{-1} (AuPd20), 2.035 cm^2g^{-1}(AuPd30), and 3.302 cm^2g^{-1}(AuPd40), respectively. However, in the anodic scan direction, Au/Pd catalysts show higher Pd oxidation current than the Pd black.

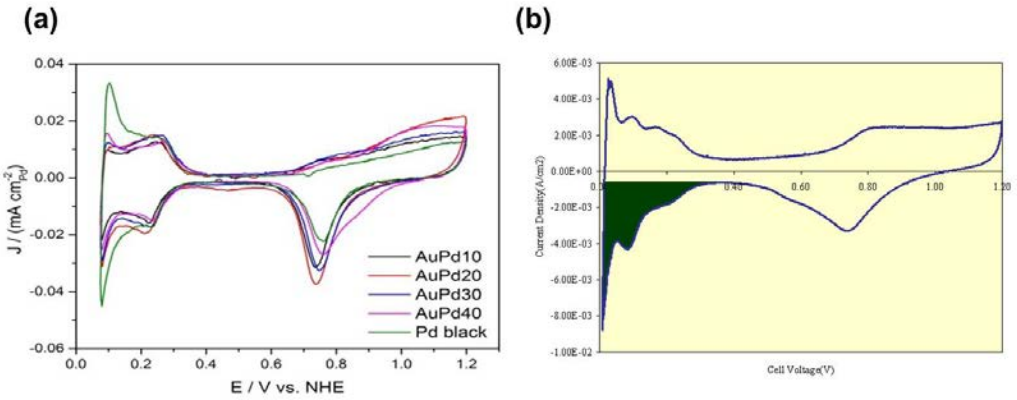

Figure 3-10 CV curves of Au/Pd nanoparticles and Pd black.

3.6.2 CO-Stripping CV

The extent of electronic structure modification in the Au/Pd catalysts can also be probed electrochemically by CO-stripping CV as shown in Figure 3-11. The Au/Pd nanoparticles, especially AuPd40 and AuPd20, display much lower CO oxidation potentials at 0.78 V and 0.79 V, respectively, than the Pd black at 0.9 V. This result demonstrates stronger CO oxidation ability of the Au/Pd catalysts.

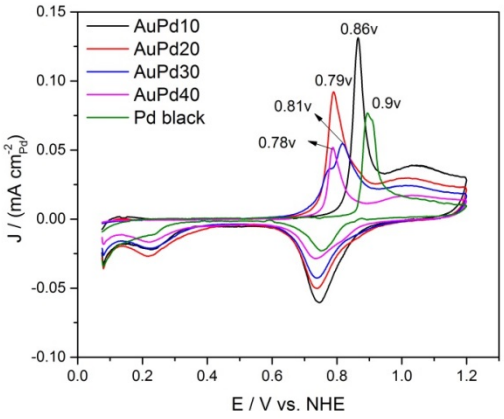

Figure 3-11 CO-stripping CV of Au/Pd nanoparticles and Pd black.

3.6.3 CV of FAO

The FAO reaction of the Pd catalysts was studied in a mixed electrolyte containing 0.1 M $HClO_4$ and 0.1 M HCOOH at 1000 rpm (in order to remove the CO_2 bubble on the electrode). Figure 3-11 shows that Au/Pd10 and Au/Pd20 demonstrated the highest area-specific current density (normalized to the ECSA) in both scan directions. The area-specific current densities of AuPd10, AuPd20, and AuPd30 are close to Pd black between 0.3V and 0.6V; however, AuPd40 is less active. In addition, Au/Pd10 and AuPd20 also demonstrate the highest peak potential (~0.84V) in both anodic and cathodic scans, suggesting that significant hydroxyl coverage on Pd only occurs at very high potential and therefore these catalysts maintain active over a wider potential window without the blocking effect of hydroxyl to Pd. This also indicates that the Au/Pd catalysts are not prone to poising (by hydroxyl groups), in agreement with the XPS results where the Au/Pd catalysts demonstrate lower binding energy (Figure 3-9) [151]. On the contrary, the Pd black shows lower peak potential (0.65V) due to absence of electronic coupling.

In addition, the impact of different concentration of formic acid was discussed in this chapter. Figure 3-12b demonstrates the FAO curve on AuPd10 nanoparticles with various FA concentrations. The result shows that AuPd10 and AuPd20 yield highest peak current density using 0.5M FA. Also, the anodic current at 0.3V demonstrated in Figure 3-12c (vs. NHE) shows that at 0.5M FA the highest current was achieved. This volcano curve distribution may attribute from the reactive sit-blocking effect on the Pd surface in the higher FA concentration. When too many poisons species occupies on the Pd surface, the catalytic efficiency will decrease significantly.

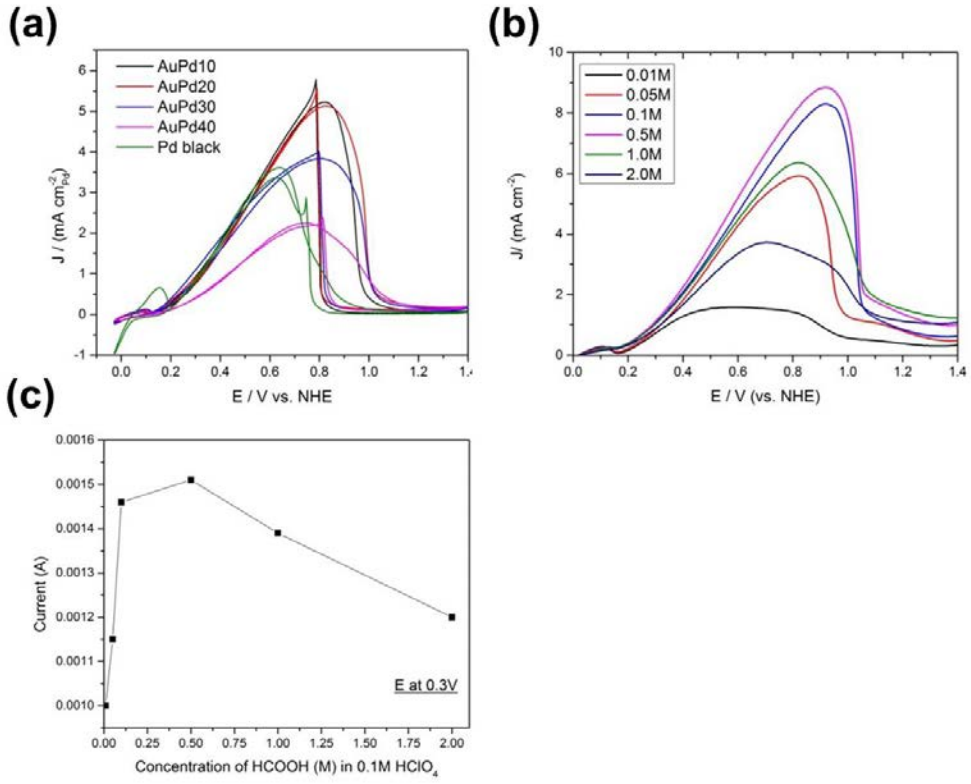

Figure 3-12 FAO curves of (a) Au/Pd nanoparticles and Pd black, (b) Au/Pd10 nanoparticles in various FA concentration, and (c) FAO Current at 0.3 V (vs. NHE) of Au/Pd 10 nanoparticles.

3.6.4 Stability and Durability

The chronoamperometry (CA) test was applied to measure the stability of catalysts in 0.1M HCOOH and 0.1M $HClO_4$ solution for an hour at 0.3V (vs. NHE). Figure 3-13a shows that AuPd20 maintains the highest area-specific current density with little decay, while significant oxidation current loss was observed in the initial 500 seconds for the Pd black.

Durability of the Au/Pd nanoparticles was assessed by the accelerated stress test (AST). The potential was cycled between 0.6V (5 sec) and 0.95V (5 sec) in 0.1M

$HClO_4$ solution up to 14000 cycles and the normalized ECSA value was plotted in Figure 3-13b. Here, the normalized ECSA indicates the relative ECSA loss of the catalysts during AST. The AuPd10 and AuPd20 preserve almost more than 85% of the initial ECSA in the first 7000 cycles and 70% after 14k cycles; on the contrary, the ECSA loss rate for the Pd black is more than doubled in the same range. This demonstrates the superb electrochemical durability of the Au/Pd nanoparticles in the long-term AST. The results in Figure 3-9 also confirm the existence of long-range electronic coupling between the Au core and Pd shell even when the latter is ~ 20nm thick. However, optimum electronic interaction appears to exist for intermediate Pd shell thickness as in AuPd20 and AuPd30. AuPd10 has poorly defined interface between Au and Pd, and therefore geometric factor dominates over electronic contribution in the overall electrochemical activity. In AuPd40, on the other hand, the Pd shell is too thick resulting in diminished electronic coupling between the core and shell.

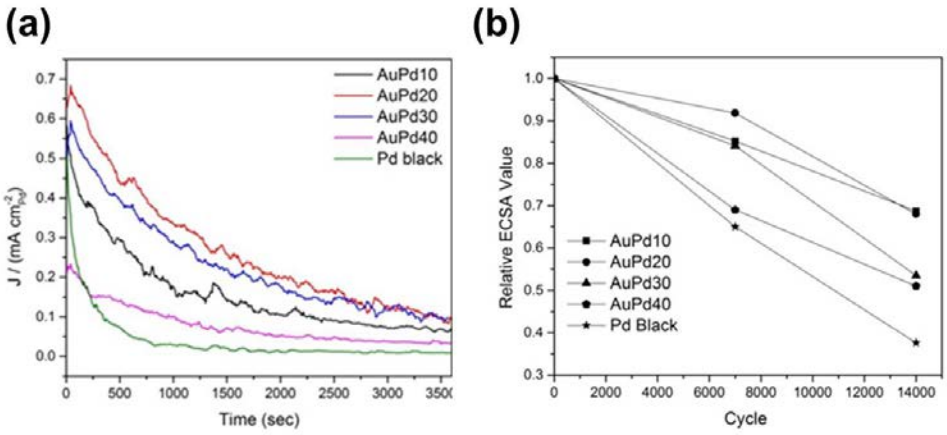

Figure 3-13 Au/Pd nanoparticles and Pd black (a) stability test, and (b) durability test.

Chapter 4

Au/PtCu Core-Shell Nanoparticles for Oxygen Reduction Reactions

4.1 Introduction

In this chapter, the facile synthesis of the Au/PtCu nanoparticles using galvanic replacement of Cu by Pt on Au surface is demonstrated. The Au/PtCu catalysts show well-defined core-shell structure with the PtCu shell and stabilizing Au core. The catalytic properties have been studied by controlling of Cu deposition time (i.e., thickness) and concentration of the K_2PtCl_4 electrolytes. Moreover, the kinetics of oxygen reduction reactions on Au/PtCu nanoparticles were also discussed. As described in chapter 3, the core-shell nanoparticle exhibited superior catalytic properties than commercial catalysts due to their unique structure and electronic configurations. Herein, the Au/PtCu nanoparticles also express superior electrocatalytic activities evaluated from the oxygen reduction reaction (ORR) polarization curves.

4.2 Synthesis of Au/PtCu Core-Shell Nanoparticles

The synthesis of the Au/PtCu core-shell nanoparticles follows the procedure described in our previous study on Au/Pd core-shell nanoparticles. The hollow Au cores were first synthesized using saturated hydrogen nanobubbles as templates. Then a Cu layer was deposited on the surface of Au, using a electrolyte solution consisting of 0.4 M $CuSO_4$, 0.17 M ethylenediaminetetraacetic acid (EDTA) disodium salt dehydrate (99%, Alfa Aesar), and formaldehyde (37%, Aldrich) at pH=10. Subsequently, the Cu layer was replaced with Pt through galvanic replacement by immersing in K_2PtCl_4 (98 wt% Aldrich) solution for 30mins.The process took place according to the reaction:

$$Cu_{(s)} + Pt^{2+}_{(aq)} \rightarrow Cu^{2+}_{(aq)} + Pt_{(S)} \quad (4\text{-}1)$$

Commercial Pt black (99.9%) from Alfa Aesar and Pt/C (TKK, 46.7 wt%) from Tanaka Kikinzoku Kogyo K.K., Tokyo, Japan were used as baseline materials.

Figure 4-1 shows the composition of Pt and Cu in the Au/PtCu 20 catalyst (20 stands for the time of Cu plating, unit: min) immersed in different concentration of K_2PtCl_4 solutions. The compositions of Pt and Cu were measured by inductively coupled plasma mass spectrometry (ICP-MS).The galvanic replacement is believed to be spontaneous due to the large difference in standard reduction potentials of the $PtCl_4^{2-}$/Pt pair (0.74V vs. SHE) and Cu^{2+}/Cu pair (0.34V vs. SHE); however, it was reported[152] that Cu may not be completely replaced by Pt since a critical replacement limit (~ 66 wt%) exists in the process and also the microstructure became more porous. Our results suggest a much higher replacement limit – Pt can reach 84 wt% and Cu is up to 16 wt% in 5mM K_2PtCl_4 solution. Higher concentration of K_2PtCl_4 may not effectively increase the replacement limit since a concentration plateau has been reached as indicated in Figure 4-1.

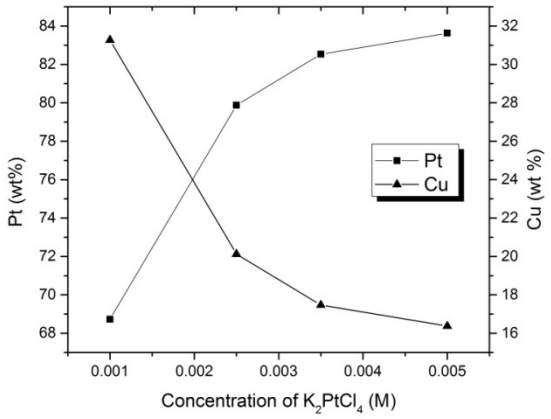

Figure 4-1 Pt and Cu composition of Au/PtCu 20 nanoparticles synthesized in different concentrations of K_2PtCl_4 solution.

4.3 Physics Characterization of Au/PtCu Nanoparticles

4.3.1 XRD of Au/PtCu Nanoparticles

The crystalline structures of the Au/PtCu, the Pt black and Au nanoparticles are studied using X-ray diffraction and the results are shown in Figure4-2. The Au/PtCu 20

catalyst shows distinct Au (111), (200), (200) and (311) phases at 38.38°, 44.72°, 64.75° and 77.87°, respectively; however Pt signal is not clear in the pattern as Pt particles are highly dispersed at the Au surface. The Au/PtCu 40 sample shows not only Au signal but also a broad Pt signal (40.97°) close to PtCu (111) at 41.17° (referred to JCPDS #48-1549) therefore synthesis of the Au/PtCu 40 nanoparticles may result in both pure Pt and PtCu alloy phase.

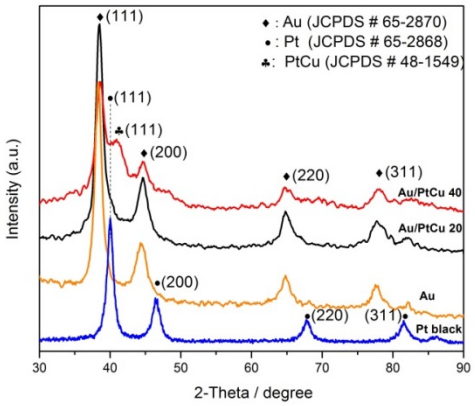

Figure 4-2 X-ray diffraction pattern of the Au, Au/PtCu and Pt black samples

4.3.2 TEM of Au/PtCu Nanoparticles

To further gain insight of the Au/PtCu nanoparticles, HR-TEM images were taken to study structure and morphologies of the samples. In the Figure 4-3a and 4-3b, the inner Au cores (around 150 nm in diameter) show hollow structure manifested by the adjusted z contrast in the TEM images and are enclosed by the PtCu shells with thickness of 25nm (Au/PtCu 20) and 50nm (Au/PtCu 40) in each case. The lattice fringes displayed in the inserted images in Figure 4-3a and 4-3b show the lattice d-spacings of 0.226 nm and 0.230 nm, respectively, for the Au/PtCu 20 and Au/PtCu 40, which are slightly larger than that of Pt (0.2207 nm). The d-spacings are also close to that of PtCu

(0.2191nm) phase though it is possible the PtCu shell may include pure Pt as well. The detailed distribution of Pt metal and PtCu alloy within the PtCu shells is not clear from the available data.

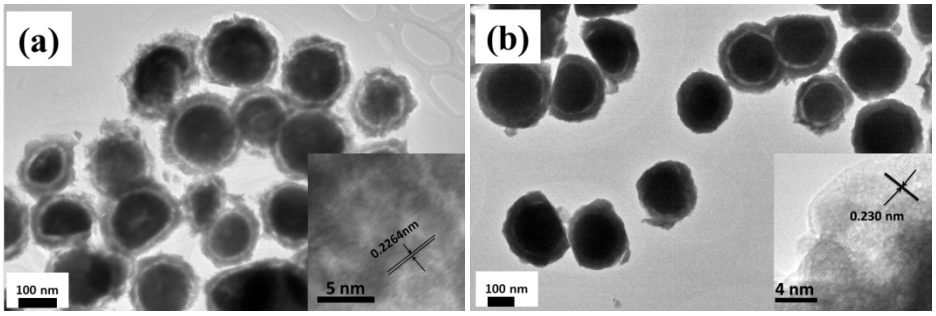

Figure 4-3 TEM images of (a) Au/PtCu 20 and (b) Au/PtCu 40 nanoparticles and inlets are the highly- magnification TEM images of PtCu shell of Au/PtCu samples.

4.4 Electrochemical Properties of Au/PtCu Nanoparticles

4.4.1 CV of Au/PtCu Nanoparticles

The CV curves of the synthesized catalysts (using 3.5 mM K_2PtCl_4) tested in 0.1M $HClO_4$ saturated with Ar are shown in Figure 4-4a. The current density (J) is normalized to the ECSA of Pt. ECSA was obtained from the hydrogen adsorption area (in cathodic scan) according to the following equation:

$$ECSA = \frac{Q_H}{[Pt]Q_C} \tag{4-2}$$

where Q_H (mC cm^{-2}) is the charge under the hydrogen adsorption peak, [Pt] (g) is the Pt loading on the RDE, and Q_c stands for the adsorption of a monolayer of hydrogen on Pt surface with value of 0.21 mC cm^{-2}. The Au/PtCu catalysts show higher oxygen reduction potentials than the commercial catalysts indicating a weak Pt-OH bond in these catalysts. Calculation of ECSA shown in Figure 4-4b from the CV curves indicates that the ECSA

values, from 20.5 to 23.5 $m^2g^{-1}_{Pt}$, of the Au/PtCu 20 is less dependent on K_2PtCl_4 concentration. However, the Au/PtCu 40 (40 min of Cu plating time) employing the 3.5mM K_2PtCl_4 solution shows slightly higher ECSA probably due to increased amount of Cu and therefore Pt. Overall, the Pt/C (TKK 46.7 wt%) shows the highest ECSA (78.21 $m^2g^{-1}_{Pt}$) due to smaller size of the Pt nanoparticles which are well-dispersed on the carbon surface.

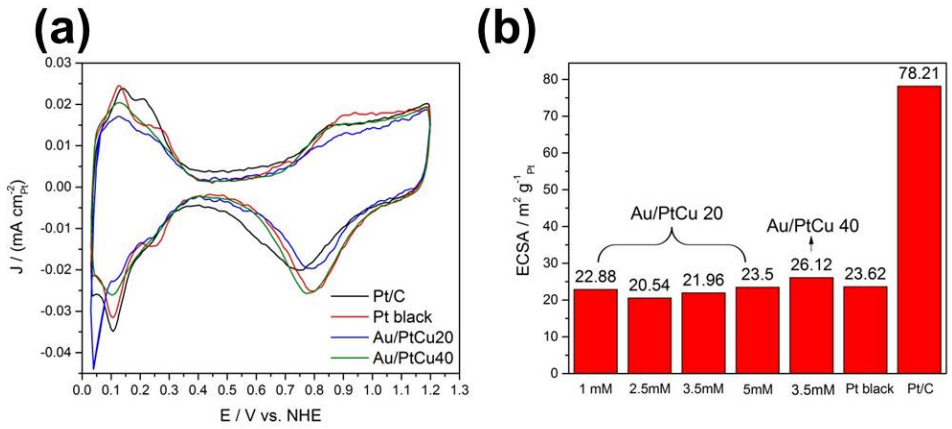

Figure 4-4 (a) CV of four samples in 0.1M $HClO_4$ solution (the Au/PtCu samples were synthesized using 3.5 mM K_2PtCl_4). (b) ECSA comparison between the Pt/C, Pt black and Au/PtCu samples.

4.4.2 Activity Study of ORR

Figure 4-5a shows the ORR polarization curves obtained in 0.1M $HClO_4$ solution at 1600 rpm for the Au/PtCu (using 3.5 mM K_2PtCl_4), Pt/C and Pt black samples with the same catalyst loading. The current has been normalized to Pt electrochemical area for easy comparison. From Figure 4-5a, the limiting current density of Au/PtCu 20 (0.3 mA cm^{-2}_{Pt}) more than doubles those of Pt/C, Pt black, and Au/PtCu40 (~0.125 mA cm^{-2}_{Pt}). According to our previous study[150], the kinetic currents (I_k) are used to estimate the mass and specific activity via mass-transport correction (so-called Koutecky-Levich equation), i.e.,

$$I_k = \frac{I_{lev} \times I}{I_{lev} - I} \quad (4\text{-}3)$$

Where I is the current which measured at 0.9 V, I_{lev} is the diffusion-limited current, and I_k is the kinetic current. The calculated results for the specific activity (SA, mA cm^{-2}_{Pt}) and mass activity (MA, mA μg^{-1}) are displayed in Figure 4-5band4-5c, respectively. The Au/PtCu 20 samples achieve the highest SA value of 0.196 (mA cm^{-2}_{Pt}) at 3.5 mM K_2PtCl_4. At the same concentration of K_2PtCl_4, the Au/PtCu 40 shows even higher SA value. Indeed, the SA value of the Au/PtCu 40 (0.256 mAcm^{-2}_{Pt}) is more than double that of Pt black (0.108 mA cm^{-2}_{Pt})and is enhanced by a factor of ~5compared to the Pt/C (0.0587 mA cm^{-2}_{Pt}). Among the MA values of the Au/PtCu 20 samples shown in Figure 4-5b, the catalyst synthesized using 3.5 mM K_2PtCl_4demonstratesthe highest value (0.043 mA μg^{-1}_{Pt}).Consistently, the Au/PtCu 40 sample synthesized using 3.5 mM K_2PtCl_4achieves even higher MA value of 0.066 mA μg^{-1}_{Pt}, which is more than double that of Pt black and higher than Pt/C as well. The reason why the Au/PtCu 20 and 40 samples prepared in 3.5mM K_2PtCl_4 solution show better catalytic activity toward ORR could be due to the fact that the Cu embedded in the nanocrystalline Pt helps lower the d-band center from the Fermi level of Pt. According to Fouda-Onana et al.[153], 30 at.% Cu in the PdCu alloy could reach the optimum values in Fermi-level and d band width. Though our results in Figure4-1 may indicate lower Cu weight fractions than the reported value; however, it is believed that an optimum balance between electronic structure (d-band center) and geometric factor (particle size) may be achieved in 3.5 mM K_2PtCl_4.

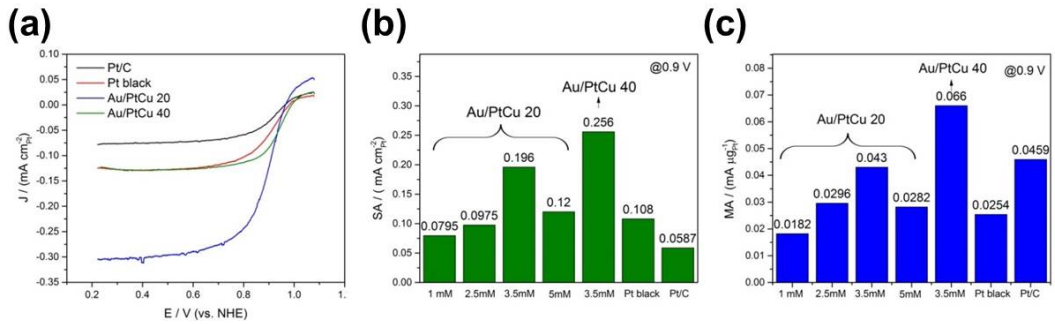

Figure 4-5 (a) Pt area-normalized current density of ORR polarization curves. (b) SA at 0.9Vand (c) MA at 0.9V. Rotation speed at 1600 rpm and scan rate 20mV/s were used.

4.4.3 Kinetics of ORR

Rotated disk electrodes (RDE) used to study the electrode kinetics and mechanisms is a common method to estimate the number of electrons (n) transferred in the chemical reaction[154-156]. For the simple cathodic mechanism:

$$T + ne^{-} \Leftrightarrow K; E^{0'} \tag{4-4}$$

At steady-state, the diffusion rate will be equal to convective transport of A at electrode surface:

$$D_T \left(\frac{\partial^2 C_T}{\partial x^2} \right)_{x=0} = \nu_x \left(\frac{\partial C_T}{\partial x} \right)_{x=0} \tag{4-5}$$

Here, V_x (axial velocity) can be expressed at the electrode surface (x=0) as:

$$\nu_x = -0.510 w^{3/2} \nu^{-1/2} x^2 + 0.333 w^2 \nu^{-1} x^3 \tag{4-6}$$

Where ν is the kinematic viscosity of the solution ($cm^2\ s^{-1}$). The second term is ignored due to low diffusivity for electroactive species. The cathodic current (I_c) for T (oxidation) to form K (reduction) is taken as

$$I_c = nFAD_T \left(\frac{\partial C_T}{\partial x} \right)_{x=0} = nFAD_T \left(\frac{C_T^b - C_T^s}{\delta} \right) \tag{4-7}$$

where n is number of electrons transferred, A is the electrode surface, C_T^s is the concentration of T at surface (x=0), and δ is the thickness of the diffusion layer.

$$\delta = [0.620]^{-1} D_T^{1/3} \nu^{1/6} w^{-1/2} \tag{4-8}$$

For an applied overpotential ($\eta = E_{app} - E^{0'} << 0$), $C_T^s \to 0$ and the value of cathodic current will be limited by the maximum rate of convective-diffusional mass transport, which is well-known Levich equation for fast electron-transfer processes:

$$I_{\lim,c} = 0.620 nFAD_T^{2/3} \nu^{-1/6} w^{1/2} C_T^b \tag{4-9}$$

Eq. 4-9 is for the species with low diffusivity, but for high diffusivity it can be expressed in another form which was described in the reference [154]. However, for the slow electron transfer, the electrode current can be defined:

$$I_c = nFA\kappa_h C_T^s \tag{4-10}$$

where κ_h (cm s^{-1}) is the heterogeneous rate constant for electron transfer.

$$\kappa_h = \kappa_0 \exp\left[\frac{-\alpha F \eta}{RT}\right] \tag{4-11}$$

Combining Eq. 4-7 and Eq. 4-10, I_c can be written as:

$$I_c = \frac{nFAD_T C_T^b}{\delta + D_T / \kappa_h} \tag{4-12}$$

Also, the reciprocal of I_c is given by:

$$\frac{1}{I_c} = \frac{1}{0.62 nFAD_T^{2/3} \nu^{-1/6} w^{1/2} C_T^b} + \frac{1}{nFA\kappa_h C_T^b} \tag{4-13}$$

where Eq. 4-13 is so-called “Koutecky-Levich equation” can be easily abbreviated by the following equation:

$$\frac{1}{I} = \frac{1}{I_k} + \frac{1}{I_{lev}} \tag{4-14}$$

Here, I is the disk current density, I_k is the kinetic current density, and I_{lev} is the Levich current density. The Eq.4-14 is the same as Eq. 4-3.

Figure 4-6a and 4-6b display the ORR polarization curves of the two Au/PtCu catalysts at different rotation speeds in 0.1M O_2-saturated $HClO_4$ at room temperature. Figure 4-6c shows the well-known Koutecky-Levich plots [125], from the ORR polarization curves at 0.6V and 0.8V according to Eq. 4-9. The Levich current density is described by

$$I_{lev} = B \times w^{1/2} \tag{4-15}$$

$$B = 0.62 \times n \times F \times A \times D^{2/3} \times V^{-1/6} \times C_{O_2} \tag{4-16}$$

where w is the rotation rate, n is the overall electron transfer number, F is Faraday constant (96485 C mol^{-1}), A is the geometric-area of electrode (0.19635 cm^2), D is the oxygen diffusivity (1.93×10^{-5} cm^2 s^{-1}), V is the kinetic viscosity of the electrolyte (1.009×10^{-2} cm^2s^{-1}), and C_{O_2} is the oxygen solubility (1.26×10^{-3} mol L^{-1}). Koutecky-Levich plot is derived from the equations between the inverse of disk current and inverse of the square rotation speed (w). Here, the calculated slopes for the Au/PtCu catalysts in Figure 4-6c are closed to 12.5 (mA^{-1} $rpm^{1/2}$), indicating the total electron transfer number is around 4 as described elsewhere.

Table 4-1 shows the kinetic current and total number of electrons transferred in ORR calculated from Figure 4-6c. The results indicate that the n value of Au/PtCu catalysts at 0.6V and 0.8V varies from 3.63 to 4.31, implying the O_2 is majorly reduced to H_2O via the four electron pathway. The case with n>4 may result from variations in oxygen solubility, diffusion-limited current, the choice of trendline of the data points.

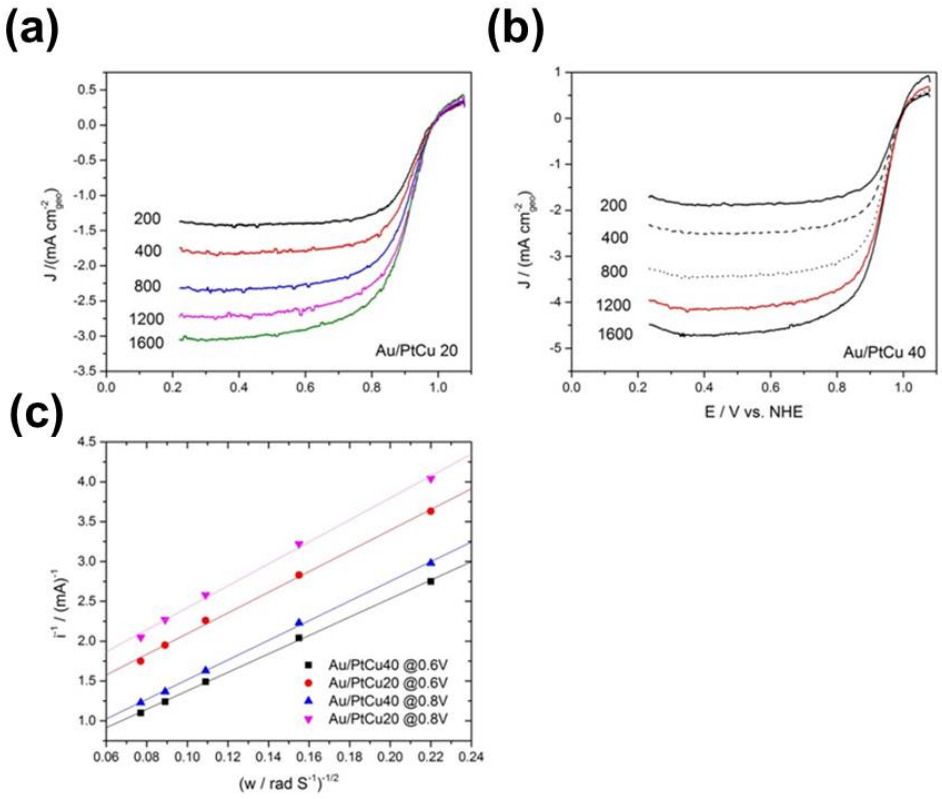

Figure 4-6 (a) ORR curves of the Au/PtCu 20 sample, (b) ORR curves of Au/PtCu40 sample, and (c) Koutecky-Levich plots of the oxygen reduction calculated from (a) and (b) at 0.6V and 0.8V, respectively. The tests were carried out in 0.1M $HClO_4$ solution with 20 mV/s scan rate.

Table 4-1 Kinetic current and electrons transferred numbers of Au/PtCu nanoparticles in ORR.

Sample	E_i (V) vs. NHE	i_k (mA)	n
Au/PtCu 20	0.6	1.26	3.86
Au/PtCu 20	0.8	0.96	3.63
Au/PtCu 40	0.6	4.56	4.31
Au/Pt Cu40	0.8	3.53	4.1

4.4.4 Durability Test of Au/PtCu Nanoparticles

For the fuel cell applications, it is crucial for the catalysts to exhibit long-term durability under working load cycles in the corrosive environment; therefore the AST is employed for probing catalytic durability. In this study, cyclic potential in the range of 0.6V (5sec) and 0.95V (5sec) was employed. Figure 4-7 records the AST results of Au/PtCu, Pt/C and Pt black nanoparticles. The Y-axis represents the relative ECSA value (%) recorded for every 7000 cycles. It is worth noting that the Au/PtCu 20 sample only loses 1% of its initial ECSA. After the first 7000 cycles and less than 5% after 14000 cycles, indicating its superb durability due to the unique core-shell structure and electronic coupling between Au and PtCu. The Au/PtCu 40 nanoparticles appear to display a larger ECSA loss (~ 25%) since a higher Cu content (>30%) may cause the catalysts to be easily corroded in the acid electrolyte during the potential cycles. When compared to the commercial Pt/C, the Au/PtCu 40 still show better catalytic durability with an average 7% less in ECSA loss.

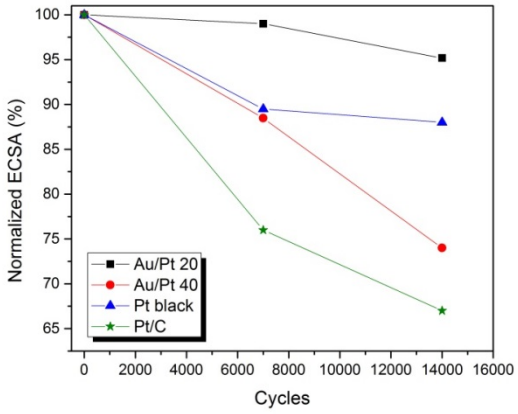

Figure 4-7 Durability of Au/PtCu, Pt black and Pt/C catalysts.

4.4.5 CO-stripping

It is well known that the catalytic behavior of Pt nanoparticles critically depends on the electronic properties. The possible electronic coupling between the PtCu-shell and Au-core is probed by CO-stripping CV. The purpose of using CO-stripping CV is to probe the variation of d-band center caused by electronic coupling between Au and Pt, by investigating the CO-stripping peak shift and the catalytic activity toward the absorbed CO. Here, CO-stripping method is carried out by holding at 0.2V for 15 minutes to absorb CO and then the adsorbed CO was removed by electrochemical CV under Ar purge. The first three curves of the CO-stripping CV scans are shown in Figure 4-8.The Pt/C shows the highest CO oxidation peak (0.86V) which indicates strong CO adsorption to the Pt surface. The Au/PtCu20 nanoparticles exhibit the lowest CO-stripping peak potential (0.726V) than the Pt black (0.731V) and effectively remove CO after the first scan due to the unique electron coupling between the Pt shell and Au core. The Au/PtCu40 nanoparticles show larger peak potential (0.75V), it may be caused by the conjugated PtCu and pure Pt on the Au surface and aggregated Pt as well. In normal fuel cell operation, the lower CO-stripping peak potential may translate to a lower level Pt-OH coverage on the Pt surface, thus enhance the ORR.

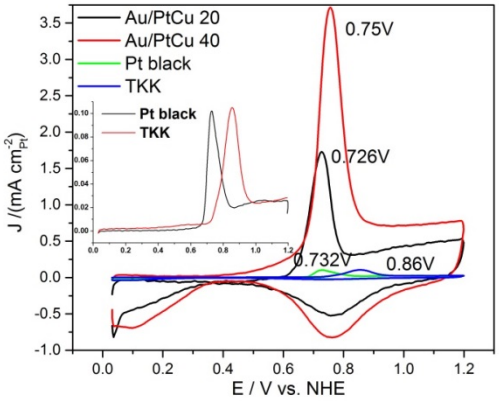

Figure 4-8 CO-stripping CV of four catalysts showing the first scan (from 0.03 V to 1.2 V).

Chapter 5

Au/Pd Nanoparticles with Varied Hollow Au Cores for Formic Acid Oxidation

5.1 Introduction

In this chapter, the effects of Au core toward catalytic behavior of the Pd layer have been discussed. Here the Au electrolyte concentration has been varied and additive Na_2SO_3 has been added to the solution. The purpose of these changes aims to control the different morphology, roughness, porosity and size of the hollow Au cores and probes their impacts on the catalytic properties. From the previous result [55], it was reported that rougher Au surfaces were formed by adding Na_2SO_3 solution in the Au electrolyte. Also, the smaller and porous Au nanoparticles were formed using solutions of lower Au concentrations. Since the outer Pd layer will be affected by the inner Au core through geometric and electronic effects, the FAO activity, stability and long-term durability will also be assessed to understand the core-shell interaction.

5.2 Effect of Concentration of Au Solution

We demonstrated that by decreasing concentration of the Au solution, smaller Au grains and highly porous structures of the hollow Au cores were formed. To adjust the concentration of the Au solution, a buffer solution, containing sodium sulfite (10%), ethylenediamine (5%), and distilled water (85%), was chosen to dilute the Au solution and keep the Au-complex ($Na_3Au(SO_3)_2$) stable. In this study, we prepared three different hollow Au nanospheres denoted as Au100, Au50, and Au25, in which the number stands for the percentage of the Au concentration relative to the received Au solution (7.775 g L^{-1} from Technic).

After that, the various shapes of Au nanoparticles were coated by Cu layers for 10 minutes and then Pd. The results indicated that these Au/Pd catalysts (denoted Au100Pd, Au50Pd, and Au25Pd) show superior catalytic activities as ideal catalysts for formic acid oxidation. Furthermore, these Au/Pd catalysts show excellent electrochemical

stability, CO oxidation ability and long-term durability. Particularly, the Au25Pd nanoparticles synthesized in this study present the best catalytic properties due to their unique structure. The hollow and porous gold cores tuned by reduced Au concentrations in the core/shell structures may influence Pd distribution and morphologies on the Au core.

5.2.1 Physical Characterization

5.2.1.1 XRD

Figure 5-1 shows the XRD reflection peaks of the Pd black at 40.20°, 46.73°, 68.21°and 82.17°, respectively, corresponding to Pd (111), (200), (220) and (311) planes in the fcc structure (JCPDS # 87-0639; 40.21°, 46.78°, 68.3°and 82.34°). For the Au/Pd NPs, the peaks at 38.28°, 44.42°, 64.76°, 77.81° correspond respectively to Au (111), (200), (220) and (311) planes (JCPDS # 65-2870; 38.19°, 44.38°, 64.57°, 77.56°). The very weak Pd signal in the XRD pattern is attributed to the highly dispersed Pd nanocrystallites embedded at the Au surface (shown in TEM images in Figure 5-3).

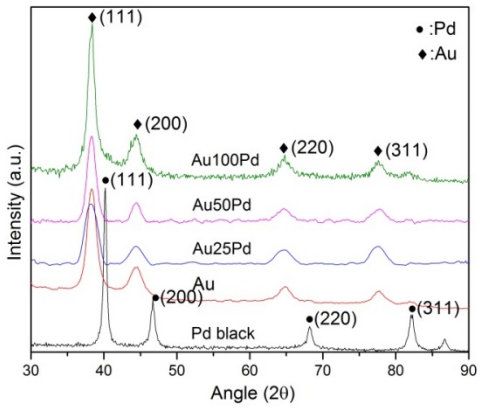

Figure 5-1 X-ray diffraction patterns for the Au/Pd, Au, Pd black nanoparticles.

5.2.1.2 XPS

Figure 5-2 displays the Pd 3d core-level XPS spectra of the Au/Pd nanoparticles and the Pd black. The Au25Pd nanoparticles showing lower Pd $3d_{5/2}$ binding energy (334.9 eV) might demonstrate higher activity than other Au/Pd nanoparticles (Au50Pd: 335 eV; Au100Pd 335.1 eV) and the Pd black (335.4 eV), which will be confirmed in section 5.2.2.

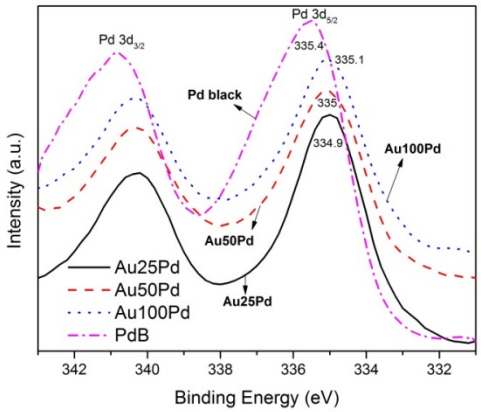

Figure 5-2 Pd 3d XPS spectra measured of the Au/Pd catalysts and Pd black.

5.2.1.3 TEM

Figure 5-3 shows the images of both the hollow Au and Au/Pd core-shell nanoparticles synthesized using different concentrations of Au solutions. The obvious dark/white contrast identified in the images of the Au nanospheres indicates that they are porous. Figures 5-3a and 5-3b show the TEM images of the Au25 and the corresponding Au/Pd nanoparticles (i.e., Au25Pd), respectively. The images clearly display porous Au structures (identified by contrast of TEM images) with 100 nm in diameter and the Pd shells with a thickness of 5-10 nm. The inset in Figure 5-3b shows the HR-TEM image of the Pd outer shell which indicates crystalline nature with a d-spacing of 0.216 nm (refer to JCPDS # 87-0639, d=0.224 nm). Figures 5-3c and 5-3d, showing the TEM images of the

Au50 and Au50Pd, indicate that their sizes are around 115 and 130nm in diameter, respectively. In addition, Figures 5-3e and 5-3f show the Au100 with 126 nm in diameter and Au100Pd with 145 nm in diameter. The comparison of these TEM images indicates the Au25 has the smallest particle size and most porous structure than others. With increasing Au concentration, the porosity of the Au nanospheres decreases, but the size continuously grows almost linearly due to the increased Au solution concentrations.

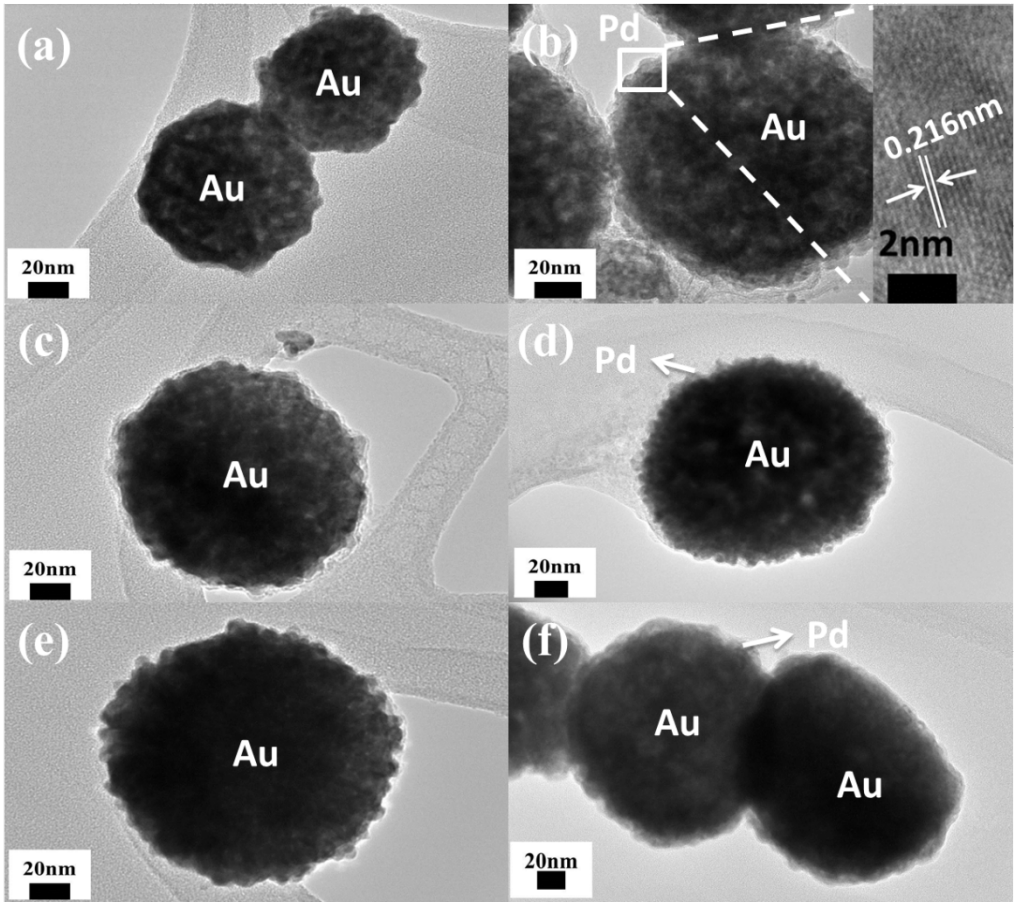

Figure 5-3 TEM images of (a) the Au25, (b) Au25Pd with the inset showing the Pd nanocrystallites from the Pd shell, (c) Au50, (d) Au50Pd, (e) Au100, and (f) Au100Pd.

5.2.1.4 UV-Vis

Ultraviolet–visible spectroscopy (UV-Vis) studies were performed to probe the surface coverage of Pd on the nanoparticles. Figure 5-4 shows the absorption spectra of the Au and Au/Pd NPs, and indicates that the absorption peak increases from 616 nm (Au25) to 698 nm (Au50, Au100) due to the surface plasmon resonance (SPR) effect of Au. The Au/Pd nanoparticles also reveal absorption peaks around 700 nm with the Au100Pd being more pronounced, indicating the Pd shell doesn't fully cover on the Au core surface. This observation is in agreement with the studies carried out by of Shim et. al.[157] because Pd doesn't show any absorption peak within the wavelength studied.

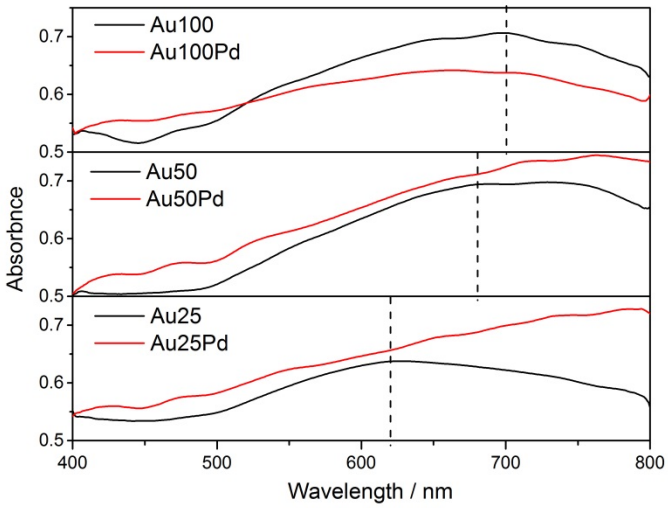

Figure 5-4 UV-vis absorption spectra of different Au and Au/Pd nanoparticles.

5.2.2 Electrochemical Properties

5.2.2.1 CV

In the CV curves shown in Figure 5-5, the current density (J) has been normalized to the electrochemical surface area (ECSA). In the anodic scan direction, the Au50Pd nanoparticles shows slightly higher Pd oxidation peak current than those of other

catalysts even though the onset of Pd oxidation is postponed. Consequently, reduction of the PdO or PdOH formed during the anodic scan occurs at slightly higher potential during the subsequent cathodic scan. The above-observed results might be due to the electronic interaction between Pd and Au and the geometric effect (or so-called ensemble effect). For many surface reactions, a certain number of active sites are required. Ensemble of active sites on the catalyst surface impacts reaction selectivity and activity. The XPS results have already demonstrated that electronic interaction between Pd and Au may not be significant to yield such different adsorption behavior of oxygen-containing species on the Au/Pd nanoparticles. Therefore, we simply attribute the effect of different Au cores in the Au/Pd nanoparticles to the geometric contribution.

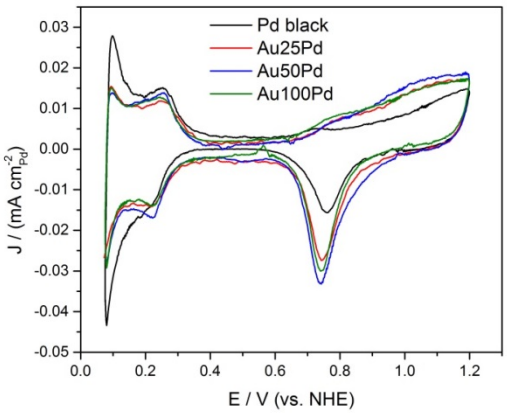

Figure 5-5 CV curves of the Au/Pd and Pd black nanoparticles in 0.1 M $HClO_4$ solution from 0.075 V to 1.2 V. The currents are normalized to the ECSA of Pd.

5.2.2.2 CO-stripping CV

This geometric effect is further confirmed and demonstrated by the CO-stripping results in Figure 5-6. The CO coverage (Au25Pd=0.88; Au50Pd=0.94; Au100Pd=0.9; Pd black=0.78) was calculated based on the integrated area under the oxidation peaks. The Au25Pd displays the lowest CO oxidation potential at 0.87 V compared to the Pd black

(0.92 V), Au50Pd (0.90 V) and Au100Pd (0.91 V). The availability of higher coordinated Pd sites (the most stable configuration) might be slightly reduced for smaller particle size due to the ensemble effect. Therefore, the adsorption strength of CO may be reduced as manifested by a negatively shifted peak potential for the Au25Pd.

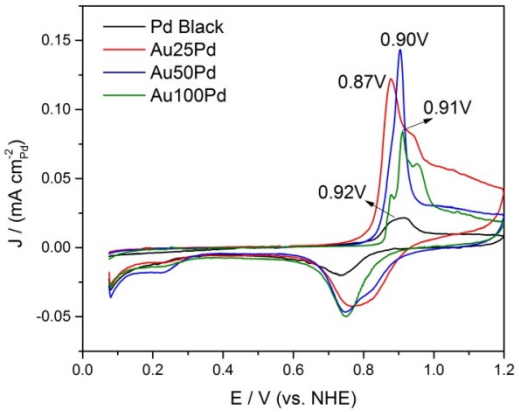

Figure 5-6 CO-stripping CV curves of the Au/Pd and Pd black nanoparticles in 0.1M $HClO_4$ solution from 0.075 V to 1.2 V. The currents are normalized to the ECSA of Pd.

5.2.2.3 FAO CV

The facile oxidation of CO on the core-shell nanoparticles at lower potential will translate to an enhanced FAO kinetics since CO or CO-like species may impede the activities of catalysts. Figure 5-7 shows that the Au25Pd demonstrates the highest area-specific current density (5.5 mA cm^{-2}) in the forward scan direction while the Pd black only shows a peak current of 3.5 mA cm^{-2}. Besides, the specific activity of the Au25Pd at 0.3 V (the normal working potential in a DFAFC) is slightly higher (0.93 mA cm^{-2}) than that of the Pd black (0.85 mA cm^{-2}). In addition, the Au25Pd shows the highest peak potential (~ 0.9 V) in both the anodic and cathodic scans, indicating that significant oxygen-containing species (e.g., hydroxyl) only form at higher potential and therefore the

Au/Pd catalysts could maintain active over a wider potential window without being poisoned by hydroxyl groups.

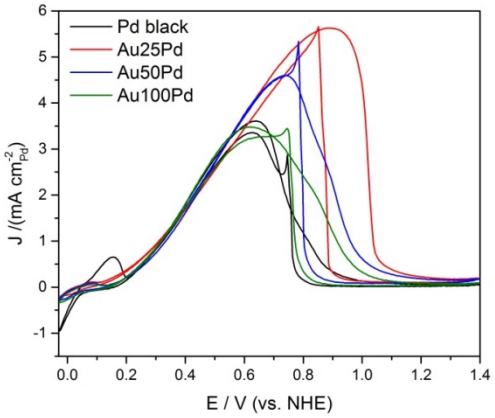

Figure 5-7 FAO CV of the Au/Pd and Pd black catalysts in 0.1 M $HClO_4$ and 0.1 M HCOOH solution from -0.03 V to 1.4 V and rotated at 1000 rpm. The area-specific current densities of the Au25Pd, Au50Pd, Au100Pd and Pd black are normalized to the ECSA.

5.2.2.4 Stability Test

Operation stability of catalysts was evaluated by the chronoamperometry tests in Figure 5-8. The Au25Pd and Au50Pd show the highest area-specific current density (normalized to the ECSA of Pd) initially and are able to maintain their superior stability even after 1 hour at ca. 0.144 mA cm^{-2} which is significantly higher than that of the Pd black (0.0099 mA cm^{-2}).

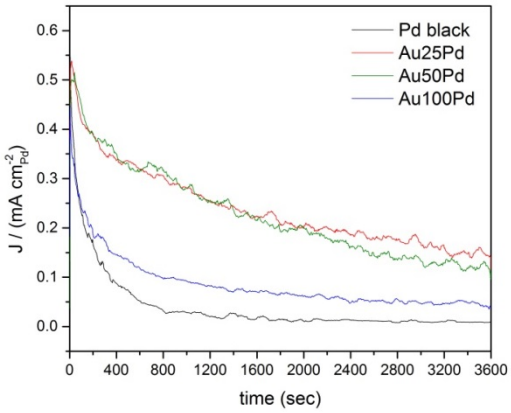

Figure 5-8 Chronoamperometry curves of the Au/Pd and Pd black nanoparticles in 0.1 M $HClO_4$ and 0.1 M HCOOH solution at 0.3 V up to 3600 seconds.

5.2.2.5 Durability Test

Durability of the Au/Pd nanoparticles was evaluated under the AST protocol with potentials applied between 0.6 V (5 sec) and 0.95 V (5 sec) up to 14000 cycles. Figure 5-9 shows that the Au25Pd preserves almost 90% of its initial ECSA in the first 7000 cycles and 71% after 14 k cycles; however, the ECSA loss for the Pd black is 35% in the first 7 k cycles and 62% after 14 k cycles. Not only the Au25Pd but also other Au/Pd catalysts demonstrate better electrochemical durability in the long-term AST. It is well known that dissolution of Pd in acidic electrolytes starts from formation of PdO or PdOH. As Figure 5-5 shows, the Au25Pd can depress the adsorption of oxygen-containing species within the potential window during the cycling tests; therefore, ensemble effect originated from the unique morphologies of the Au core in the Au25Pd may contribute to its superior durability.

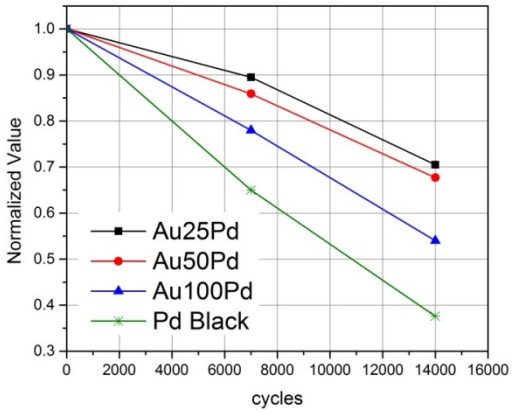

Figure 5-9 Relative ECSA losses for the Au/Pd and Pd black nanoparticles in 0.1 M $HClO_4$ solution during potential-cycling tests.

5.3 Effect of Na_2SO_3 in Au Solution

In order to tune the surface roughness of the hollow Au spheres according to our previous study [55], 1 ml Na_2SO_3 solution was added into 4 ml Au solution (7.775 g L^{-1}, Technic Inc.) at concentrations of 2 M, 0.2 M and 0 M (i.e. deionized water only) to form $[Au(SO_3)_2]^{3-}$ complexants. After leaving for 12 hours, the final pH values of the mixed solution were 6.75, 6.3, and 6, for 2 M, 0.2 M, and 0 M, respectively. In this study, different Au/Pd nanoparticles were labeled as 2 M, 0.2 M and 0 M accordingly. The higher concentration of Na_2SO_3 in the Au solution generated rougher Au surface; however, the defects of the Pd layer on the Au/Pd core-shell structure are expected to increase accordingly. These defects may retard the electrochemical reaction of FAO on the catalysts. From the electrochemical results, our Au/Pd core-shell nanoparticles show superior catalytic activities for FAO, stability, CO oxidation ability and long-term durability than the Pd black. Particularly, the 0M-Au/Pd nanoparticles synthesized in this study present the best catalytic properties probably due to fewer defects in the Pd layer. In

order to further understand the experimental results, we developed a simple model, which aims to provide insights to the FAO reaction mechanism.

5.3.1 Physical Characterization

5.3.1.1 XRD

XRD patterns of commercial Pd black in Figure 5-10 also show Pd (111), (200), (220) and (311) planes at 40.20°, 46.73°, 68.21° and 82.17°, respectively. For the three Au/Pd nanoparticles obtained using different Na_2SO_3 concentration indicated in the figure, the peaks at 38.44°, 44.45°, 64.88°, 77.71°, 81.88° correspond respectively to Au (111), (200), (220), (311), and (222) planes (JCPDS No. 04-0784; 38.18°, 44.39°, 64.57°, 77.54°, 81.72°). Because of highly dispersed Pd nanocrystallites embedded at the Au surface (will be shown in TEM images in Figure 5-13), the Au/Pd nanoparticles display very weak Pd signal in Figure 5-10. In addition, there is no identifiable Cu signal in the spectra, suggesting that Cu has been completely replaced by the Pd shell.

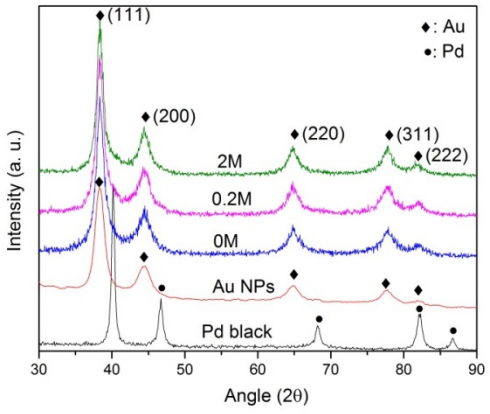

Figure 5-10 XRD pattern of Au/Pd NPs and Pd black

5.3.1.2 XPS

Figure 5-11 shows the Pd 3d core-level XPS spectra of the Au/Pd nanoparticles and Pd black. From XPS result, not only the electronic configuration of Pd was probed, but also the presence of nanocrystalline Pd can be confirmed. The Au/Pd nanoparticles of 0 M, 0.2 M, and 2M show lower Pd $3d_{5/2}$ binding energy at 334.9 eV, 334.9 eV, and 335.4 eV, respectively, than the Pd black (335.5 eV). The impact of the core-level binding energy on electrochemical FAO will be examined later.

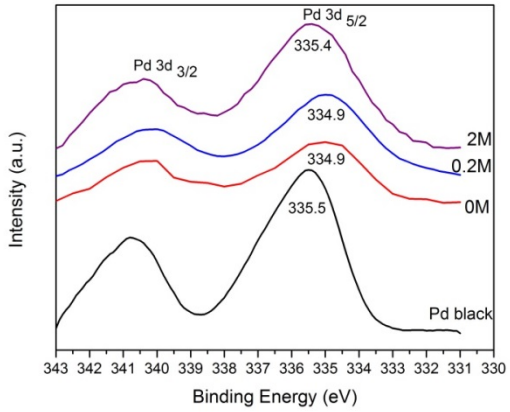

Figure 5-11 Pd 3d XPS spectra of three Au/Pd nanoparticles and the Pd black

5.3.1.3 SEM

Figure 5-12 shows the FE-SEM images of the three types of hollow Au nanospheres. The average particle size in diameter is about 120 nm for 0 M, 100 nm for 0.2 M and 90 nm for 2 M. It is found that the surface roughness of the three Au nanoparticles ranks in the order of 2 M > 0.2 M > 0 M, indicating that $[SO_3]^{2-}$ plays an important role to stabilize Au ions in the solution and alter the hollow Au morphologies. Our previous study has discovered that the size and roughness of the Au nanoparticles critically depend on the Au ions in various $[Au(SO3)_2]^{3-}$ complexants and smoother

surface of Au nanoparticles could be achieved by adding lower concentration of Na_2SO_3 solution.

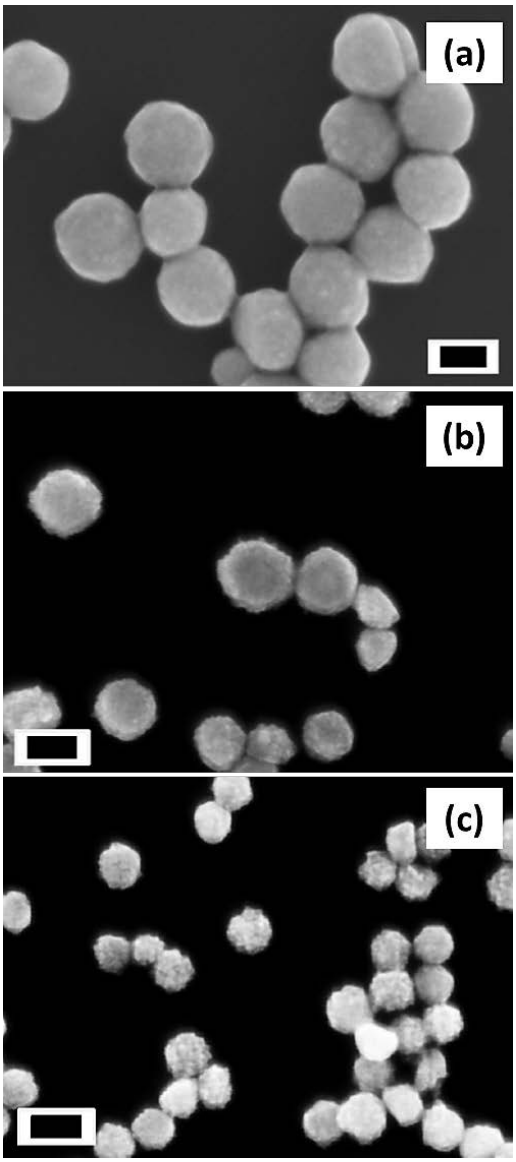

Figure 5-12 FE-SEM images of different Au nanoparticles (a) 0 M, (b) 0.2 M, and (c) 2 M The scale is 100nm.

5.3.1.4 TEM

The microstructures of the hollow Au/Pd nanoparticles synthesized in different Na_2SO_3 concentrations were investigated by HR-TEM in Figure 5-13. The image of

Figure 5-13a clearly displays a continuous 10nm-thick Pd shell and the average size of Au/Pd nanoparticles is around 130 nm in diameter. In addition, the TEM images of the 0.2 M and 2 M Au/Pd nanoparticles in Figures 5-13b and 5-13c, respectively, indicate that their sizes are around 115 and 120 nm in diameter. The island-like Pd shells of the 0.2 M and 2 M Au/Pd nanoparticles show observably higher roughness than 0 M-Au/Pd nanoparticles. With increasing Na_2SO_3 concentration in the Au solution, the roughness of the Au nanospheres increases, and thus impedes continuous Pd growth on the surface of Au.

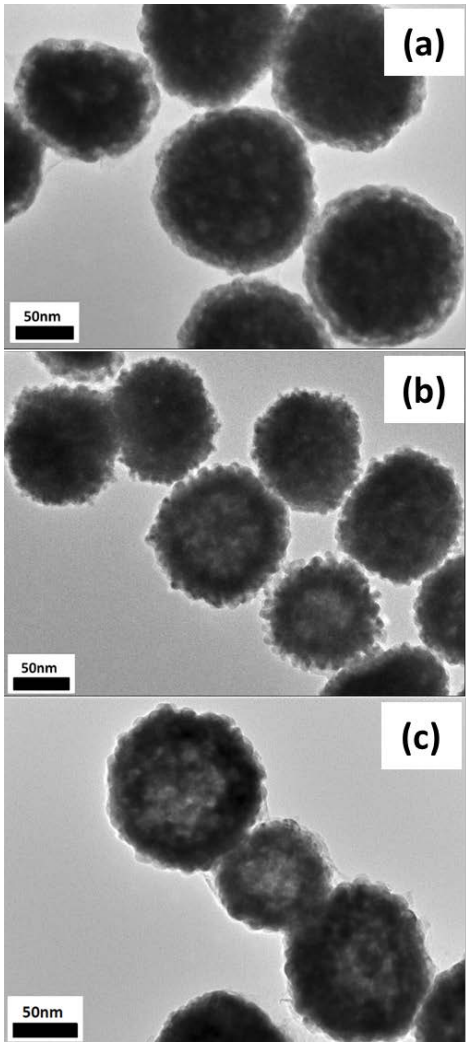

Figure 5-13 HR-TEM images of different Au/Pd NPs (a) 0M; (b) 0.2M and (c) 2M

5.3.2 Electrochemical Properties

5.3.2.1 CO-stripping CV

Electrochemical characteristics of the Au/Pd nanoparticles and the Pd black were evaluated in Figure 5.14-17.The calculated ECSA is individually listed: 2 M: 6.61 $m^2 g^{-1}$, 0.2 M: 6.54 $m^2 g^{-1}$, 0 M: 4.5 $m^2 g^{-1}$ and Pd black: 6.3 $m^2 g^{-1}$. The CO-stripping results in Figure 5a show that the 0 M-Au/Pd nanoparticles display the lowest CO oxidation peak potential at 0.82 V compared to the Pd black (0.95 V), 0.2 M (0.91 V) and 2 M (0.90 V) Au/Pd nanoparticles. Besides, the Au/Pd nanoparticles display lower onset potential for CO oxidation with the 0M sample being almost 0.2 V lower than that of the Pd black, indicating the strongest CO oxidation ability and electronic coupling between the Au core and Pd shell. On the other hand, the availability of higher coordination Pd sites (the most stable configuration) might be slightly reduced for smaller Pd particles (Au/Pd nanoparticles~ 6-10 nm; Pd black~15 nm). Since the CO-stripping is a structure sensitive technique, the broadening of CO-stripping peak of the Au/Pd nanoparticles may result from different bonds of CO to the catalysts such as linear, bridge and others.

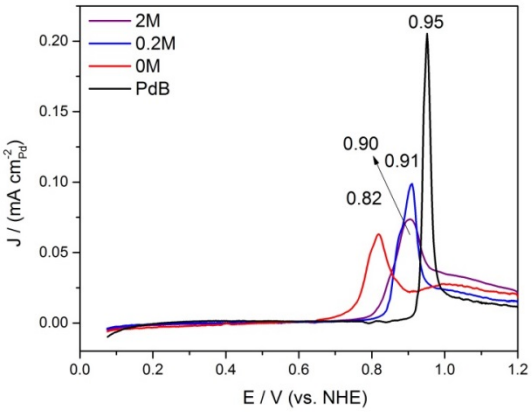

Figure 5-14 CO-stripping CV of Pd catalysts in $HClO_4$ solution

5.3.2.2 FAO CV

It is well known that CO or CO-like intermediates may retard the activities of catalysts and the FAO kinetics strongly depend on oxidation of these intermediates on the core-shell NPs at lower potential. Figure 5-15 shows that the 0M-Au/Pd nanoparticles demonstrate the highest area-specific current density (6.5 mA cm^{-2}) in the forward scan direction while the Pd black only shows a peak current of 1.93 mA cm^{-2}. The specific activity (1.01 mA cm^{-2}) of the 0 M-Au/Pd nanoparticles measured at 0.3 V (the normal working potential in a DFAFC) almost doubles that of the Pd black (0.51 mA cm^{-2}). In addition, the 0 M-Au/Pd nanoparticles showed the highest peak potential (0.736 V) in both the anodic and cathodic scans. Since the catalytic oxidation is highly structure-sensitive, the defects and steps in the Pd shell, caused by rougher Au core, are easy to adsorb anions and prone to be poisoned, thus inhibiting the FAO reaction. Moreover, the electronic interaction between Au support and Pd catalyst may influence the catalytic activity. The XPS result of 2M Au/Pd nanoparticles in Figure 5-11 demonstrated a positive shift of the binding energy (broad peak, 335.7-335.1 eV), suggesting a lower FAO activity according to the references. This may explain why the 2M Au/Pd nanoparticles show lower catalytic activity than other Au/Pd nanoparticles and thePd black.

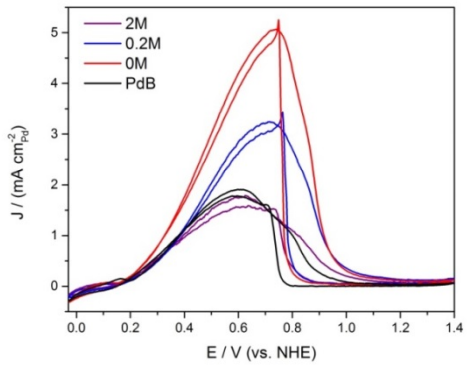

Figure 5-15 FAO CVs of Au/Pd and Pd black in 0.1 M of $HClO_4$ and HCOOH solution

5.3.2.3 Stability Test

The FAO stability of the Au/Pd nanoparticles and the Pd black was studied by the chronoamperometry tests in Figure 5-16. The 0 M-Au/Pd nanoparticles show the highest area-specific current density initially and is able to maintain its superior performance even after 1 hour at 0.064 mA cm^{-2} which is obviously higher than those of the Pd black (0.008 mA cm^{-2}) and other Au/Pd nanoparticles.

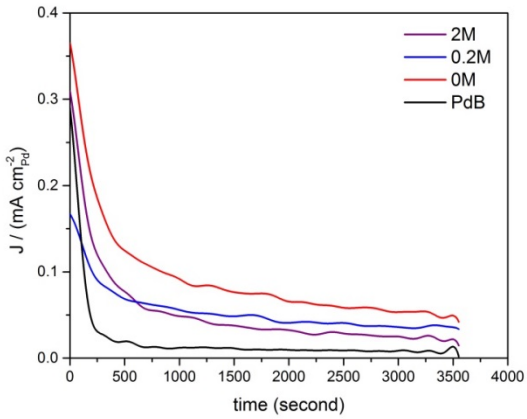

Figure 5-16 Chronoamperometry curves in 0.1 M of $HClO_4$ and HCOOH solution at 0.3 V up to 3600 sec

5.3.2.4 Durability Test

Durability of the Au/Pd nanoparticles was evaluated under the AST protocol with potentials applied between 0.6 V (5 sec) and 0.95 V (5 sec) up to 14,000 cycles. Figure 5-17 shows that the 0M-Au/Pd nanoparticles preserves almost 84 % of its initial ECSA in the first 7,000 cycles and 60 % after 14,000 cycles; however, the ECSA loss for the Pd black is 35 % in the first 7,000 cycles and 62.4 % after 14,000 cycles. The 0.2 M and 2M -Au/Pd nanoparticles also demonstrate better electrochemical durability in the long-term AST than the Pd black. Generally, in terms of most favorable particle size of Pd nanoparticles for FAO, an intermediate range between 5-7 nm is most active as reported

by Zhou et al.[142]. In this study, we believe that the Pd grains in the shell of different samples remain within that favorable range (as confirmed by HRTEM images). Under constant Pd particle size, changes in Pd surface structure and electronic effects, both induced by roughness of the Au core, play a key role in both catalytic activity and durability. It is well known that during long-term tests in an acid environment, PdO and PdOH species will be generated leading to a decrease of efficiency and possible corrosion of the Pd catalysts. The 0 M-Au/Pd nanoparticles express higher stability and durability which may be due to fewer defects on Pd layers and lower Pd 3d core-level binding energy; therefore, both geometric and electronic effects originated from the smooth Au core in the 0 M-Au/Pd nanoparticles may contribute to its superior durability.

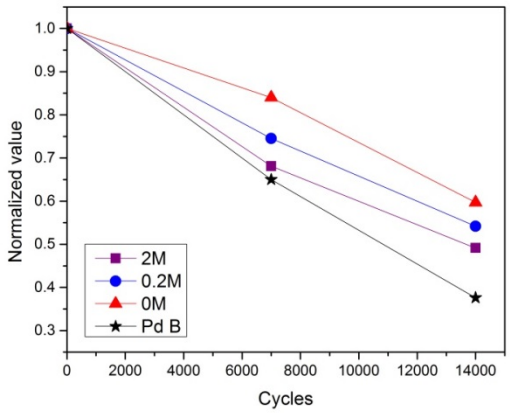

Figure 5-17 Normalized ECSA of Pd catalysts after 7k and 14k cycles of AST.

Chapter 6

In Situ Raman of CO Oxidation, Experiment and Simulation of the Electrooxidation of Formate-based Solutionson Au/Pd Nanoparticles

6.1 Introduction

In order to further investigate the catalytic ability of the Au/Pd nanoparticles, in situ Raman spectroscopy was employed as a convenient tool to survey CO-stripping ability. Since formate is considered as one of the possible intermediates during the formic acid oxidation, in the second part of this chapter, we will discuss the influence of formate group in the electro-oxidation. By using formate-based solutions as the electro-oxidation study on Au/Pd catalysts, we can have a comprehensive understanding of the impact of formate group.

To understand the electro-oxidation mechanism of formate-based solutions and shed light on the fundamental difference between Au/Pd nanoparticles and the Pd black, numerical simulation is adopted in this study. A simple simulation was developed to predict the anodic curve by including reaction intermediates of formate and hydroxyl groups [108, 158]. In this part of simulation, the impact of roughness (Chapter 5-3), Pd thickness, and formate-based solutions on Au/Pd nanoparticles will be discussed in different cases.

6.2 In Situ Raman Scattering of CO Oxidation

6.2.1 Experimental Setup

In situ Raman spectroscopy was conducted on a DXR Raman microscope (Thermo Scientific) using a 780 nm laser at 30 mW as the light source and associated with a homemade three-electrode electrochemical system (potentiostat: Princeton Applied Research 2273) - a Au/Cr coated Si wafer, a Pt wire, and a Ag/AgCl electrode as the working, counter, and reference electrodes shown in Figure 6-1a, respectively. The scan range is from -0.3V~0.6V (vs. Ag/AgCl) at the scan rate of 10 mV/s. Saturated CO

solution was prepared by bubbling of CO gas in 0.1M $HClO_4$ solution for one hour before the test.The catalysts were dropped on the Au/Cr coated Si wafer and dried under the IR lamp for 10 minutes. The SEM image of Au/Pd nanoparticles on the working electrode was shown in Figure 6-1b and the TEM images show the detailed microstructures in Figure 6-1c.Herein we conducted in situ Raman studies on our core-shell nanoparticles to understand their structures and understand their formate oxidation activity. However, a thick Pd shell may hinder the surface plasmon resonance (SPR) of the inner Au cores under laser. Hence, UV-Vis spectroscopy was employed to examine the SPR effect of the nanoparticles. The UV-Vis spectra (scan range: 400~800 nm) shown in Figure 6-1d indicates an absorption peak around 650 nm due to the unique SPR effect from the inner Au core. The contribution from the rough Pd outer layers to the above UV-Vis spectra has been ruled out since the commercial Pd black doesn't show any significant absorption peak, although Pd has been considered as a potential SERS material elsewhere[159].

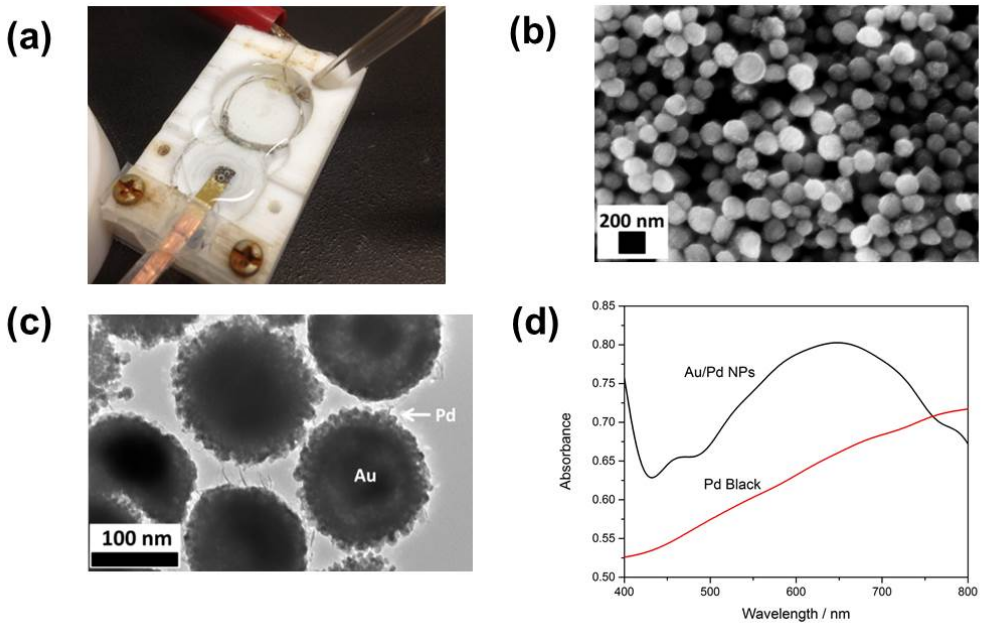

Figure 6-1 (a) Homemade three electrode system for in situ Raman measurement, (b) HR-SEM image of Au/Pd nanoparticles on Si wafer, (c) TEM images of Au/Pd nanoparticles, and (d) UV-Vis absorption spectra.

6.2.2 Results and Discussion

To evaluate the catalytic abilities for removing CO poison species, we borrowed CO as the probe molecule to investigate CO oxidation ability on different catalysts at varying potentials. CO adsorption to the catalysts was first performed at 0.3 V for 5 minutes in a CO-saturated 0.1M $HClO_4$ solution. Then Raman spectra were collected while the potential of the working electrode was maintained at certain potentials. In the potential-dependent Raman spectra in Figure 6-2, the low-frequency band at around 370 cm^{-1}[160]is attributed to the Pd-C vibration of bridge-bonded CO[161]. In addition, the strong band at about 1950 cm^{-1} in the high frequency region is assigned to the stretching mode of bridge-bonded CO. In Figure 6-2a of the Au/Pd nanoparticles, the CO band at about 1950 cm^{-1} appears at -0.2 V and gradually moves to higher wavenumber (blue

shift) until it disappeared at 0.6 V. There should be another band corresponding to linear-bonded (on-top) CO at around 2070 cm^{-1} according to reference [160]. However, because of the strong peak from substrate (noted as an asterisk in all figures) at 2030 cm^{-1}, this weak CO signal may be shielded in this broad area.

The CO band at around 1950 cm^{-1}[160] from the Pd black in Figure 6-2b does not show any observable shift within the entire potential window. The peak emerges at -0.3 V and still shows a noticeable intensity at 0.6 V, indicating that a fraction of the CO still adsorb to the Pd black. These results indicate that the Au/Pd nanoparticles show a stronger CO oxidation ability. On the other hand, comparison of the high-frequency peak at ca. 1950 cm^{-1} may also suggest difference in surface structure of the two Pd samples. It has been reported that the C-O stretching frequency reduces when adsorbed on three-fold-hollow Pd sites (1844 cm^{-1}) than adsorbed on bridge-bonded sites (1950 cm^{-1}). Besides, it was discovered that peaks related to CO adsorption on defect-rich Pd particles (e.g., surface steps and/or particle edges) appear at higher wavenumbers compared to the bridge-bonded CO on (111) terraces[162]. Thus it seems reasonable to attribute the blue shift of the 1950 cm^{-1} band to a change in the preferred adsorption site for the Au/Pd nanoparticles under different potentials – from three-fold-hollow Pd sites to bridge-bonded sites. The absence of this Raman shift for the Pd black sample probably suggests more surface steps and/or edges on the particle which significantly reduce the three-fold-hollow adsorption sites. The different fluctuation of Figure 6-2a and 6-2b in the high frequency region of spectra could be affected by the roughness of the particles and substrate as reported by M.J. Weaver et al. [72] and S.Z. Zou et al. [136]. Besides, similarly low quality of SERS signal on the Pd surface was also reported by Fleischmann M. et al. [163]. We believed that the difference between the Pd black and Au/Pd nanoparticles in higher frequency region is due to their different surface roughness. However, the noise is not significant in the lower frequency region.

(a)

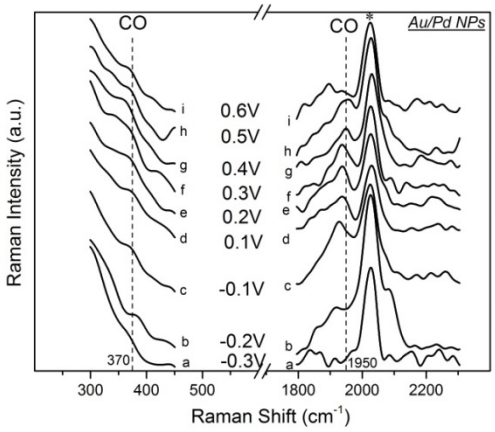

(b)

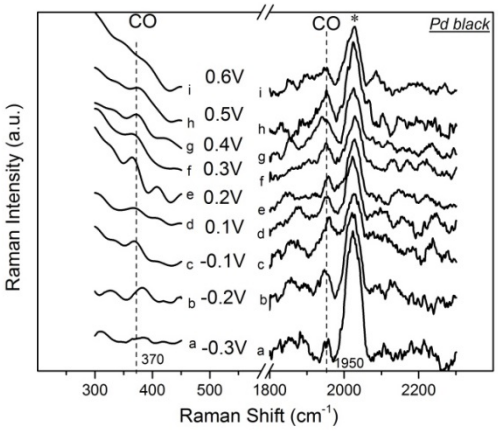

Figure 6-2 Potential-dependent Raman spectra of (a) Au/Pd nanoparticles, and (b) Pd black in 0.1 M $HClO_4$ saturated CO (* indicating the signal from the substrate of Au/Cr-coated Si).

6.3 Electro-oxidation of Formate-based Solutions

Figure 6-3a and 6-4b show that the Au/Pd nanoparticles yield remarkably higher FAO current densities (normalized to the ECSA of Pd) than those of the Pd black at the same FA concentration. The higher activity of the Au/Pd nanoparticles can be clearly

revealed by Table 6-1 which summarizes the current densities at 0.3 V in different solutions. For example, the current densities are 1.12 mA cm^{-2} and 0.63 mA cm^{-2} for the Au/Pd nanoparticles and the Pd black respectively in 1.0 M FA solution, indicating that individual Pd atom at the Au/Pd NP surface is 178% more active than that of the Pd black. It is well known that electrochemical area-specific activity of Pd or Pt particles is inversely proportional to the particle size. This almost doubled area-specific activity of the Au/Pd nanoparticles compared to that of the Pd black is possibly due to the electronic coupling between the core and shell as well as feasibly structural/geometric contributions. The pH values of different solutions are also provided in Table 6-1. Lower pH values seem to enhance the current density in the FA solutions; however, the opposite trend shows up for the SF and mixed (FA + SF) solutions. Besides, the peak position corresponding to the maximum current density in both Figure6-3a and 6-3b shows interesting positive shift with increasing FA concentration, indicating that the surface coverage of adsorbed intermediate species could be altered by FA concentration during FAO reaction.

On the contrary, the oxidation peak potential decreases (negative shift) in SF solutions when the concentration increases as shown in Figure 6-3c and 6-3d. This observation is consistent with the results reported by Gao et al.[164] though Pt catalysts were employed in their studies. In addition, the highest oxidation currents (peak current densities: 9.4 mA cm^{-2} for the core-shell nanoparticles and 7.4 mA cm^{-2} for the Pd black) were achieved using the most concentrated SF solution (1.0 M). Formate has been considered as one of the active species that participate in electrochemical oxidation reaction,

$$HCOO^- \rightarrow CO_2 + H^+ + 2e^- \quad (6\text{-}1)$$

Therefore, a higher concentration of formate improves the oxidation current. On the other hand, more formate groups could adsorb on the Pd surfaces at higher

concentrations and then block these active sites, which may also retard the catalytic reaction especially at high potentials where surface coverage of formate reaches the maximum. With the increase of SF concentration, the negative shift of oxidation peak potentials suggests an earlier saturation of the reaction intermediate species on Pd surface at lower potentials. A summary of the results from Figure 6-3a ~ 6-3d implied that formate group is a highly active species in the oxidation reaction. For example, oxidation of 1.0 M SF by the Au/Pd nanoparticles produces a current density of 2.98 mA cm^{-2} at 0.3 V (Table 6-1), whereas oxidation of 1.0 M FA only yields 1.12 mA cm^{-2}.

Mixed solutions combining SF and FA were also tested. The concentration of SF varied while that of FA was fixed at 0.5 M which has been demonstrated to produce the highest current density according to Figure 6-3a and 3b. Several phenomena are observed from Figure 6-3e and 3f. First, the oxidation peak potentials follow the same trends in SF solutions, i.e., peaks shift negatively with increasing SF concentration. However, the highest peak current density was produced using an intermediate concentration of SF (0.5 M). This is somewhat surprising and contrary to the results in Figure6-3c and 3d. More interestingly, the response of peak potentials to the SF concentration is different for the Au/Pd nanoparticles (more sensitive) and the Pd black (less sensitive) in the mixed solutions. The peak potentials range from 0.8 V to 1.39 V for the former and from 0.89 V to 1.2 V for the latter when different SF concentration was used. Second, the current density at low potentials (e.g., at 0.3 V in the left branch of the volcano curve) increases as the SF concentration from 0.1 M to 1.0 M.

The chronoamperometric tests in Figure 6-4 demonstrate higher stability of Au/Pd nanoparticles than Pd black in the same condition. The applied potential at 0.3V (vs. NHE) is chosen around the operation potential of DFAFCs. Within the promoted solution concentration, the current density indicates distinct increase, suggesting an efficient improvement of their lower energy density (~2104Wh L^{-1}). The worth noticing

thing in Figure 6-4 indicates that the current density of the Au/Pd nanoparticles is almost double than Pd black in all 1.0M formate-based solutions.

Table 6-1 The relation of current density (at 0.3V vs. NHE) with different formatted-based solutions.

N0.	**Formic acid (aq.)**	**Sodium Formate (aq.)**	**pH value**	**I @ 0.3V (mA/cm2)**
A1	0.1 M		1.39	0.61
A2	0.5 M		1.21	0.96
A3	1.0 M		1.14	1.12
A4		0.1 M	2.25	0.69
A5		0.5 M	4.18	1.84
A6		1.0 M	4.61	2.98
A7	0.5M	0.1M	1.9	0.73
A8	0.5M	0.5M	3.26	1.93
A9	0.5M	1.0M	3.68	2.83
B1	0.1 M		1.39	0.4
B2	0.5 M		1.21	0.52
B3	1.0 M		1.14	0.63
B4		0.1 M	2.25	0.32
B5		0.5 M	4.18	0.96
B6		1.0 M	4.61	2.1
B7	0.5M	0.1M	1.9	0.45
B8	0.5M	0.5M	3.26	1.41
B9	0.5M	1.0M	3.68	2.06
A: Au/Pd NPs catalysts ; B: Pd black				

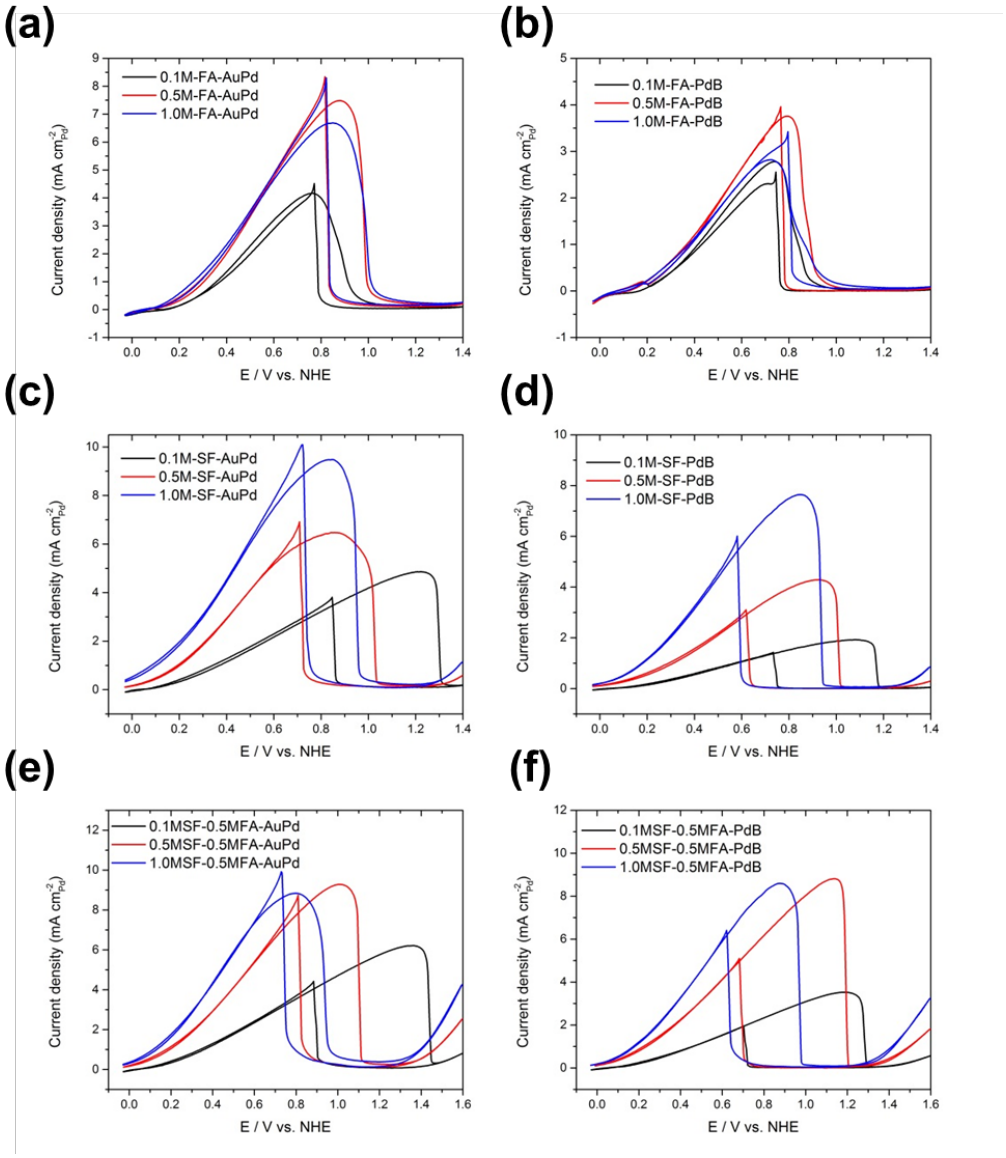

Figure 6-3 Area-specific cyclic voltammograms of (a) Formic acid-Au/Pd catalysts, (b) Formic acid-Pd black, (c) Sodium formate-Au/Pd catalysts, (d) Sodium formate-Pd black, (e) Hybrid solution-Au/Pd catalysts, and (f) Hybrid solution-Pd black in different concentration. The scan rate is 10 mV/sec.

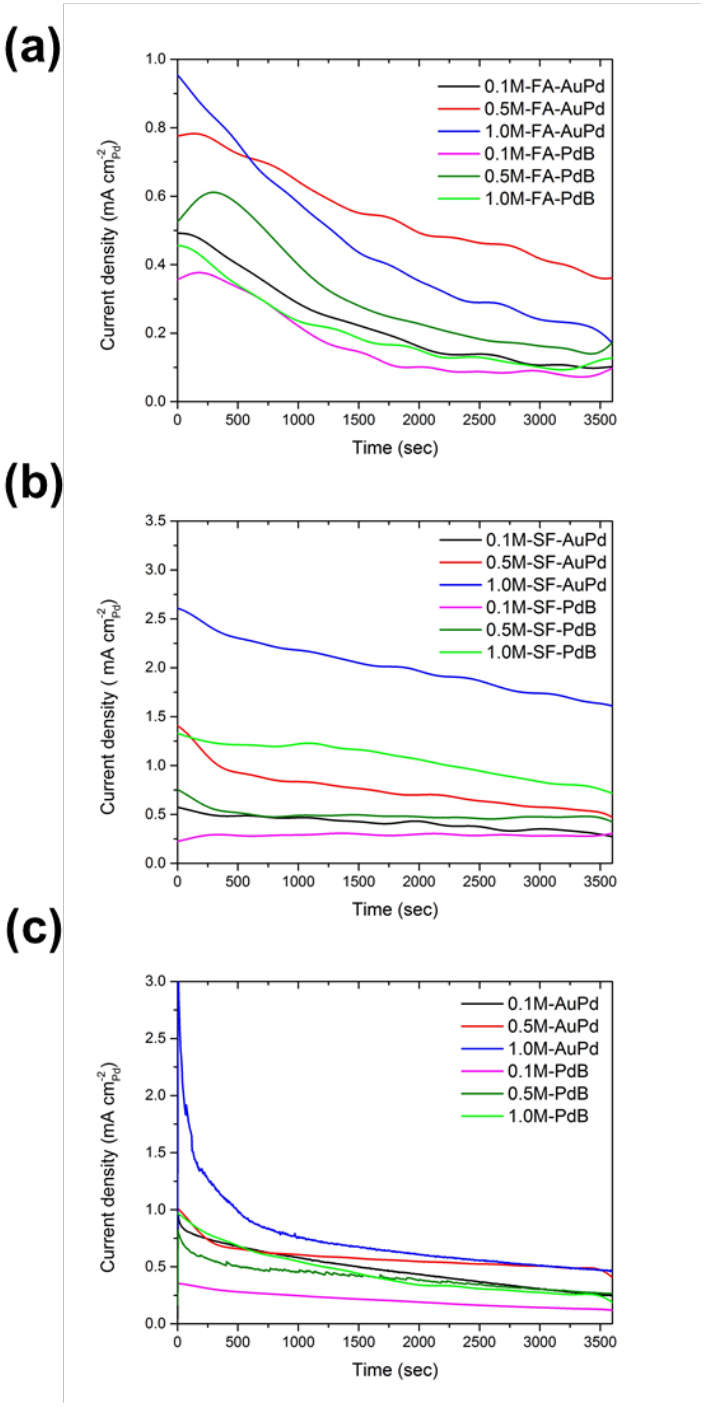

Figure 6-4 Chronoamperometric tests at 0.3V (vs. NHE) for Au/Pd NPs and Pd black catalysts in various concentration of (a) Formic acid, (b) Sodium formate, and (c) Hybrid solution (different concentration of sodium formate in 0.5M formic acid).

6.4 Simulations of Electro-oxidation Curve

6.4.1 Simulation method

In order to study the FAO mechanism, we conducted a simple simulation by merely considering formate and hydroxyl groups as the intermediates, since several reports already proved formate as the reaction intermediate during FAO reaction without generating CO as the poisoning species. Formate molecule was recently confirmed as one of the possible intermediates among others such as OH_{ads}, $COOH_{ads}$, and CHO_{ads}[165, 166] via IR spectra and other techniques. The electro-oxidation of formic acid on Pd-based catalysts is considered as a direct pathway via a dehydrogenation reaction:

$$HCOOH \rightarrow CO_2 + 2H^+ + 2e^- \quad (6\text{-}2)$$

During the reaction, the generated intermediates block the available sites on the catalysts and therefore prevent further reactions.

In this study, the possible reaction steps listed below are considered:

$$Pd + HCOOH \rightarrow Pd + CO_2 + 2H^+ + 2e^- \quad (6\text{-}3)$$

$$H_2O + Pd \leftrightarrow PdOH + H^+ + e^- \quad (6\text{-}4)$$

$$Pd + HCOOH \rightarrow PdHCOO + H^+ + e^- \quad (6\text{-}5)$$

$$PdOH + PdHCOO \rightarrow H_2O + 2Pd + CO_2 \quad (6\text{-}6)$$

These four equations consist of the direct dehydrogenation pathway (6-1) and other intermediate-containing pathways. Here, the coverage of the formate and hydroxyl group was denoted as θ_1 and θ_2, respectively. The corresponding kinetic equations for the above reactions can be expressed as follows:

$$V_1 = k_1 C_f (1 - \theta_1 - \theta_2) \exp(\frac{E}{b_1}) \quad (6\text{-}7)$$

$$V_2 = k_2 C_w (1-\theta_1-\theta_2)\exp(\frac{E}{b_2}) - k_{-2} C_{H^+} \theta_2 \exp(\frac{-E}{b_2}) \quad (6\text{-}8)$$

$$V_3 = k_3 C_f (1-\theta_1-\theta_2)\exp(\frac{E}{b_3}) - k_{-3} C_{H^+} \theta_1 \exp(\frac{-E}{b_3}) \quad (6\text{-}9)$$

$$V_4 = k_4 \theta_1 \theta_2 C_f C_{H^+} \quad (6\text{-}10)$$

where E is the potential (V vs. NHE), C is the concentration (M) with subscripts representing different species (e.g., f: formic acid; w: water), bis the Tafel slope, and *k* is the reaction constant. Table 6-2 lists parameters for the Au/Pd NPs and Pd black. The overall production rates of formate and hydroxyl can be calculated by the following equations:

$$q \cdot \frac{d\theta_1}{dt} = V_3 - V_4 \quad (6\text{-}11)$$

$$q \cdot \frac{d\theta_2}{dt} = V_2 - V_4 \quad (6\text{-}12)$$

in which q is assumed to be the charge of these intermediates absorbed on the Pd surface. Finally, the total current density (J= mA cm^{-2}) can be calculated as:

$$J = 2 \cdot V_1 + V_2 + V_3 \quad (6\text{-}13)$$

When the electro-oxidation simulations for the formate-based solutions, the reaction pathways of sodium formate on Pd-based catalysts, Eq. (6-3) was replaced by Eq. (6-14) for direct formate oxidation and Eq. (6-5) was rewritten into Eq. (6-15) for adsorption of formate on Pd surface, and the other steps are the same as FAO.

$$\mathrm{Pd} + \mathrm{HCOO^-} \rightarrow Pd + \mathrm{CO_2} + \mathrm{H^+} + 2\mathrm{e^-} \quad (6\text{-}14)$$

$$\mathrm{Pd} + \mathrm{HCOONa} \rightarrow PdHCOO + Na^+ + \mathrm{e^-} \quad (6\text{-}15)$$

6.4.2 Results and Discussion

6.4.2.1 Roughness of the Gold Nanoparticles

Figure 6-5a shows the anodic scan of the simulated (dot-line) and experimental curves (solid-line) of the 0M-Au/Pd NPs and Pd black according to Chapter 5-3. It is apparent that the simulation result agrees well with the experimental result, except that at higher potential the curve of the Au/Pd nanoparticles after peak potential drops suddenly probably due to accumulation of intermediates on the reactive surface (blocking-site effect). The corresponding parameters used in the simulation shown in Table 6-2 indicate that the reaction constant k_1 of the Au/Pd nanoparticles is higher than that of Pd black while other reaction constants are unchanged. This suggests that the FAO reaction majorly happens in dehydrogenation pathway, in a good agreement with reports in literature [46, 167] that $HCOOH_{ads}$ forms on Pd surface and carries the most oxidation current.

The kinetics of electrochemical reactions strongly depends on the charge transfer coefficient which is closely related to the electrode material. The charge transfer coefficient (α) [168] is calculated from: $\alpha=2.303\times R\times T/(n\times b\times F)$, where R is the gas constant, T is the absolute temperature, n is the number of electrons, b is the Tafel slope and F is the Faraday constant. The transfer coefficient from the Tafel slope (b_1) of the Au/Pd nanoparticles (0.155) is smaller than that of the Pd black (0.184) with assumption of n=2. Also, the transfer coefficients calculated from b_2 and b_3 (n=1) are smaller for the Au/Pd nanoparticles (α=0.328) than those of the Pd black (α=0.394). In addition, the surface coverage of the formate and hydroxyl groups on the Au/Pd nanoparticles and Pd black in Figure 6-5b and 6-5c show much lower formate coverage than those of hydroxyl group, which agrees with reported results in many studies using infrared technique. For example, Samjesk et al. [63] reported that formate was generated at low potentials and reached to the highest coverage at around 1.0 V similar to Miyake's finding[46] (highest

peak at 0.8 V). However, signal of the formate in many reports shows very low intensity due to its low coverage on the catalyst surface. Chen et al. [169]reported that 15% of FAO current is attributed from oxidation of formate, and the rest may come from reactions in other pathways. The result of the Au/Pd nanoparticlesin Figure 6-5b shows that formate starts forming on the surface of the catalysts at 0.01 V and reaches to a surface coverage of 6.8% at 1.1 V; however, the hydroxyl group starts to generate at 0.3 V and reaches to 93% coverage at 1.2 V. For the Pd black in Figure 6-5c, formate forms at 0.01 V and achieves 5.8% coverage at 1.0 V, and slightly decreases with increasing potential; the hydroxyl group begins to accumulate on the surface at 0.3 V and reach to 94% coverage at 1.0 V. Comparison between the Au/Pd nanoparticles and Pd black suggests higher formate and lower hydroxyl coverage on the Au/Pd nanoparticles especially at higher potentials. Most important, hydroxyl adsorption on Au/Pd nanoparticles has been remarkably delayed. For example, the hydroxyl coverage of 0.1, i.e., $\theta_{OH} = 0.1$, occurs at ca. 0.59V for the Au/Pd nanoparticles but at 0.48V for the Pd black. Since hydroxyl group on the Pd surface (PdOH), as a product of surface oxidation, has been widely considered as a poisoning species which would inhibit the catalytic activity. As a result, the anti-oxidation property of the Au/Pd nanoparticles promotes both electrochemical activity toward FAO and durability of Pd during the AST.

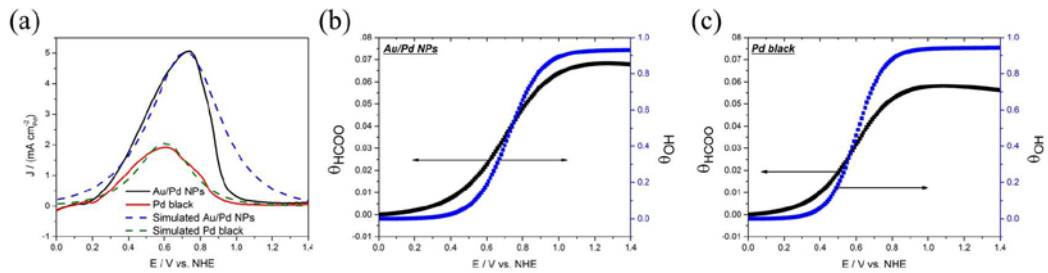

Figure 6-5 (a) Comparison of experimental (solid line) and simulated (dot line) results of the Au/Pd nanoparticles and Pd black. The simulated surface coverage of formate and hydroxyl group for (b) Au/Pd nanoparticles and (c) Pd black in different potentials, respectively.

Table 6-2 Parameters of simulation model

Parameters	Values (Au/Pd nanoparticles)	Values (Pd black)	Unit
scan range	0-1.4	0-1.4	V
scan rate	10	10	mVs^{-1}
k_1	$1.0x10^{-3}$	$3.2x10^{-4}$	A cm^{-2} M^{-1}
k_2	$3.3x10^{-5}$	$3.3x10^{-5}$	A cm^{-2} M^{-1}
k_{-2}	60	60	A cm^{-2} M^{-1}
k_3	$1.0x10^{-5}$	$1.0x10^{-5}$	A cm^{-2} M^{-1}
k_{-3}	$9x10^{-7}$	$9x10^{-7}$	A cm^{-2} M^{-1}
k_4	$4.0x10^{-3}$	$4.0x10^{-3}$	A cm^{-2} M^{-1}
C_w	55.6	55.6	M
q	0.02016	0.02016	C cm^{-2}
C_f	0.1	0.1	M
C_H	0.1	0.1	M
b_1	0.19	0.16	V
b_2	0.18	0.15	V
b_3	0.18	0.15	V

6.4.2.2 Thickness of the Palladium Layer

The numerical model was employed to understand the impact of the Pd thickness in the Au/Pd nanoparticles on the FAO reactions. Herein, the comparison between simulated (red-dot line) and experimental (black-solid line, reploted from the results in Chapter 3.6.3) results of the Au/Pd nanoparticles and the Pd black are discussed. . Figure 6-6 shows both the anodic FAO curves and intermediate coverage distributions. It is apparent that the simulated curves agree well with the experimental results in general; however, the experimental curves bend down significantly at higher potentials possibly due to intermediates accumulation on the surface of catalysts. This phenomenon was more obvious for AuPd10 (i.e. Au/Pd nanoparticles which Cu coated for 10 minutes) than AuPd40. The peak current densities of FAO were 5.25 mA cm^{-1} (AuPd10), 5 mA cm^{-1} (AuPd20), 3.75 mA cm^{-1} (AuPd30), 2.25 mA cm^{-1} (AuPd40), and 1.88 mA cm^{-1} (Pd black) for different samples as shown in Figure 6-6, which indicating that the higher FAO activities result from thinner Pd shells. In addition, the Tafel slope of b_1 employed in the simulation to fit the experimental curves are 0.21 (AuPd10), 0.215 (AuPd20), 0.21 (AuPd30), 0.19 (AuPd 40) and 0.165 (Pd black), respectively, which decreases with the thicker thickness (i.e., particle size). The coverage of intermediates showed that less formate and hydroxyl groups occupied on the surface of the Au/Pd nanoparticles than the Pd black at the same applied potential (e.g., 0.6V), leaving more active sites for FAO. Besides, the same coverage of hydroxyl (OH_{ads}) group (i.e. 0.2; 20% coverage on the Pd surface) appears at lower potential on Pd black than the Au/Pd nanoparticles, which may suggest that PdOH will likely form on the catalyst surface to diminish the catalytic ability due to the site-blocking effect.

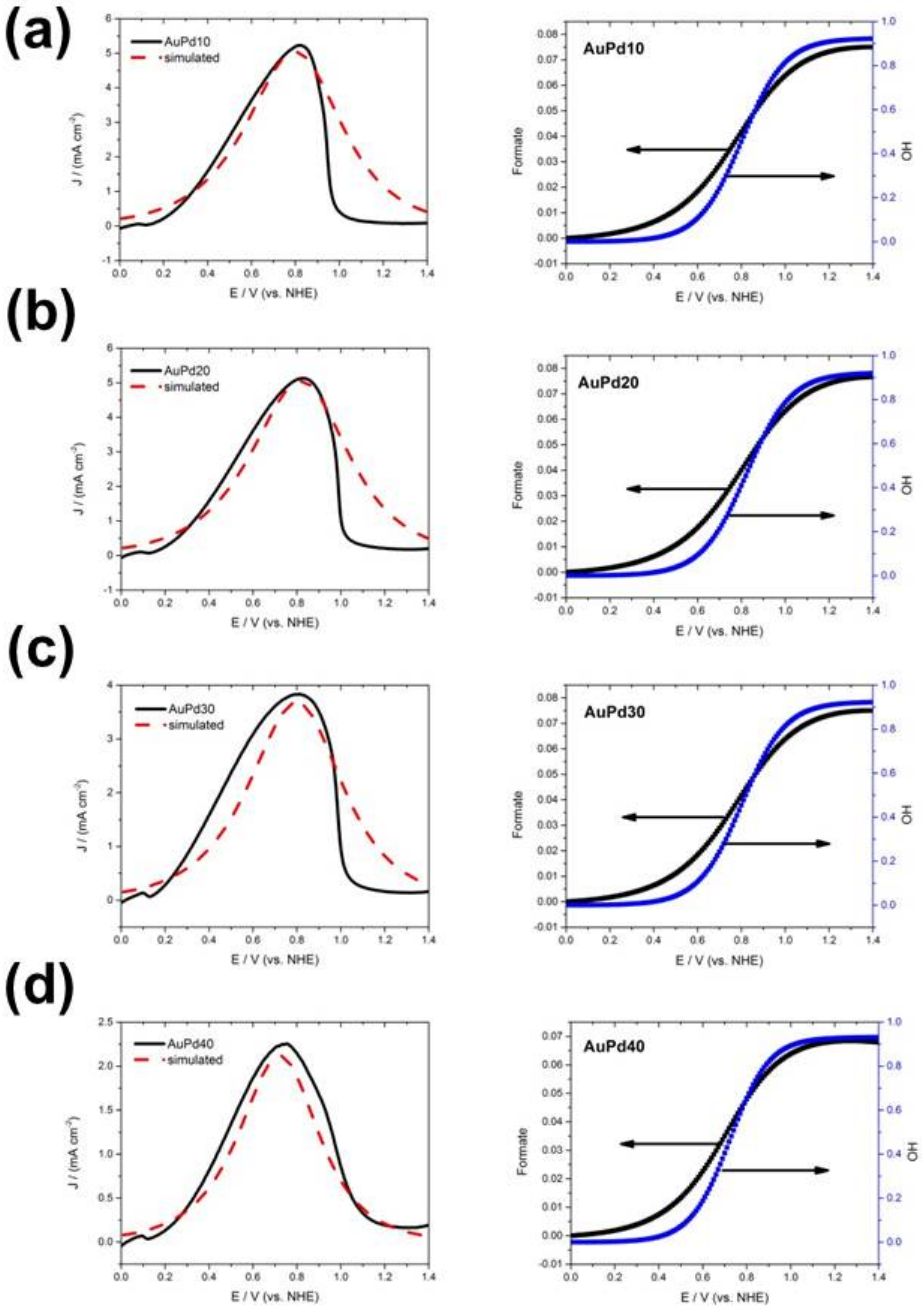

Figure 6-6 Simulation of Au/Pd nanoparticles and the coverage (Θ) of formate and hydroxyl in different thickness.

6.4.2.3 Type of the Formate-based Solutions

The similar model was also developed and used to understand the mechanism of the electro-oxidation of formate-based solutions. The parameters used in this simulation were shown in Table 6-3. Figure 6-7 compares the anodic oxidation curves from experiment (solid-line) and simulation (dot-line), and shows the coverage of formate and hydroxyl species in 0.1 M FA (Figure 6-7a), 0.1 M SF (Figure 6-7b) and mixed solutions (0.1 M SF + 0.5 M FA, Figure 6-7c) for both the Au/Pd nanoparticles and the Pd black. Overall the simulated current densities agree well with the experimental results; however, observable differences are evident in the higher potential region possibly due to intermediate accumulation. Moreover, for the SF-containing solutions the simulated curves show lower current densities than the experimental ones before reaching the peak potential as shown in Figure 6-7b and 6-7c. The above discrepancies may result from the fast scanning rate (10 mV s^{-1}) which leads to higher current densities whereas a near-steady state was simulated instead. Nevertheless, the surface coverages of both formate and hydroxyl species could still be valuable to provide insights on oxidation mechanisms. As well known, the catalytic efficiency depends on the rate of removing reaction intermediates from the catalyst surface (generating more active-sites). The simulated results suggest lower formate and hydroxyl coverages at the same applied potential for the Au/Pd nanoparticles than the Pd black in all formate-based solutions. In other words, higher potentials are required for the Au/Pd nanoparticles to achieve the same coverages of hydroxyl and formate than the Pd black. For example, at a OH coverage of 0.2 (meaning 20% coverage on the catalyst surface) the Au/Pd nanoparticles shows higher potentials in the solutions (0.5 M FA + 0.1 M SF: 1.15 V; 0.1 M SF: 0.97 V; FA: 0.66 V) than those of the Pd black (0.5 M FA + 0.1 M SF: 1.02 V; SF: 0.94 V; FA: 0.64 V). At a formate coverage of 0.02 a similar trend still holds: higher potentials for the Au/Pd nanoparticles (0.5 M FA + 0.1 M SF: 0.89 V; 0.1 M SF: 0.81 V; FA: 0.60 V) than those of

the Pd black (0.5 M FA + 0.1 M SF: 0.81 V; 0.1 M SF: 0.76 V; FA: 0.58 V). This suggests that Pd oxidation (corresponding to Pd-OH formation) has been retarded and formate-consuming rate could have been boosted on the Au/Pd nanoparticles. These differences are believed to result from electronic coupling and/or geometric factors in the core-shell nanoparticles.

On the other hand, comparison between different solutions in Figure 6-7 for one specific catalyst suggests that the SF-containing solutions, e.g., 0.1 M SF and the mixed solution (0.5 M FA + 0.1 M SF), significantly shift the anodic oxidation peak potentials positively. The volcano curves shown in Figure 6-7a for FAO are nearly symmetric with the two branches at either side of the peak. With additional formate species in the solutions, however, the volcano curves are distorted and the left branches are significantly expanded. This is because that saturation of hydroxyl and formate at catalyst surface is postponed to higher potentials at higher concentrations of SF. Figure6-7b and 6-7c clear show that saturation of hydroxyl and formate has not been yet reached even at 1.4 V. This also indicates relative lower OH coverages within the entire potential window for the formate-based solutions. For example, the OH coverages on the AuPd NPs at 1.4 V are 90%, 70%, and 50% in 0.1 M FA, 0.1 M SF, and the mixed solution of 0.5 M FA + 0.1 M SF, respectively. The lowest OH coverage in the mixed solution is believed to provide more active sites and contribute to the highest electro-oxidation currents.

Table 6-3 Parameter for the simulation of formate-based electro-oxidations

Parameters	Au/Pd NPs	Pd black	Unit
A_1	FA: 8.0×10^{-5} SF: 9.6×10^{-5} FA+SF: 1.23×10^{-4}	FA: 5.0×10^{-5} SF: 3.45×10^{-5} FA+SF: 6.8×10^{-5}	A cm^{-2}
A_2	1.83×10^{-3}	1.83×10^{-3}	A cm^{-2}
A_{-2}	6	6	A cm^{-2}
A_3	1×10^{-6}	1×10-6	A cm^{-2}
A_{-3}	9×10^{-8}	9×10^{-8}	A cm^{-2}
A_4	4×10^{-5}	4×10^{-5}	A M cm^{-2}
b_1	FA: 0.205 SF: 0.315 FA+SF: 0.35	FA: 0.195 SF: 0.287 FA+SF: 0.308	V
b_2	FA: 0.195 SF: 0.305 FA+SF: 0.34	FA: 0.185 SF: 0.277 FA+SF: 0.298	V
b_3	FA: 0.195 SF: 0.305 FA+SF: 0.34	FA: 0.185 SF: 0.277 FA+SF: 0.298	V
q	0.02016	0.02016	C cm^{-2}

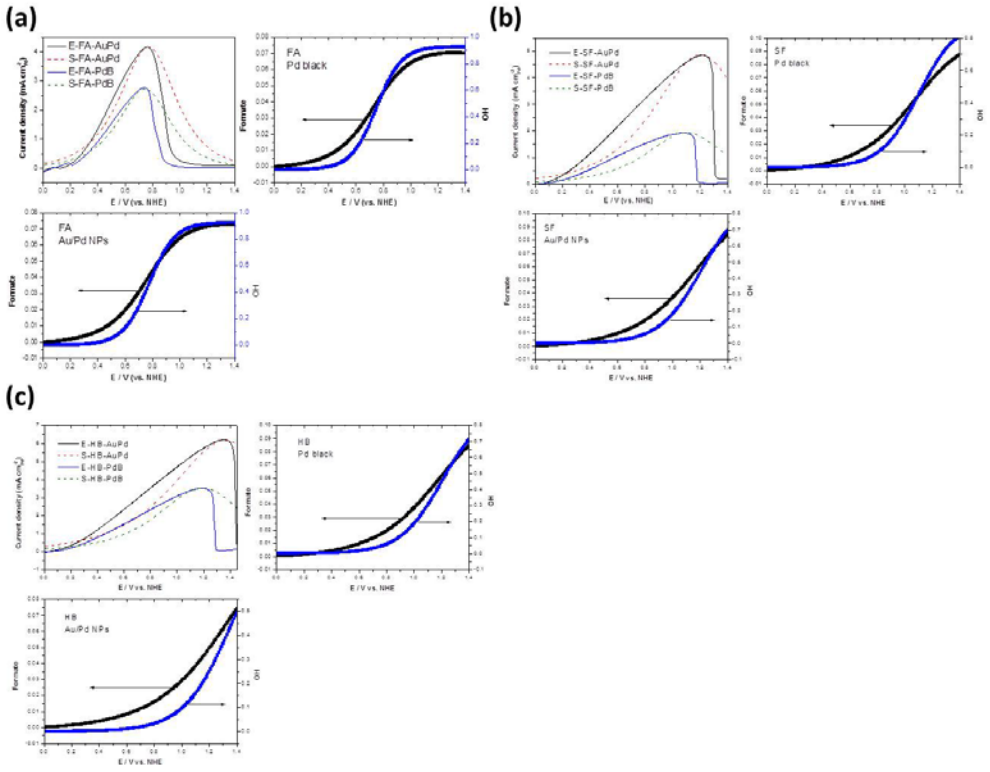

Figure 6-7 Experimental (solid-line) and simulated (dot-line) results, and the coverage of formate and hydroxyl for the Au/Pd nanoparticles and the Pd black in (a) 0.1 M formic acid, (b) 0.1 M sodium formate, and (c) mixed solution of 0.5 M formic acid + 0.1 M sodium formate.

6.4.3 Summary of Geometric Effect and Electronic Effect

In this study, XPS was used to identify the electronic configuration of the Pd layer. Many reports [28,40] claimed that a lower core-level binding energy of Pd $3d_{5/2}$ will weaken the formate binding to the catalysts and promote the FAO activity (promote the direct formic acid pathway). In chapter 3, we already discussed the impact of Pd layer thickness on the FAO activity and CO oxidation. In addition, the Au effects (i.e., Au roughness, Au particle size) were discussed in chapter 5. In order to evaluate the geometric and electronic effect between the Pd shell and Au core, we summarized the data from the experiment and simulation results. In Figure 6-8, (a) is for the impact of Pd

thickness from chapter 3, (b) is for the influence of Au particle sizes from chapter 5, and (c) is for the impact of the Au roughness from chapter 5, respectively. The experimental results including Pd thickness, Au/Pd particle size and CO oxidation peak were combined with simulation data particularly k1 (reaction kinetic constant in direct FAO pathway) and b1 (Tafel slope in direct FAO pathway) at various Pd $3d_{5/2}$ binding energy. Here, k1 and b1 are the parameters we used in simulation to express the kinetics of the direct FAO pathway which primarily determined the FAO reaction rate.

According to the Figure 6-8, we found that changes in either the Pd shell or the inner Au core will shift the binding energy and hence influence the electrooxidation ability (i.e., FAO, CO oxidation ability). We organized the following findings according to Figure 6-8:

(1) With the increase of Pd thickness and Au/Pd particle size, the Pd $3d_{5/2}$ binding energy increases (Figure 6-8 a). This indicates that thicker Pd shells or larger Au/Pd particle size diminish the electronic couplings between the core and shell.

(2) A lower CO oxidation peak potential corresponds to a lower Pd $3d_{5/2}$ binding energy . As previously mentioned, the lower Pd $3d_{5/2}$ binding energy will weaken the formate binding. It may also affect the binding of CO because a higher binding energy between Pd and CO will hinder the CO oxidation.

(3) k1 and b1 are generally proportional to the Pd $3d_{5/2}$ binding energy. The increase of Pd $3d_{5/2}$ binding energy will enhance the formate binding and hence retard the overall FAO reaction.

Overall, we concluded the Pd $3d_{5/2}$ core-level binding energy shift can be affected by either Pd shell thickness changes or morphology of the inner Au core. Our results showed that the two effects are combined in many cases in determining the overall FAO and CO oxidation ability of the core-shell Au-Pd nanoparticles.

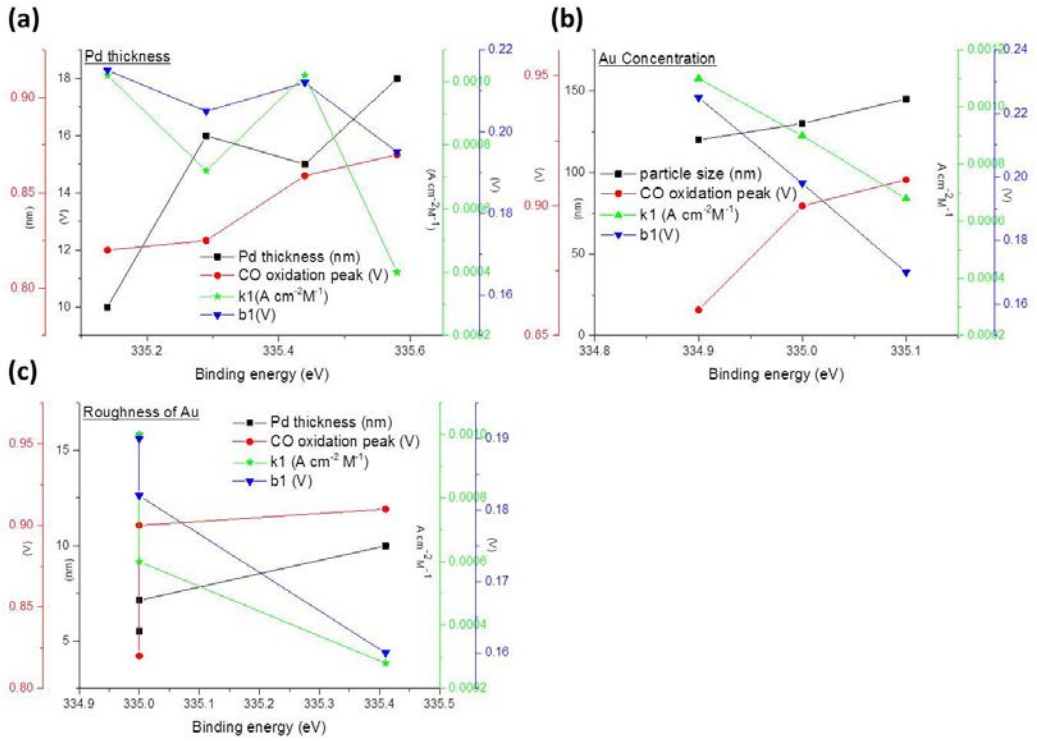

Figure 6-8 The binding energy changes from the (a) Pd thickness, (b) Au concentration, and (c) Au roughness with the Pd shell thickness, CO oxidation peak, k1 and b1.

Chapter 7

Conclusion

Au-M (M=Pd and PtCu) core-shell nanoparticles can serve as highly active catalysts for formic acid oxidation and oxygen reduction reaction. In this dissertation, we aim to understand microstructures and electrochemical properties of these core-shell nanoparticles to be used in direct formic acid fuel cells.

The Au/PtCu catalysts show well-defined core-shell structure with the PtCu shell and stabilizing Au core. It is found that the PtCu alloy was formed after replacement of the Cu layer and up to 80 wt. % Cu was substituted by Pt. The thickness of PtCu can be controlled by the Cu coating time. Compared to commercial Pt catalysts, the Au/PtCu catalysts express superior specific activity and mass activity evaluated from the oxygen reduction reaction polarization curves. In addition, the calculated number of electrons transferred from Koutecky-Levich plot is close to four, indicating the catalysts could efficiently reduce O_2 to H_2O during ORR. Moreover, the CO-stripping studies suggest optimum electronic coupling between the PtCu shell and Au core in the catalysts. The long-term durability test of the Au/PtCu 20 catalyst carried out in acid solution showed less than 5% loss of ECSA after 14k potential cycles, majorly due to its unique structure.

In the Au/Pd core-shell nanoparticles, it was found that the coating time of Cu significantly impact Pd shell morphology: a discontinuous Pd shell with isolated islands was formed within 10 minutes Cu coating and on the other hand continuous Pd layers were obtained with longer coating time showing porous structures. The electrochemical results indicated that the Au/Pd nanoparticles exhibited excellent catalytic activities in formic acid oxidation, stability (chronoamperometry), and long-term durability compared with the commercial Pd black. Especially, Au/Pd20 (Cu coating time: 20 minutes) nanoparticles in this study displayed the best catalytic properties due to the optimum Au-

Pd electronic coupling, showing the largest Pd binding energy shift. The hollow gold core in this structure may play a crucial role to donate electrons and stabilize the Pd shell.

Roughness and particle size of the Au-core in the Au/Pd core-shell nanoparticles also showed a great impact on the formic acid oxidation. Small Au nanoparticles with smooth surfaces coated with Pd demonstrated superior formic acid oxidation activities, CO oxidation ability, electrochemical stabilities, and long-term durability than Pd black. Particularly, the Au25Pd (smallest Au particles) nanoparticles synthesized in this study present the best catalytic properties due to their unique structure. The hollow and porous gold cores tuned by reduced Au concentrations in the core/shell structures may influence Pd distribution and morphologies on the Au core. In addition, the surface roughness of Au nanoparticles was tuned by adding different concentration of Na_2SO_3 solution. The higher concentration of Na_2SO_3 in the Au solution generated rougher Au surface; however, the defects of the Pd layer on the Au/Pd core-shell structure increased accordingly. These defects retard the electrochemical reaction of formic acid oxidation on the catalysts.

An electrochemical model was built to provide insights of the formic acid oxidation reaction mechanism. Computational simulation suggested that the distortion of the volcano curves from the formate-based electro-oxidation is due to a postponed saturation of reaction intermediates such as hydroxyl and formate at catalyst surface to higher potentials, especially using higher concentrations of sodium formate. Additionally in situ Raman spectroscopy combined with CO stripping test showed a weaker CO adsorption on the core-shell nanoparticles, suggesting a strong electronic coupling between Au and Pd which could further postpone the saturation of formate and hydroxyl species on the Pd surface. It was found from simulation that smooth Au surface and thin Pd shell thickness help reduce the formate and hydroxyl coverage on the core-shell nanoparticles than those of the Pd black in the same applied potential, indicating efficiently oxidized these intermediates to promote formic acid oxidation.

Appendix A

Code of the Anodic Curve of FAO on Au/Pd Nanoparticles

```
# include "udf.h"
# include "id.h"
# include "mem.h"
# include "sg.h"
#define e0 0.0 /* starting potential */
#define e1 1.4 /* end potential */
#define scanrate 10.0 /* voltage scan rate in mV/s */
#define k1 0.001 /* kinetic const. of FA oxidized to CO2, no use here*/
#define k2 0.000033 /* kinetic const. of H2O */
#define k_2 60.0
#define k3 0.00001 /* kinetic const. of Formate */
#define k_3 0.0000009
#define k4 0.004/* kinetic const. of overall reaction */
#define Cw 55.6 /* pure H2O=(1000/18)/1L*/
#define Cf 0.1 /* formic acid concentration */
#define Ch 0.1
#define q1 0.02016 /* 210*1.2/0.125; charge of H */
#define q2 0.02016 /* 210*1.2/0.125 charge of H */
#define b1 0.19
#define b2 0.18
#define b3 0.18 /* relate to formate */
/* C_UDSI(c,t,0) thita_FA */
/* C_UDSI(c,t,1) thita_OH */
/*************************************************************************************************/
    DEFINE_SOURCE(thita_FA,c,t,dS,eqn)
```

```
{
real source,phai,t0;
t0=(e1-e0)/scanrate*1000.0; /* time needed to scan from e0 to e1 in seconds */
if (CURRENT_TIME<t0)
phai=e0+CURRENT_TIME*scanrate/1000.0;
else
phai=e0+e1-(CURRENT_TIME-t0)*scanrate/1000.0;
source=(1.0/q1)*(k3*Cf*(1.0-C_UDSI(c,t,0)-C_UDSI(c,t,1))*exp(phai/b3)-
k_3*Ch*C_UDSI(c,t,0)*exp(-p
hai/b3)-k4*C_UDSI(c,t,0)*C_UDSI(c,t,1)*Cf*Ch);
dS[eqn]=(1.0/q1)*(k3*(-1.0)*Cf*exp(phai/b3)-k_3*Ch*exp(-phai/b3)-
k4*C_UDSI(c,t,1)*Cf*Ch);
return source;
}
/*****************************************************************************************/
DEFINE_SOURCE(thita_OH,c,t,dS,eqn)
{
real source,phai,t0;
t0=(e1-e0)/scanrate*1000.0; /* time needed to scan from e0 to e1 in seconds */
if (CURRENT_TIME<t0)
phai=e0+CURRENT_TIME*scanrate/1000.0; /* potential */
else
phai=e0+e1-(CURRENT_TIME-t0)*scanrate/1000.0;
source=(1.0/q2)*(k2*Cw*(1.0-C_UDSI(c,t,0)-C_UDSI(c,t,1))*exp(phai/b2)-
k_2*Ch*C_UDSI(c,t,1)*exp(-phai/b2)-k4*C_UDSI(c,t,0)*C_UDSI(c,t,1)*Cf*Ch);
```

```
dS[eqn]=(1.0/q2)*(k2*Cw*(-1.0)*exp(phai/b2)-k_2*Ch*exp(-phai/b2)-
k4*C_UDSI(c,t,0)*Cf*Ch);
return source;
}
/****************calculate surface concentration curves **************/
DEFINE_EXECUTE_AT_END(coverages)
{
real phai,t0,current;
Domain *d= Get_Domain(1);
Thread *t = Lookup_Thread(d,2);
FILE *f1;
t0=(e1-e0)/scanrate*1000.0; /* time needed to scan from e0 to e1 in seconds */
1
if (CURRENT_TIME<t0)
phai=e0+CURRENT_TIME*scanrate/1000.0;
else
phai=e0+e1-(CURRENT_TIME-t0)*scanrate/1000.0;
current=2*k1*Cf*(1.0-C_UDSI(0,t,0)-C_UDSI(0,t,1))*exp(phai/b1)+k2*Cw*(1.0-
C_UDSI(0,t,0)-C_UDSI(0,
t,1))*exp(phai/b2)-(k_2*Ch*C_UDSI(0,t,1)*exp(-phai/b2))+
k3*Cf*(1-C_UDSI(0,t,0)-C_UDSI(0,t,1))*exp(phai/b3)-k_3*Ch*C_UDSI(0,t,0)*exp(-
phai/b3);
f1=fopen("curve.txt","a");
fprintf(f1,"%12.8e %12.8e %12.8e %12.8e %12.8e\n",CURRENT_TIME, phai,
C_UDSI(0,t,0), C_UDSI(0,t,1), current);fclose (f1);}
```

Appendix B

Code of the Anodic Curve of FAO on Pd Black

```
# include "udf.h"
# include "id.h"
# include "mem.h"
# include "sg.h"
#define e0 0.0 /* starting potential */
#define e1 1.4 /* end potential */
#define scanrate 10.0 /* voltage scan rate in mV/s */
#define k1 0.00032 /* kinetic const. of FA oxidized to CO2, no use here*/
#define k2 0.000033 /* kinetic const. of H2O */
#define k_2 60.0
#define k3 0.00001 /* kinetic const. of Formate */
#define k_3 0.0000009
#define k4 0.004/* kinetic const. of overall reaction */
#define Cw 55.6 /* pure H2O=(1000/18)/1L*/
#define Cf 0.1 /* formic acid concentration */
#define Ch 0.1
#define q1 0.02016 /* 210*1.2/0.125; charge of H */
#define q2 0.02016 /* 210*1.2/0.125 charge of H */
#define b1 0.16
#define b2 0.15
#define b3 0.15 /* relate to formate */
/* C_UDSI(c,t,0) thita_FA */
/* C_UDSI(c,t,1) thita_OH */
/*************************************************************************************************/
DEFINE_SOURCE(thita_FA,c,t,dS,eqn)
```

```
{
real source,phai,t0;
t0=(e1-e0)/scanrate*1000.0; /* time needed to scan from e0 to e1 in seconds */
if (CURRENT_TIME<t0)
phai=e0+CURRENT_TIME*scanrate/1000.0;
else
phai=e0+e1-(CURRENT_TIME-t0)*scanrate/1000.0;
source=(1.0/q1)*(k3*Cf*(1.0-C_UDSI(c,t,0)-C_UDSI(c,t,1))*exp(phai/b3)-
k_3*Ch*C_UDSI(c,t,0)*exp(-p
hai/b3)-k4*C_UDSI(c,t,0)*C_UDSI(c,t,1)*Cf*Ch);
dS[eqn]=(1.0/q1)*(k3*(-1.0)*Cf*exp(phai/b3)-k_3*Ch*exp(-phai/b3)-
k4*C_UDSI(c,t,1)*Cf*Ch);
return source;
}
/*************************************************************************************************/
DEFINE_SOURCE(thita_OH,c,t,dS,eqn)
{
real source,phai,t0;
t0=(e1-e0)/scanrate*1000.0; /* time needed to scan from e0 to e1 in seconds */
if (CURRENT_TIME<t0)
phai=e0+CURRENT_TIME*scanrate/1000.0; /* potential */
else
phai=e0+e1-(CURRENT_TIME-t0)*scanrate/1000.0;
source=(1.0/q2)*(k2*Cw*(1.0-C_UDSI(c,t,0)-C_UDSI(c,t,1))*exp(phai/b2)-
k_2*Ch*C_UDSI(c,t,1)*exp(-p
```

```
hai/b2)-k4*C_UDSI(c,t,0)*C_UDSI(c,t,1)*Cf*Ch);
dS[eqn]=(1.0/q2)*(k2*Cw*(-1.0)*exp(phai/b2)-k_2*Ch*exp(-phai/b2)-
k4*C_UDSI(c,t,0)*Cf*Ch);
return source;
}
/********** calculate surface concentration curves *******/
DEFINE_EXECUTE_AT_END(coverages)
{
real phai,t0,current;
Domain *d= Get_Domain(1);
Thread *t = Lookup_Thread(d,2);
FILE *f1;
t0=(e1-e0)/scanrate*1000.0; /* time needed to scan from e0 to e1 in seconds */
1
if (CURRENT_TIME<t0)
phai=e0+CURRENT_TIME*scanrate/1000.0;
else
phai=e0+e1-(CURRENT_TIME-t0)*scanrate/1000.0;
current=2*k1*Cf*(1.0-C_UDSI(0,t,0)-C_UDSI(0,t,1))*exp(phai/b1)+k2*Cw*(1.0-
C_UDSI(0,t,0)-C_UDSI(0,
t,1))*exp(phai/b2)-(k_2*Ch*C_UDSI(0,t,1)*exp(-phai/b2))+
k3*Cf*(1-C_UDSI(0,t,0)-C_UDSI(0,t,1))*exp(phai/b3)-k_3*Ch*C_UDSI(0,t,0)*exp(-
phai/b3);
f1=fopen("curve.txt","a");
```

```
fprintf(f1,"%12.8e %12.8e %12.8e %12.8e %12.8e\n",CURRENT_TIME, phai,
C_UDSI(0,t,0), C_UDSI(0,t,1), current);
fclose (f1);
}
```

References

[1] Baldauf M., Kolb D. M. Formic Acid Oxidation on Ultrathin Pd Films on Au(hkl) and Pt(hkl) Electrodes. The Journal of Physical Chemistry. 1996;100:11375-81.

[2] Winters A. L., Fychan R., Jones R. Effect of formic acid and a bacterial inoculant on the amino acid composition of grass silage and on animal performance. Grass and Forage Science. 2001;56:181-92.

[3] Rice C., Ha S., Masel R. I., Waszczuk P., Wieckowski A., Barnard T. Direct formic acid fuel cells. Journal of Power Sources. 2002;111:83-9.

[4] Rice C., Ha S., Masel R. I., Wieckowski A. Catalysts for direct formic acid fuel cells. Journal of Power Sources. 2003;115:229-35.

[5] Ha S., Larsen R., Zhu Y., Masel R. I. Direct Formic Acid Fuel Cells with 600 mA cm–2 at 0.4 V and 22 °C. Fuel Cells. 2004;4:337-43.

[6] Zhu Y., Ha S. Y., Masel R. I. High power density direct formic acid fuel cells. Journal of Power Sources. 2004;130:8-14.

[7] Ha S., Larsen R., Masel R. I. Performance characterization of Pd/C nanocatalyst for direct formic acid fuel cells. Journal of Power Sources. 2005;144:28-34.

[8] Tian M., Conway B. E. Phenomenology of oscillatory electro-oxidation of formic acid at Pd: role of surface oxide films studied by voltammetry, impedance spectroscopy and nanogravimetry. Journal of Electroanalytical Chemistry. 2005;581:176-89.

[9] Hoshi N., Kida K., Nakamura M., Nakada M., Osada K. Structural Effects of Electrochemical Oxidation of Formic Acid on Single Crystal Electrodes of Palladium. J Phys Chem B. 2006;110:12480-4.

[10] Zhou W. P., Lewera A., Larsen R., Masel R. I., Bagus P. S., Wieckowski A. Size Effects in Electronic and Catalytic Properties of Unsupported Palladium Nanoparticles in Electrooxidation of Formic Acid. J Phys Chem B. 2006;110:13393-8.

[11] Yu X., Pickup P. G. Recent advances in direct formic acid fuel cells (DFAFC). Journal of Power Sources. 2008;182:124-32.

[12] Chai J., Li F., Hu Y., Zhang Q., Han D., Niu L. Hollow flower-like AuPd alloy nanoparticles: One step synthesis, self-assembly on ionic liquid-functionalized graphene, and electrooxidation of formic acid. Journal of Materials Chemistry. 2011;21:17922-9.

[13] Kuai L., Yu X., Wang S., Sang Y., Geng B. Au–Pd Alloy and Core–Shell Nanostructures: One-Pot Coreduction Preparation, Formation Mechanism, and Electrochemical Properties. Langmuir. 2012;28:7168-73.

[14] Sankar M., He Q., Morad M., Pritchard J., Freakley S. J., Edwards J. K., et al. Synthesis of Stable Ligand-free Gold–Palladium Nanoparticles Using a Simple Excess Anion Method. ACS Nano. 2012;6:6600-13.

[15] Villa A., Wang D., Veith G. M., Prati L. Bismuth as a modifier of Au–Pd catalyst: Enhancing selectivity in alcohol oxidation by suppressing parallel reaction. Journal of Catalysis. 2012;292:73-80.

[16] Wu M.-L., Chen D.-H., Huang T.-C. Synthesis of Au/Pd Bimetallic Nanoparticles in Reverse Micelles. Langmuir. 2001;17:3877-83.

[17] Chen Y.-H., Tseng Y.-H., Yeh C.-S. Laser-induced alloying Au-Pd and Ag-Pd colloidal mixtures: the formation of dispersed Au/Pd and Ag/Pd nanoparticles. Journal of Materials Chemistry. 2002;12:1419-22.

[18] dos Santos M. L., de Souza P., de Vercik L. C., Guastaldi A. C. Microstructural study of the resistance to corrosion of laser welded AuPd alloy joints for prosthesis supported by implants. Ecletica Quim. 2002;27:185-99.
[19] Łukaszewski M., Czerwiński A. Electrochemical behavior of palladium–gold alloys. Electrochimica Acta. 2003;48:2435-45.
[20] Ge Z. B., Cahill D. G., Braun P. V. AuPd metal nanoparticles as probes of nanoscale thermal transport in aqueous solution. J Phys Chem B. 2004;108:18870-5.
[21] Pawelec B., Venezia A. M., La Parola V., Cano-Serrano E., Campos-Martin J. M., Fierro J. L. G. AuPd alloy formation in Au-Pd/Al2O3 catalysts and its role on aromatics hydrogenation. Applied Surface Science. 2005;242:380-91.
[22] Mejía-Rosales S. J., Fernández-Navarro C., Pérez-Tijerina E., Blom D. A., Allard L. F., José-Yacamán M. On the Structure of Au/Pd Bimetallic Nanoparticles. J Phys Chem C. 2006;111:1256-60.
[23] Lee Y. W., Kim N. H., Lee K. Y., Kwon K., Kim M., Han S. W. Synthesis and Characterization of Flower-Shaped Porous Au−Pd Alloy Nanoparticles. J Phys Chem C. 2008;112:6717-22.
[24] Liu F., Wechsler D., Zhang P. Alloy-structure-dependent electronic behavior and surface properties of Au–Pd nanoparticles. Chemical Physics Letters. 2008;461:254-9.
[25] Abdelsayed V., Aljarash A., El-Shall M. S., Al Othman Z. A., Alghamdi A. H. Microwave Synthesis of Bimetallic Nanoalloys and CO Oxidation on Ceria-Supported Nanoalloys. Chemistry of Materials. 2009;21:2825-34.
[26] Liu F., Zhang P. Tailoring the local structure and electronic property of AuPd nanoparticles by selecting capping molecules. Appl Phys Lett. 2010;96.
[27] Kinoshita K. Particle size effects for oxygen reduction on highly dispersed platinum in acid electrolytes. Journal of The Electrochemical Society. 1990;137:845-8.
[28] Mavrikakis M., Hammer B., Nørskov J. K. Effect of Strain on the Reactivity of Metal Surfaces. Physical Review Letters. 1998;81:2819-22.
[29] Kibler L. A., El-Aziz A. M., Hoyer R., Kolb D. M. Tuning Reaction Rates by Lateral Strain in a Palladium Monolayer. Angewandte Chemie International Edition. 2005;44:2080-4.
[30] Wilson O. M., Knecht M. R., Garcia-Martinez J. C., Crooks R. M. Effect of Pd Nanoparticle Size on the Catalytic Hydrogenation of Allyl Alcohol. Journal of the American Chemical Society. 2006;128:4510-1.
[31] Peng Z., Yang H. Designer platinum nanoparticles: Control of shape, composition in alloy, nanostructure and electrocatalytic property. Nano Today. 2009;4:143-64.
[32] Koel B. E., Sellidj A., Paffett M. T. Ultrathin films of Pd on Au(111): Evidence for surface alloy formation. Physical Review B. 1992;46:7846-56.
[33] Hammer B., Nørskov J. K. Theoretical surface science and catalysis—calculations and concepts. In: Bruce C. Gates HK, editor. Advances in Catalysis: Academic Press; 2000. p. 71-129.
[34] Stamenkovic V., Mun B. S., Mayrhofer K. J. J., Ross P. N., Markovic N. M., Rossmeisl J., et al. Changing the Activity of Electrocatalysts for Oxygen Reduction by Tuning the Surface Electronic Structure. Angewandte Chemie International Edition. 2006;45:2897-901.
[35] Bus E., van Bokhoven J. A. Electronic and Geometric Structures of Supported Platinum, Gold, and Platinum−Gold Catalysts. J Phys Chem C. 2007;111:9761-8.

[36] Park I.-S., Lee K.-S., Choi J.-H., Park H.-Y., Sung Y.-E. Surface Structure of Pt-Modified Au Nanoparticles and Electrocatalytic Activity in Formic Acid Electro-Oxidation. J Phys Chem C. 2007;111:19126-33.
[37] Mani P., Srivastava R., Strasser P. Dealloyed Pt−Cu Core−Shell Nanoparticle Electrocatalysts for Use in PEM Fuel Cell Cathodes. J Phys Chem C. 2008;112:2770-8.
[38] Zhou W., Lee J. Y. Highly active core–shell Au@Pd catalyst for formic acid electrooxidation. Electrochemistry Communications. 2007;9:1725-9.
[39] Fang P.-P., Duan S., Lin X.-D., Anema J. R., Li J.-F., Buriez O., et al. Tailoring Au-core Pd-shell Pt-cluster nanoparticles for enhanced electrocatalytic activity. Chemical Science. 2011;2:531-9.
[40] Hong J. W., Kim D., Lee Y. W., Kim M., Kang S. W., Han S. W. Atomic-Distribution-Dependent Electrocatalytic Activity of Au-Pd Bimetallic Nanocrystals. Angew Chem-Int Edit. 2011;50:8876-80.
[41] Strasser P., Koh S., Anniyev T., Greeley J., More K., Yu C., et al. Lattice-strain control of the activity in dealloyed core–shell fuel cell catalysts. Nat Chem. 2010;2:454-60.
[42] Haruta M. Gold as a novel catalyst in the 21st century: Preparation, working mechanism and applications. Gold Bulletin. 2004;37:27-36.
[43] Sardar R., Funston A. M., Mulvaney P., Murray R. W. Gold Nanoparticles: Past, Present, and Future. Langmuir. 2009;25:13840-51.
[44] Zhao P., Li N., Astruc D. State of the art in gold nanoparticle synthesis. Coordination Chemistry Reviews. 2013;257:638-65.
[45] Sengupta A., Laucks M., Dildine N., Drapala E., Davis E. Bioaerosol characterization by surface-enhanced Raman spectroscopy (SERS). Journal of aerosol science. 2005;36:651-64.
[46] Miyake H., Okada T., Samjeske G., Osawa M. Formic acid electrooxidation on Pd in acidic solutions studied by surface-enhanced infrared absorption spectroscopy. Physical Chemistry Chemical Physics. 2008;10:3662-9.
[47] Zhang K., Xiang Y., Wu X., Feng L., He W., Liu J., et al. Enhanced Optical Responses of Au@Pd Core/Shell Nanobars. Langmuir. 2008;25:1162-8.
[48] Yang Z., Li Y., Li Z., Wu D., Kang J., Xu H., et al. Surface enhanced Raman scattering of pyridine adsorbed on Au@Pd core/shell nanoparticles. The Journal of Chemical Physics. 2009;130:234705-7.
[49] Chen Y., Lim H., Tang Q., Gao Y., Sun T., Yan Q., et al. Solvent-free aerobic oxidation of benzyl alcohol over Pd monometallic and Au–Pd bimetallic catalysts supported on SBA-16 mesoporous molecular sieves. Applied Catalysis A: General. 2010;380:55-65.
[50] Duan S., Fang P.-P., Fan F.-R., Broadwell I., Yang F.-Z., Wu D.-Y., et al. A density functional theory approach to mushroom-like platinum clusters on palladium-shell over Au core nanoparticles for high electrocatalytic activity. Physical Chemistry Chemical Physics. 2011;13:5441-9.
[51] Hu J.-W., Zhang Y., Li J.-F., Liu Z., Ren B., Sun S.-G., et al. Synthesis of Au@Pd core–shell nanoparticles with controllable size and their application in surface-enhanced Raman spectroscopy. Chemical Physics Letters. 2005;408:354-9.
[52] Hu J.-W., Li J.-F., Ren B., Wu D.-Y., Sun S.-G., Tian Z.-Q. Palladium-Coated Gold Nanoparticles with a Controlled Shell Thickness Used as Surface-Enhanced Raman Scattering Substrate. J Phys Chem C. 2006;111:1105-12.

[53] Tian Z.-Q., Ren B., Li J.-F., Yang Z.-L. Expanding generality of surface-enhanced Raman spectroscopy with borrowing SERS activity strategy. Chemical Communications. 2007:3514-34.
[54] Fang P.-P., Li J.-F., Yang Z.-L., Li L.-M., Ren B., Tian Z.-Q. Optimization of SERS activities of gold nanoparticles and gold-core–palladium-shell nanoparticles by controlling size and shell thickness. Journal of Raman Spectroscopy. 2008;39:1679-87.
[55] Huang C. W., Hao Y. W., Nyagilo J., Dave D. P., Xu L. F., Sun X. K. Porous hollow gold nanoparticles for cancer SERS imaging. Journal of Nano Research. 2010;10:137-48.
[56] Huang C., Hao Y. Plasmonic Properties of Polycrystalline Hollow Au Nanoparticles: A Surface Roughness Effect. Journal of Nanoscience and Nanotechnology. 2011;11:3701-5.
[57] Horinouchi S., Yamanoi Y., Yonezawa T., Mouri T., Nishihara H. Hydrogen Storage Properties of Isocyanide-Stabilized Palladium Nanoparticles. Langmuir. 2006;22:1880-4.
[58] Osawa M., Komatsu K.-i., Samjeské G., Uchida T., Ikeshoji T., Cuesta A., et al. The Role of Bridge-Bonded Adsorbed Formate in the Electrocatalytic Oxidation of Formic Acid on Platinum. Angewandte Chemie International Edition. 2011;50:1159-63.
[59] Suo Y., Hsing I. M. Synthesis of bimetallic PdAu nanoparticles for formic acid oxidation. Electrochimica Acta. 2011;56:2174-83.
[60] Zhang G., Wang Y., Wang X., Chen Y., Zhou Y., Tang Y., et al. Preparation of Pd–Au/C catalysts with different alloying degree and their electrocatalytic performance for formic acid oxidation. Applied Catalysis B: Environmental. 2011;102:614-9.
[61] Song H. M., Anjum D. H., Khashab N. M. Shape-controlled synthesis of Au@Pd core-shell nanoparticles and their corresponding electrochemical properties. RSC Advances. 2012;2:3621-4.
[62] Teng X., Wang Q., Liu P., Han W., Frenkel A. I., Wen, et al. Formation of Pd/Au Nanostructures from Pd Nanowires via Galvanic Replacement Reaction. Journal of the American Chemical Society. 2007;130:1093-101.
[63] Samjeské G., Osawa M. Current Oscillations during Formic Acid Oxidation on a Pt Electrode: Insight into the Mechanism by Time-Resolved IR Spectroscopy. Angewandte Chemie. 2005;117:5840-4.
[64] Yano H., Kataoka M., Yamashita H., Uchida H., Watanabe M. Oxygen Reduction Activity of Carbon-Supported Pt−M (M = V, Ni, Cr, Co, and Fe) Alloys Prepared by Nanocapsule Method. Langmuir. 2007;23:6438-45.
[65] Qian Y., Wen, Adcock P. A., Jiang Z., Hakim N., Saha M. S., et al. PtM/C Catalyst Prepared Using Reverse Micelle Method for Oxygen Reduction Reaction in PEM Fuel Cells. J Phys Chem C. 2008;112:1146-57.
[66] Gupta G., Slanac D. A., Kumar P., Wiggins-Camacho J. D., Wang X., Swinnea S., et al. Highly Stable and Active Pt−Cu Oxygen Reduction Electrocatalysts Based on Mesoporous Graphitic Carbon Supports. Chemistry of Materials. 2009;21:4515-26.
[67] Venkateswara Rao C., Viswanathan B. ORR Activity and Direct Ethanol Fuel Cell Performance of Carbon-Supported Pt−M (M = Fe, Co, and Cr) Alloys Prepared by Polyol Reduction Method. J Phys Chem C. 2009;113:18907-13.

[68] Rao C. S., Singh D. M., Sekhar R., Rangarajan J. Pt–Co electrocatalyst with varying atomic percentage of transition metal. International Journal of Hydrogen Energy. 2011;36:14805-14.
[69] Yoo S. J., Lee K.-S., Hwang S. J., Cho Y.-H., Kim S.-K., Yun J. W., et al. Pt3Y electrocatalyst for oxygen reduction reaction in proton exchange membrane fuel cells. International Journal of Hydrogen Energy. 2012;37:9758-65.
[70] Wang M., Zhang W., Wang J., Minett A., Lo V., Liu H., et al. Mesoporous hollow PtCu nanoparticles for electrocatalytic oxygen reduction reaction. Journal of Materials Chemistry A. 2013;1:2391-4.
[71] Weber M., Wang J. T., Wasmus S., Savinell R. Formic Acid Oxidation in a Polymer Electrolyte Fuel Cell A Real-Time Mass-Spectrometry Study. Journal of The Electrochemical Society. 1996;143:L158-L60.
[72] Marković N. M., Gasteiger H. A., Ross Jr P. N., Jiang X., Villegas I., Weaver M. J. Electro-oxidation mechanisms of methanol and formic acid on Pt-Ru alloy surfaces. Electrochimica Acta. 1995;40:91-8.
[73] Parsons R., VanderNoot T. The oxidation of small organic molecules: A survey of recent fuel cell related research. Journal of Electroanalytical Chemistry and Interfacial Electrochemistry. 1988;257:9-45.
[74] Xia X. H., Iwasita T. Influence of Underpotential Deposited Lead upon the Oxidation of HCOOH in HClO4 at Platinum Electrodes. Journal of The Electrochemical Society. 1993;140:2559-65.
[75] Baldauf M., Kolb D. Formic acid oxidation on ultrathin Pd films on Au (hkl) and Pt (hkl) electrodes. The Journal of Physical Chemistry. 1996;100:11375-81.
[76] Fang C., Chungang W., Tingting W., Zhanfang M., Zhongmin S. L-cysteine functionalized gold nanoparticles for the colorimetric detection of Hg 2+ induced by ultraviolet light. Nanotechnology. 2010;21:025501.
[77] Hu M., Chen J., Li Z.-Y., Au L., Hartland G. V., Li X., et al. Gold nanostructures: engineering their plasmonic properties for biomedical applications. Chemical Society Reviews. 2006;35:1084-94.
[78] Faraday M. The Bakerian Lecture: Experimental Relations of Gold (and Other Metals) to Light. Philosophical Transactions of the Royal Society of London. 1857;147:145-81.
[79] Turkevich J., Stevenson P. C., Hillier J. A study of the nucleation and growth processes in the synthesis of colloidal gold. Discussions of the Faraday Society. 1951;11:55-75.
[80] Brust M., Walker M., Bethell D., Schiffrin D. J., Whyman R. Synthesis of thiol-derivatised gold nanoparticles in a two-phase Liquid-Liquid system. Journal of the Chemical Society, Chemical Communications. 1994:801-2.
[81] Daniel M.-C., Astruc D. Gold Nanoparticles: Assembly, Supramolecular Chemistry, Quantum-Size-Related Properties, and Applications toward Biology, Catalysis, and Nanotechnology. Chemical Reviews. 2003;104:293-346.
[82] Grzelczak M., Perez-Juste J., Mulvaney P., Liz-Marzan L. M. Shape control in gold nanoparticle synthesis. Chemical Society Reviews. 2008;37:1783-91.
[83] Ziegler C., Eychmüller A. Seeded Growth Synthesis of Uniform Gold Nanoparticles with Diameters of 15−300 nm. J Phys Chem C. 2011:4502-6.
[84] Schwartzberg A. M., Olson T. Y., Talley C. E., Zhang J. Z. Synthesis, Characterization, and Tunable Optical Properties of Hollow Gold Nanospheres†. J Phys Chem B. 2006;110:19935-44.

[85] Huang C. BUBBLE TEMPLATE SYNTHESIS OF HOLLOW GOLD NANOPARTICLES AND THEIR APPLICATIONS AS THERANOSTIC AGENTS. Arlington, Texas: UT-Arlington; 2010.
[86] Huang C., Jiang J., Lu M., Sun L., Meletis E. I., Hao Y. Capturing electrochemically evolved nanobubbles by electroless deposition. A facile route to the synthesis of hollow nanoparticles. Nano Letters. 2009;9:4297-301.
[87] Huang C., Jiang J., Muangphat C., Sun X., Hao Y. Trapping iron oxide into hollow gold nanoparticles. Nanoscale Res Lett. 2011;6:1-5.
[88] Kim Y., Hong J. W., Lee Y. W., Kim M., Kim D., Yun W. S., et al. Synthesis of AuPt Heteronanostructures with Enhanced Electrocatalytic Activity toward Oxygen Reduction. Angewandte Chemie. 2010;122:10395-9.
[89] Li X., Liu J., He W., Huang Q., Yang H. Influence of the composition of core–shell Au–Pt nanoparticle electrocatalysts for the oxygen reduction reaction. Journal of Colloid and Interface Science. 2010;344:132-6.
[90] Du B., Zaluzhna O., Tong Y. J. Electrocatalytic properties of Au@Pt nanoparticles: effects of Pt shell packing density and Au core size. Physical Chemistry Chemical Physics. 2011;13:11568-74.
[91] Wang L., Yamauchi Y. Strategic Synthesis of Trimetallic Au@Pd@Pt Core−Shell Nanoparticles from Poly(vinylpyrrolidone)-Based Aqueous Solution toward Highly Active Electrocatalysts. Chemistry of Materials. 2011;23:2457-65.
[92] Shuangyin W., Noel K., Sanping J., Xin W. Controlled synthesis of dendritic Au@Pt core–shell nanomaterials for use as an effective fuel cell electrocatalyst. Nanotechnology. 2009;20:025605.
[93] Ataee-Esfahani H., Wang L., Nemoto Y., Yamauchi Y. Synthesis of Bimetallic Au@Pt Nanoparticles with Au Core and Nanostructured Pt Shell toward Highly Active Electrocatalysts. Chemistry of Materials. 2010;22:6310-8.
[94] Yancey D. F., Carino E. V., Crooks R. M. Electrochemical Synthesis and Electrocatalytic Properties of Au@Pt Dendrimer-Encapsulated Nanoparticles. Journal of the American Chemical Society. 2010;132:10988-9.
[95] Song H. M., Anjum D. H., Sougrat R., Hedhili M. N., Khashab N. M. Hollow Au@Pd and Au@Pt core-shell nanoparticles as electrocatalysts for ethanol oxidation reactions. Journal of Materials Chemistry. 2012;22:25003-10.
[96] Xie W., Herrmann C., Kömpe K., Haase M., Schlücker S. Synthesis of Bifunctional Au/Pt/Au Core/Shell Nanoraspberries for in Situ SERS Monitoring of Platinum-Catalyzed Reactions. Journal of the American Chemical Society. 2011;133:19302-5.
[97] Lee Y. W., Kim M., Kim Z. H., Han S. W. One-Step Synthesis of Au@Pd Core−Shell Nanooctahedron. Journal of the American Chemical Society. 2009;131:17036-7.
[98] Yang C.-W., Chanda K., Lin P.-H., Wang Y.-N., Liao C.-W., Huang M. H. Fabrication of Au–Pd Core–Shell Heterostructures with Systematic Shape Evolution Using Octahedral Nanocrystal Cores and Their Catalytic Activity. Journal of the American Chemical Society. 2011;133:19993-20000.
[99] Okamoto H., Kon W., Mukouyama Y. Five current peaks in voltammograms for oxidations of formic acid, formaldehyde, and methanol on platinum. J Phys Chem B. 2005;109:15659-66.
[100] Zhang J. PEM Fuel Cell Electrocatalysts and Catalyst Layers Fundamentals and Applications: Springer; 2008.
[101] Qiang Z., Ruirui Y., Fengxing J., Huiwen W., Chunyang Z., Ping Y., et al. Au as an efficient promoter for electrocatalytic oxidation of formic acid and carbon

monoxide: a comparison between Pt-on-Au and PtAu alloy catalysts. Gold Bulletin. 2013.
[102] Liu F., Wang C.-Y. Mixed Potential in a Direct Methanol Fuel Cell: Modeling and Experiments. Journal of The Electrochemical Society. 2007;154:B514-B22.
[103] Hsing I.-M., Wang X., Leng Y.-J. Electrochemical Impedance Studies of Methanol Electro-oxidation on Pt/C Thin Film Electrode. Journal of The Electrochemical Society. 2002;149:A615-A21.
[104] Orts J. M., Louis E., Sander L. M., Clavilier J. Numerical simulation of the voltammetric electrooxidation of CO adsorbed on Pt(111). Electrochimica Acta. 1998;44:1221-7.
[105] Mukouyama Y., Kikuchi M., Samjeske G., Osawa M., Okamoto H. Potential oscillations in galvanostatic electrooxidation of formic acid on platinum: A mathematical modeling and simulation. J Phys Chem B. 2006;110:11912-7.
[106] Wang H.-F., Liu Z.-P. Formic Acid Oxidation at Pt/H2O Interface from Periodic DFT Calculations Integrated with a Continuum Solvation Model. J Phys Chem B. 2009;113:17502-8.
[107] Gao W., Keith J. A., Anton J., Jacob T. Oxidation of formic acid on the Pt(111) surface in the gas phase. Dalton Transactions. 2010;39:8450-6.
[108] Xu J., Yuan D., Yang F., Mei D., Zhang Z., Chen Y.-X. On the mechanism of the direct pathway for formic acid oxidation at a Pt(111) electrode. Physical Chemistry Chemical Physics. 2013;15:4367-76.
[109] Lović J., Tripković A., Gojković S. L., Popović K. D., Tripković D., Olszewski P., et al. Kinetic study of formic acid oxidation on carbon-supported platinum electrocatalyst. Journal of Electroanalytical Chemistry. 2005;581:294-302.
[110] Marković N., Gasteiger H., Grgur B., Ross P. Oxygen reduction reaction on Pt (111): effects of bromide. Journal of Electroanalytical Chemistry. 1999;467:157-63.
[111] Schmidt T., Paulus U., Gasteiger H., Behm R. The oxygen reduction reaction on a Pt/carbon fuel cell catalyst in the presence of chloride anions. Journal of Electroanalytical Chemistry. 2001;508:41-7.
[112] Paulus U., Wokaun A., Scherer G., Schmidt T., Stamenkovic V., Markovic N. M., et al. Oxygen reduction on high surface area Pt-based alloy catalysts in comparison to well defined smooth bulk alloy electrodes. Electrochimica Acta. 2002;47:3787-98.
[113] Paulus U., Wokaun A., Scherer G., Schmidt T., Stamenkovic V., Radmilovic V., et al. Oxygen reduction on carbon-supported Pt-Ni and Pt-Co alloy catalysts. J Phys Chem B. 2002;106:4181-91.
[114] Yang H., Vogel W., Lamy C., Alonso-Vante N. Structure and electrocatalytic activity of carbon-supported Pt-Ni alloy nanoparticles toward the oxygen reduction reaction. J Phys Chem B. 2004;108:11024-34.
[115] Huang Q., Yang H., Tang Y., Lu T., Akins D. L. Carbon-supported Pt–Co alloy nanoparticles for oxygen reduction reaction. Electrochemistry Communications. 2006;8:1220-4.
[116] Neyerlin K., Srivastava R., Yu C., Strasser P. Electrochemical activity and stability of dealloyed Pt–Cu and Pt–Cu–Co electrocatalysts for the oxygen reduction reaction (ORR). Journal of Power Sources. 2009;186:261-7.
[117] Wang C., Daimon H., Sun S. Dumbbell-like Pt− Fe3O4 Nanoparticles and Their Enhanced Catalysis for Oxygen Reduction Reaction. Nano Letters. 2009;9:1493-6.

[118] Savadogo O., Lee K., Oishi K., Mitsushima S., Kamiya N., Ota K.-I. New palladium alloys catalyst for the oxygen reduction reaction in an acid medium. Electrochemistry Communications. 2004;6:105-9.
[119] Shao M.-H., Sasaki K., Adzic R. R. Pd-Fe nanoparticles as electrocatalysts for oxygen reduction. Journal of the American Chemical Society. 2006;128:3526-7.
[120] Chen Z., Waje M., Li W., Yan Y. Supportless Pt and PtPd Nanotubes as Electrocatalysts for Oxygen-Reduction Reactions. Angewandte Chemie International Edition. 2007;46:4060-3.
[121] Wang W., Zheng D., Du C., Zou Z., Zhang X., Xia B., et al. Carbon-supported Pd-Co bimetallic nanoparticles as electrocatalysts for the oxygen reduction reaction. Journal of Power Sources. 2007;167:243-9.
[122] Lim B., Jiang M., Camargo P. H., Cho E. C., Tao J., Lu X., et al. Pd-Pt bimetallic nanodendrites with high activity for oxygen reduction. Science. 2009;324:1302-5.
[123] Nørskov J. K., Rossmeisl J., Logadottir A., Lindqvist L., Kitchin J. R., Bligaard T., et al. Origin of the Overpotential for Oxygen Reduction at a Fuel-Cell Cathode. J Phys Chem B. 2004;108:17886-92.
[124] Zhang J. PEM Fuel Cell Electrocatalysts and Catalyst Layers Fundamentals and Applications. London: Springer; 2008.
[125] Xu C., Zhang Y., Wang L., Xu L., Bian X., Ma H., et al. Nanotubular Mesoporous PdCu Bimetallic Electrocatalysts toward Oxygen Reduction Reaction. Chemistry of Materials. 2009;21:3110-6.
[126] Zhai J., Huang M., Dong S. Electrochemical Designing of Au/Pt Core Shell Nanoparticles as Nanostructured Catalyst with Tunable Activity for Oxygen Reduction. Electroanalysis. 2007;19:506-9.
[127] Kumar S. S., Phani K. L. N. Exploration of unalloyed bimetallic Au-Pt/C nanoparticles for oxygen reduction reaction. Journal of Power Sources. 2009;187:19-24.
[128] Deng X.-C., Tian X.-D., Wen F.-P., Yi F., Cheng M.-Q., Zhong Q.-L., et al. Electrochemical Study of Au@Pt Nanoparticles for Oxygen Reduction Reaction. Chemical Journal of Chinese Universities-Chinese. 2012;33:336-40.
[129] Ye F., Liu H., Hu W., Zhong J., Chen Y., Cao H., et al. Heterogeneous Au-Pt nanostructures with enhanced catalytic activity toward oxygen reduction. Dalton Transactions. 2012;41:2898-903.
[130] Wang J. X., Markovic N. M., Adzic R. R. Kinetic Analysis of Oxygen Reduction on Pt(111) in Acid Solutions: Intrinsic Kinetic Parameters and Anion Adsorption Effects. J Phys Chem B. 2004;108:4127-33.
[131] Lu L., Sun G., Zhang H., Wang H., Xi S., Hu J., et al. Fabrication of core-shell Au-Pt nanoparticle film and its potential application as catalysis and SERS substrate. Journal of Materials Chemistry. 2004;14:1005-9.
[132] Kim N. H., Kim K. Adsorption Characteristics of Arylisocyanide on Au and Pt Electrode Surfaces: Surface-Enhanced Raman Scattering Study. J Phys Chem B. 2006;110:1837-42.
[133] Guo S., Wang L., Wang Y., Fang Y., Wang E. Bifunctional Au@Pt hybrid nanorods. Journal of Colloid and Interface Science. 2007;315:363-8.
[134] Park Y.-K., Yoo S.-H., Park S. Three-Dimensional Pt-Coated Au Nanoparticle Arrays: Applications for Electrocatalysis and Surface-Enhanced Raman Scattering. Langmuir. 2008;24:4370-5.
[135] Li J.-F., Yang Z.-L., Ren B., Liu G.-K., Fang P.-P., Jiang Y.-X., et al. Surface-Enhanced Raman Spectroscopy Using Gold-Core Platinum-Shell Nanoparticle

Film Electrodes: Toward a Versatile Vibrational Strategy for Electrochemical Interfaces†. Langmuir. 2006;22:10372-9.
[136] Zhang B., Li J.-F., Zhong Q.-L., Ren B., Tian Z.-Q., Zou S.-Z. Electrochemical and Surfaced-Enhanced Raman Spectroscopic Investigation of CO and SCN- Adsorbed on Aucore−Ptshell Nanoparticles Supported on GC Electrodes. Langmuir. 2005;21:7449-55.
[137] Heck K. N., Janesko B. G., Scuseria G. E., Halas N. J., Wong M. S. Observing Metal-Catalyzed Chemical Reactions in Situ Using Surface-Enhanced Raman Spectroscopy on Pd−Au Nanoshells. Journal of the American Chemical Society. 2008;130:16592-600.
[138] Mayrhofer K. J. J., Blizanac B. B., Arenz M., Stamenkovic V. R., Ross P. N., Markovic N. M. The Impact of Geometric and Surface Electronic Properties of Pt-Catalysts on the Particle Size Effect in Electrocatalysis. J Phys Chem B. 2005;109:14433-40.
[139] Antolini E., Salgado J. R. C., Giz M. J., Gonzalez E. R. Effects of geometric and electronic factors on ORR activity of carbon supported Pt–Co electrocatalysts in PEM fuel cells. International Journal of Hydrogen Energy. 2005;30:1213-20.
[140] Chen M., Kumar D., Yi C.-W., Goodman D. W. The Promotional Effect of Gold in Catalysis by Palladium-Gold. Science. 2005;310:291-3.
[141] Zhang J., Vukmirovic M. B., Xu Y., Mavrikakis M., Adzic R. R. Controlling the Catalytic Activity of Platinum-Monolayer Electrocatalysts for Oxygen Reduction with Different Substrates. Angewandte Chemie. 2005;117:2170-3.
[142] Zhou W., Lee J. Y. Particle Size Effects in Pd-Catalyzed Electrooxidation of Formic Acid. J Phys Chem C. 2008;112:3789-93.
[143] Kitchin J. R., Norskov J. K., Barteau M. A., Chen J. G. Modification of the surface electronic and chemical properties of Pt(111) by subsurface 3d transition metals. The Journal of Chemical Physics. 2004;120:10240-6.
[144] Huang C., Li Y.-J., Muangphat C., Hao Y. Electroless deposition of Au around electrochemically evolved hydrogen bubbles. Electrochimica Acta. 2011;56:8319-24.
[145] Brenner A., Riddell G. E. Nickel plating on steel by chemical reduction. Proc Am Electroplaters Soc. 1946;33:23-9.
[146] Bindra P., Arbach G., Stimming U. On the mechanism of laser enhanced plating of copper. Journal of The Electrochemical Society. 1987;134:2893-900.
[147] Wagner C., Traud W. “On the Interpretation of Corrosion Processes through the Superposition of Electrochemical Partial Processes and on the Potential of Mixed Electrodes,” with a Perspective by F. Mansfeld. Corrosion. 2006;62:843-55.
[148] Donahue F. M., Wong K., Bhalla R. Kinetics of Electroless Copper Plating IV. Empirical Rate Law for Baths. Journal of The Electrochemical Society. 1980;127:2340-2.
[149] Bertolini J. C., Delichere P., Khanra B. C., Massardier J., Noupa C., Tardy B. Electronic properties of supported Pd aggregates in relation with their reactivity for 1,3-butadiene hydrogenation. Catal Lett. 1990;6:215-23.
[150] Patel S., Jiang J., Liu F. Facile synthesis and characterization of highly dispersed platinum nanoparticles for fuel cells. International Journal of Hydrogen Energy. 2011;36:11108-15.
[151] Tedsree K., Chan C. W. A., Jones S., Cuan Q., Li W.-K., Gong X.-Q., et al. 13C NMR Guides Rational Design of Nanocatalysts via Chemisorption Evaluation in Liquid Phase. Science. 2011;332:224-8.

[152] Mohl M., Dobo D., Kukovecz A., Konya Z., Kordas K., Wei J., et al. Formation of CuPd and CuPt Bimetallic Nanotubes by Galvanic Replacement Reaction. J Phys Chem C. 2011;115:9403-9.
[153] Fouda-Onana F., Savadogo O. Study of O2 and OH adsorption energies on Pd–Cu alloys surface with a quantum chemistry approach. Electrochimica Acta. 2009;54:1769-76.
[154] Treimer S., Tang A., Johnson D. C. A Consideration of the Application of Koutecký-Levich Plots in the Diagnoses of Charge-Transfer Mechanisms at Rotated Disk Electrodes. Electroanalysis. 2002;14:165-71.
[155] Levich V. G. Physicochemical Hydrodynamics. 2nd ed. N.J.: Prentice-Hall Englewood Cliffs; 1962.
[156] A. J. Bard L. R. F. Electrochemical Method. 1st ed. New York: Wiley; 1980.
[157] Shim J. H., Kim J., Lee C., Lee Y. Porous Pd Layer-Coated Au Nanoparticles Supported on Carbon: Synthesis and Electrocatalytic Activity for Oxygen Reduction in Acid Media. Chemistry of Materials. 2011;23:4694-700.
[158] Wang X., Hu J.-M., Hsing I. M. Electrochemical investigation of formic acid electro-oxidation and its crossover through a Nafion® membrane. Journal of Electroanalytical Chemistry. 2004;562:73-80.
[159] Chen H., Wei G., Ispas A., Hickey S. G., Eychmüller A. Synthesis of Palladium Nanoparticles and Their Applications for Surface-Enhanced Raman Scattering and Electrocatalysis. J Phys Chem C. 2010;114:21976-81.
[160] Feng Y.-Y., Liu Z.-H., Xu Y., Wang P., Wang W.-H., Kong D.-S. Highly active PdAu alloy catalysts for ethanol electro-oxidation. Journal of Power Sources. 2013;232:99-105.
[161] Liu Z., Yang Z.-L., Cui L., Ren B., Tian Z.-Q. Electrochemically Roughened Palladium Electrodes for Surface-Enhanced Raman Spectroscopy: Methodology, Mechanism, and Application. J Phys Chem B. 2007;111:1770-5.
[162] Unterhalt H., Galletto P., Morkel M., Rupprechter G., Freund H. J. Sum Frequency Generation Study of CO Adsorption on Palladium Model Catalysts. physica status solidi (a). 2001;188:1495-503.
[163] Fleischmann M., Graves P. R., Robinson J. The raman spectroscopy of the ferricyanide/ferrocyanide system at gold, β-palladium hydride and platinum electrodes. Journal of Electroanalytical Chemistry and Interfacial Electrochemistry. 1985;182:87-98.
[164] Gao Y.-Y., Tan C.-H., Ye-Ping L. I., Guo J., Zhang S.-Y. Formic acid–Formate blended solution: A new fuel system with high oxidation activity. International Journal of Hydrogen Energy. 2012;37:3433-7.
[165] Sun S. G., Clavilier J., Bewick A. The mechanism of electrocatalytic oxidation of formic acid on Pt (100) and Pt (111) in sulphuric acid solution: an emirs study. Journal of Electroanalytical Chemistry and Interfacial Electrochemistry. 1988;240:147-59.
[166] Tao C., Xu L., Guan J. Well-dispersed mesoporous Ta2O5 submicrospheres: Enhanced photocatalytic activity by tuning heating rate at calcination. Chemical Engineering Journal. 2013;229:371-7.
[167] Chen Y. X., Heinen M., Jusys Z., Behm R. J. Kinetics and Mechanism of the Electrooxidation of Formic Acid—Spectroelectrochemical Studies in a Flow Cell. Angew Chem Int Ed. 2006;45:981-5.
[168] Liu Y., Wang L., Wang G., Deng C., Wu B., Gao Y. High Active Carbon Supported PdAu Catalyst for Formic Acid Electrooxidation and Study of the Kinetics. J Phys Chem C. 2010;114:21417-22.

[169] Chen Y. X., Heinen M., Jusys Z., Behm R. J. Bridge-Bonded Formate: Active Intermediate or Spectator Species in Formic Acid Oxidation on a Pt Film Electrode?†. Langmuir. 2006;22:10399-408.

Biographical Information

Chiajen Hsu was born in Kaohsiung City, Taiwan. He received his bachelor degree in materials science and engineering (MSE) from National Cheng Kung University in 2004, and master degree from National Chung Hsing University in 2006. After that, he took military service for 15 months. In 2013, he received his Ph.D. degree in Materials Science and Engineering from the University of Texas at Arlington under the mentorship of Dr. Fuqiang Liu. During his Ph. D education, he served as a volunteer for the MSE summer camp and joined several oral presentation competitions hosted by ASM and TSM. Several awards and fellowships he earned such as:

(1) 2012 North Texas Symposium on Materials Science and Engineering- First Place Oral Presentation, March 28 2012

(2) 2013 Academic Excellence Award of College of Engineering- UT-Arlington, April 17 2013

(3) 2013 Office of Graduate Studies Dissertation Fellowship Summer 2013 Term

His research area focused on the fabrication, electrochemical characterization, and simulation for Pt and Pd based catalysts. He has successfully fabricated unique Au/Pd and Au/PtCu core-shell nanoparticles which applied in the direct formic acid fuel cells with the collaboration with Dr. Yaowu Hao's biomaterial lab in UTA. The results were already presented in 2012 ECS meeting (Seattle, USA) and published in the following journals:

(1) **Hsu, C.**, Huang C., Y. Hao, and F. Liu "Au/Pd core–shell nanoparticles for enhanced electrocatalytic activity and durability." Electrochemistry Communications (2012) 23(0): 133-136 [DOI: http://dx.doi.org/10.1016/j.elecom.2012.07.027]

(2) **Chiajen Hsu**, Chienwen Huang, Yaowu Hao and Fuqiang Liu "Synthesis of highly active and stable Au–PtCu core–shell nanoparticles for oxygen reduction reaction." Phys. Chem. Chem. Phys., 2012, 14, 14696-14701 [DOI: 10.1039/C2CP42716H]

(3) **Chiajen Hsu**, Chienwen Huang, Yaowu Hao and Fuqiang Liu "Au/Pd core-shell nanoparticles with varied hollow Au cores for enhanced formic acid oxidation." Nanoscale Research Letters 2013, 8:113 [DOI: 10.1186/1556-276X-8-113]

(4) **Chiajen Hsu**, Chienwen Huang, Yaowu Hao and Fuqiang Liu “Impact of Surface Roughness of Au Core in Au/Pd Core-Shell Nanoparticles toward Formic Acid Oxidation - Experiment and Simulation.” Journal of Power Sources 2013, [DOI: 10.1016/j.jpowsour.2013.05.185]

(5) **Chiajen Hsu**, Chienwen Huang, Yaowu Hao and Fuqiang Liu “Electro-oxidation of formate-based solutions on Au/Pd core-shell nanoparticles - Experiment and simulation” International Journal of Hydrogen Energy, [DOI: 10.1016/j.ijhydene.2013.09.019]

In addition, he also synthesized several nanostructures such as, flower-shape rutile phase Au-TiO_2 photocatalysts, and anatase phase TiO_2 nanobelts. As an engineer, he received well-training on analysis of the resulting nanostructures via different characteristic techniques such as high-resolution transmission electron microscopy (TEM), scanning electron microscopy (SEM), X-ray diffraction (XRD), energy dispersive spectrometer (EDS), Raman spectroscopy and X-ray photoelectron spectroscopy (XPS), UV-vis spectroscopy, electrochemical characterization, and computational simulation (Fluent and FDTD).